VRIJE UNIVERSITEIT

XUV Frequency Comb Metrology and the Ground State of Helium

ACADEMISCH PROEFSCHRIFT

ter verkrijging van de graad Doctor aan
de Vrije Universiteit Amsterdam,
op gezag van de rector magnificus
prof.dr. L.M. Bouter,
in het openbaar te verdedigen
ten overstaan van de promotiecommissie
van de faculteit der Exacte Wetenschappen
op donderdag 1 december 2011 om 9.45 uur
in de aula van de universiteit,
De Boelelaan 1105

door

Dominik Zbigniew Kanduła
geboren te Kościerzyna, Polen

promotoren:	prof.dr. W.M.G. Ubachs
	prof.dr. K.S.E. Eikema

Cover design: Charaf Cherkouk

The work described was performed as part of a research program of the Netherlands Organization for Scientific Research (NWO) and was carried out at LaserLaB Amsterdam, Vrije Universiteit (De Boelelaan 1083, 1081 HV Amsterdam, The Netherlands). It was supported by the Marie Curie Actions Early Stage Training programme: Advanced Training in Laser Sciences (ATLAS), while investment support was provided by the Foundation for Fundamental Research on Matter (FOM).

Contents **v**

1 Introduction **1**
1.1 Precision tests and laser spectroscopy 1
1.2 Generation and application of extreme ultraviolet frequency combs 2
1.3 Quantum-electro dynamics and the ground-state of helium 4
1.4 Motivation and outline of this thesis 12

2 Theoretical background **15**
2.1 Electromagnetic waves and wave packets 15
2.2 Frequency-comb lasers 27
2.3 Spectroscopy with frequency combs 30
2.4 An analysis of the interaction of a two-level system with a phase-locked pulse-pair 34
2.5 Theory of non-collinear optical parametric amplification . 40
2.6 High harmonic generation 44

3 Experimental realization of a frequency comb in the XUV **55**
3.1 The frequency comb laser 55
3.2 Non-collinear optical double pulse parametric amplification 59
3.3 Phase measurement setup 63
3.4 Harmonic Generation and Excitation Setup 66

4 Phase stability of optical parametric amplification **71**
4.1 Setup 73
4.2 Results and diuscussion 74
4.3 Conclusions 77

5 Phase stability of a double-pulse OPA **79**
5.1 Amplification of pulse pairs 81
5.2 Measurements of the amplifier phase shift 84
5.3 Conclusions 94

6 XUV frequency comb metrology on the ground state of helium **95**
6.1 Overview and principle of XUV comb generation and excitation 99
6.2 Experimental setup 103
6.3 Frequency metrology on $1s^2 - 1s4p$ and $1s^2 - 1s5p$ transitions in helium 110
6.4 Discussion 112
6.5 Conclusions and outlook 131

7 Outlook **135**
7.1 Two-photon excitation of the $1s^2\ {}^1\mathrm{S}_0 - 1s2s\ {}^1\mathrm{S}_0$ transition in helium 135
7.2 Programmable pulse delay for Fourier-transform spectroscopy of moderately complicated spectra 137

Bibliography **141**

List of Publications **157**

Summary **159**

Samenvatting **163**

Acknowledgements **167**

Chapter 1

Introduction

This thesis reports on the development and application of a new spectroscopic tool: the extreme ultra violet frequency comb (XFC). The XFC is based on noncollinear optical parametric chirped pulse amplification (NOPCPA) of a pulse pair from a near-infrared (near-IR) frequency comb laser to the mJ-level, and subsequent generation of high order harmonics with this pulse pair. The frequency comb, created by the high-order harmonics of the near-IR pulses is employed to measure the ground-state energy of helium precisely enough to challenge the current theoretical calculations. The motivation for these experiments is given in this first introductory chapter.

1.1 Precision tests and laser spectroscopy

Precision measurements have turned out to be crucial for our understanding of the laws of physics. For instance, the discovery of the Lamb-shift in the hydrogen atom by Lamb and Retherford [1], resulted in the formulation of the theory of quantum electro dynamics (QED) [2, 3, 4], which explained the influence of vacuum fluctuations on atomic level structure as well as on single particles (e.g. the electron anomalous magnetic moment). While implicating surprising underlying phenomena like spontaneous apperance and anihilation of elementary particles (see Fig. 1.1(b)), this theory has become one of the best tested theories to date. It is nowadays an important part of the interpretation of spectroscopic experiments to derive values of the physical constants of nature [5]. In recent years, experimenters began to investigate the possibility of *changes* of fundamental constants, by e.g. obtaining spectroscopic data with a precision that could be sufficient to observe the fractional changes of the fine structure constant α in the order of 10^{-15} on the timescale of several years [6].

The advance in spectroscopic techniques and instruments allowed to perform high precision experiments not only at microwave frequencies, such as in the experiment of Lamb and Retherford, but extended the spectrum to optical frequencies, which are of the order of several hundred THz. Before the year 2000, elaborate chains of frequency multipliers ("frequency chains") were used to bridge the gap between the microwave frequencies (at which the most precise atomic clocks operated at that time) and the visible spectral region [7, 8]. The frequency comb laser (FCL) principle that was developed around the year 2000 [9, 10] brought about a revolution in the field of high precision spectroscopy, providing the possibility to relate frequencies of visible light directly to a radio frequency, which can be accurately measured by electronic means. The large frequency-chains that were usually employed spanned over a few laboratories and needed to be operated several scientists. These could now be replaced by a FCL of 1 m^2 size, connected to a radio-frequency standard, and operated by a single person. Nowadays even small laboratories can reach accuracies of the order of 10^{-12} and better with this technology. Furthermore, the FCL is paving the way towards new atomic clocks operating on optical transitions. The best of these potential clocks is based on a single aluminum ion, and an accuracy on the order of 10^{-17} [11] has been demonstrated with it.

1.2 Generation and application of extreme ultraviolet frequency combs

The motivation that led to the development of the FCL in the IR and the visible spectral region, was twofold. On the one hand the desire to increase the accuracy of available frequency standards naturally demands higher frequencies for the oscillator and the "readout" on which the clockwork is based. On the other hand, for spectroscopy there was the desire to measure optical and higher frequencies more accurately, which required a source of those frequencies that could be directly related to the Cs-frequency standard. The development of novel more accurate frequency sources was pursued by John L. Hall and coworkers at NIST. Therefore, they initially developed and employed the FCL to extend atomic clocks to optical frequency standards, e.g. an iodine-stabilized

HeNe laser operating at 633 nm [12]. The group of Theodor W. Hänsch in the MPQ Garching developed the FCL to increase the accuracy of the spectroscopic experiments mainly on atomic hydrogen, carried out in this institute. Quite a few other groups have participated in the development of FCL's (such as the PTB in Germany [13, 14]) which has led to a myriad of applications ranging from atomic clocks (such as [11]) to attosecond science (see [15]).

The successful development of the FCL in the near-IR has motivated the development of FCLs that operate beyond the optical spectral region. The lack of lasing material at these wavelengths demands methods which differ from the state-of-the-art FCLs, which are based on pulsed lasers with fixed repetition rate and stabilized carrier-envelope phase (CEP) shift between consecutive pulses. While a frequency comb in the ultraviolet (UV) can easily be produced by frequency upconversion of the entire pulse train from a FCL in a nonlinear crystal, further upconversion is limited due to the lack of suitable nonlinear media and the limited pulse energies produced by most frequency comb laser oscillators.

In order to generate frequency combs beyond the UV spectral region two methods have been successfully employed. One method, pursued e.g. at the MPQ Garching and at JILA in Boulder, Colorado, is based on enhancement of the pulses from a FCL in an external cavity combined with generation of high-order harmonics of the enhanced light field within this cavity [16, 17]. The generated harmonic pulses inherit the frequency comb structure of the fundamental FCL, thus transporting it to higher frequencies. This method was fairly successful in the wavelength range down to 150 nm [18]; however, the spectral power and experimental conditions have not been sufficiently optimized yet to perform a spectroscopic experiment.

A second approach towards XUV-frequency comb generation is described in this thesis. It is based on the amplification of coherent pulse pairs to energy levels which are sufficient to generate high-order harmonics. The spectrum of such pulse pairs resembles a cosine-modulated continuum with maxima sitting at exactly the same positions as the comb-teeth of an infinite pulse train with the same CEP-shift and repetition time between consecutive pulses as the aforementioned amplified pulse pair. The structure of the spectrum generated by this method can differ from the spectrum of the original pulse pairs due to possible

phase-shifts occuring in the amplification and harmonic upconversion processes. Because of that, a careful calibration of the upconverted frequency comb is required. The pulse energy achievable from amplification is considerably higher than in the enhancement cavities, and therefore a higher spectral yield per pulse in the XUV can be achieved. As a result several successful spectroscopic experiments have been performed with such a source [19, 20, 21].

The experiments reported in this thesis apply this amplification approach to measure the ground state ionization energy of the helium atom with an unprecedented accuracy, so that it can be compared to the theoretical value. To achieve this, the transition frequency from the ground-state to the nP-levels ($n \in \{4, 5\}$) is measured with a frequency comb at ≈ 51 nm. The current theory of the energy structure of helium is briefly introduced in the following section.

1.3 Quantum-electro dynamics and the ground-state of helium

The high precision of the helium ground-state energy obtained in this thesis allows for a comparison with the value predicted by the quantum theory. Because helium is a three-body system, which can not be solved analytically, approximations are necessary. To cope with that, as early as 1929 Hylleraas [22] expanded the wave function in a basis set based on spherical harmonic functions on which he employed variational analysis. Present calculations still use variational methods, but at a much more sophisticated level. In order to reach a high precision, the Hamiltonian is expanded in powers of the nuclear charge Z and of the fine structure constant α. The calculation is difficult and requires the solution of many thousands of integrals. One issue is that the expansion diverges for higher orders in α, but the divergences can be canceled using the explicit form of the non-relativistic solution [23]. A good introduction to the theory can be found in the extensive survey written in 1999 by Drake [24], covering both the status of the atomic-helium theory and experiments at that time. A more elaborate treatment of the theoretical approaches can be found in [25] and [26]. A summary that incorporates progress in calculations made since then is given in this section.

The energy-structure of helium is calculated with the Schrödinger-equation $H\Psi = E\Psi$. The Hamiltonian can be written as a sum of a non-relativistic Schrödinger term H_0, a relativistic term H_{rel} and the quantum-electro-dynamics (QED) contribution H_{QED}:

$$H = H_0 + H_{rel} + H_{QED}. \tag{1.1}$$

The expectation values of the energy can be written for this Hamiltonian accordingly as:

$$E = E_0 + E_{rel} + E_{QED}. \tag{1.2}$$

Non-relativistic Terms

The Schrödinger part of the Hamiltonian takes into account non-relativistic electromagnetic interactions between the two electrons positioned at $\mathbf{r}_1$ and $\mathbf{r}_2$ with respect to the nucleus. Using the atomic units introduced by Hartree 1928, it can be written in the following form:

$$H_0 = \sum_{i=1,2} \Big(-\frac{1}{2}\nabla_i^2 - \frac{Z}{r_i} \Big) + \frac{1}{r_{12}}, \tag{1.3}$$

with $r_{12} = |\mathbf{r}_1 - \mathbf{r}_2|$. The sum in the first part of this operator describes the Coulomb- and the kinetic energies of the two electrons. The Coulomb repulsion between the electrons is taken into account in the last term of the equation. The corresponding Schrödinger equation is solved with variational calculations, using a 'doubled' set of Hylleraas' basis functions [24]:

$$\Phi_{ijk} = a_A \phi_{ijk}(\alpha_A, \beta_A) + a_B \phi_{ijk}(\alpha_B, \beta_B), \tag{1.4}$$

with:

$$\phi_{ijk}(\alpha, \beta) = r_1^i r_2^j r_{12}^k e^{-\alpha r_1 - \beta r_2} \mathcal{Y}^M_{l_1, l_2, L}(\mathbf{r}_1, \mathbf{r}_2) \pm \text{exchange term}, \tag{1.5}$$

where $\mathcal{Y}^M_{l_1,l_2,L}(\mathbf{r}_1,\mathbf{r}_2)$ is a vector-coupled product of spherical harmonics. The factors α and β can be adjusted separately to optimize the energy. The two pairs of these coefficients $(\alpha_A,\beta_A),(\alpha_B,\beta_B)$ are the same for all the basis set members. With this basis the wave function can be expanded as:

$$\Psi(\mathbf{r}_1,\mathbf{r}_2) = \sum_{i,j,k}^{i+j+k\leqslant\Omega} a_{ijk}\Phi_{ijk}. \tag{1.6}$$

The energy eigenvalues are found by studying the convergence as Ω is increased. The amount of permutations of (i,j,k) grows rapidly with increasing Ω and actual calculations carefully reduce the basis-set size. However, an elaborate treatment is beyond the scope of this thesis and the interested reader will find it in [26] and [25]. It should not be left unmentioned that the precision of present calculations surpassed a fractional accuracy of 10^{-20}, which is (as we will see later) far beyond the precision of relativistic and QED contributions.

For the non-relativistic Hamiltonian (1.1) an infinite mass of the nucleus is assumed. This is corrected by rescaling the value of Rydberg used in the atomic units by a factor μ/M, where $\mu = mM/(m+M)$ is the reduced mass, m the electron mass and M the mass of the nucleus (α-particle). The transformation of the coordinate system to the centre of mass is taken into account with a mass polarization term. The recoil correction calculated with the latter appears in the Hamiltonian as :

$$-\frac{\mu}{M}\nabla_1\nabla_2. \tag{1.7}$$

Because the electron-nucleus mass ratio in helium m^2/M^2 is of the order of 10^{-8} one could expect small contributions from the second order recoil correction. Both orders can be treated as perturbations [27]. A different approach is to perform an expansion in powers of m/M instead of μ/M to facilitate a nicer notation of relativistic corrections, which are more naturally expanded in powers of m/M [28].

Relativistic Corrections

The relativistic corrections, which result from the relative velocities of the particles, are calculated from $\langle\Psi_J|H_{rel}|\Psi_J\rangle$, where Ψ_J is the previ-

ously obtained non-relativistic wave function for the angular momentum $\mathbf{J} = \mathbf{L}+\mathbf{S}$, which is a combination of the total orbital angular momentum $\mathbf{L}$ and total spin $\mathbf{S}$ of the electrons. The Hamiltonian is derived from the *Breit equation* [29], which itself is based on the *Dirac equation* for two spin-1/2 particles in an electromagnetic field. It can be formulated using six operators as [30]:

$$H_{rel} = \alpha^2 \left(\frac{\mu}{m}\right)^3 \Big[B_1 + B_2 + B_4 + B_{SO} + B_{SOO} + B_{SS}\Big], \quad (1.8)$$

with:

$$\begin{aligned}
B_1 &= \frac{\mu}{8m}(p_1^4 + p_2^2) \quad (1.9)\\
B_2 &= -\frac{1}{2}\left(\frac{1}{r_{12}}(\mathbf{p}_1 \cdot \mathbf{p}_1 + \frac{1}{r_{12}^3}\mathbf{r}_{12} \cdot (\mathbf{r}_{12} \cdot \mathbf{p}_1)\mathbf{p}_2\right)\\
B_4 &= \pi\left(\frac{Z}{2}\delta(\mathbf{r}_1) + \frac{Z}{2}\delta(\mathbf{r}_2) - \delta(\mathbf{r}_1)\right)\\
B_{SO} &= \frac{Z}{4}\left[\frac{1}{r_1^3}(\mathbf{r}_1 \times \mathbf{p}_1) \cdot \boldsymbol{\sigma}_1 + \frac{1}{r_2^3}(\mathbf{r}_2 \times \mathbf{p}_2) \cdot \boldsymbol{\sigma}_2\right]\\
B_{SOO} &= \frac{1}{4}\left[\frac{1}{r_{12}^3}\mathbf{r}_{12} \times \mathbf{p}_2 \cdot (2\boldsymbol{\sigma}_1 + \boldsymbol{\sigma}_2) - \frac{1}{r_{12}^3}\mathbf{r}_{12} \times \mathbf{p}_1 \cdot (2\boldsymbol{\sigma}_2 + \boldsymbol{\sigma}_1)\right]\\
B_{SS} &= \frac{1}{4}\left[-\frac{8}{3}\pi\delta(\mathbf{r}_{12}) + \frac{1}{r_{12}^3}\boldsymbol{\sigma}_1 \cdot \boldsymbol{\sigma}_2 - \frac{3}{r_{12}^3}(\boldsymbol{\sigma}_1 \cdot \mathbf{r}_{12})(\boldsymbol{\sigma}_1 \cdot \mathbf{r}_{12})\right].
\end{aligned}$$

Here $\mathbf{p}_1$ and $\mathbf{p}_2$ are the two momentum operators for electron 1 and 2. The first three terms describe the spin-unrelated effects: B_1 the relativistic mass increase, B_2 the retardation of the electromagnetic fields produced by the moving particles. B_4 is a term that originates from the Dirac equation, providing additional corrections to the fields of the interacting particles. The terms B_{SO}, B_{SOO} and B_{SS} describe the spin-orbit, the spin-other-orbit, and the spin-spin interaction.

The non-relativistic and α^2-contributions to the binding energies of some lower energy eigenstates of helium (apart from the QED contributions, which is discussed in the next section) are summarized in table 1.1. All the contributions can be calculated with high precision. A residual

Term	$1\ ^1S_0$	$2\ ^3S_1$	$2\ ^1P_1$
E_0	-5945405676	-1152795881.8	-814736669.9
$\Delta E_0(\mu/M)$	143446	6711.2	41522.2
$\Delta E_0(\mu^2/M^2)$	-58	-7.1	-20.8
E_{rel}	16902	-57621.4	-14022.1
$\Delta E_{rel}(\mu/M)_{ms}$	-155	-5.6	4.2
$\Delta E_{rel}(\mu/M)_{mp}$	53	2.0	8.4
E_{QED}	41284(36)	4058.8(2.5)	-1255.1(1.0)
Total [30]	-5945204175(36)	-1152842741.3(2.5)	-814709147.4(1.0)
Total [31, 32]	-5945204174(36)	-1152842741.6(1.0)	-814709145.99(16)

Table 1.1: Contributions to the binding energies for some lower lying states in helium. All energies, expressed in MHz are taken from [30]. E_0 is the non-relativistic binding energy rescaled taking the reduced mass of helium into account, while the corrections ΔE_0 are representing the first and second order mass polarization. E_{rel} gives the relativistic correction based on Eq. 1.8. The ΔE_{rel} terms arise from mass scaling (ms) and mass polarization (mp). The composition of the higher-order contribution E_{QED} can be found in Table 1.2

contribution from higher orders in Z and α forms an object of research at the frontier of QED-theory.

QED Contributions

The dawn of quantum electrodynamics goes back to Paul A.M. Dirac, who wrote an article about radiation-matter interaction in 1927 [33]. Dirac described the electromagnetic field as an ensemble of harmonic oscillators on which he applied the concept of creation and annihilation operators. His formalism was developed further in the following years culminating in an elegant formulation of quantum electrodynamics by Enrico Fermi 1932 in [34]. This theory seemed to be capable of computing virtually any physical process, that involves interaction between light and charged particles. However, further studies in the 1930s revealed that these QED calculations were only reliable at first-order perturbation theory. At higher orders infinities emerged, which made these calculations physically meaningless.

Modern quantum electrodynamics began with the discovery of the Lamb-shift in hydrogen in 1947 [35]. The measured difference in the binding energy of the $2\ ^2S_{1/2}$ and $2\ ^2P_{1/2}$ states of hydrogen could not be

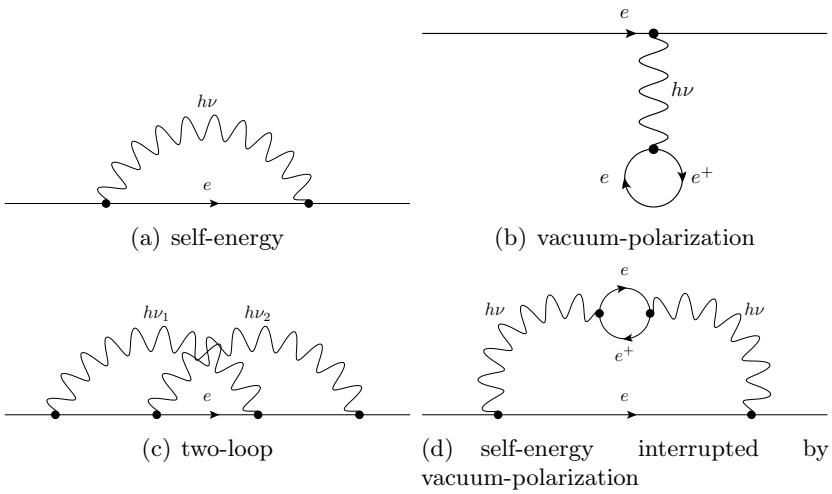

(a) self-energy (b) vacuum-polarization

(c) two-loop (d) self-energy interrupted by vacuum-polarization

Figure 1.1: Some of the lowest order QED effects displayed as Feynman diagrams. The straight lines are electrons, the wavy lines are photons, the circles represent creation and annihilation of electron-positron pairs, while the black dots are vortices.

explained by the quantum mechanical calculations at that time. However, Hans Bethe developed the method of *renormalization*, which allowed to remove the infinities that occurred in QED calculations, and was able to calculate the observed splitting in excellent agreement with experimental data [36]. On the basis of Bethes approach QED was developed further, and eventually a covariant formulation emerged that was finite at any order of the perturbation theory [2, 3, 4]. Shin'ichirō Tomonaga, Julian Seymour Schwinger and Richard Phillips Feynman were awarded with the Nobel prize in 1965 for their contributions to this field. The calculation of the QED contribution involves an expansion of the Hamiltonian in powers of Z and α and computation of the corrections to the energy eigenvalues, resulting from this expansion.

Traditionally the hydrogen atom has been, and still is a test ground for the quality of QED calculations. Experiments have reached a precision of the order of 10^{-14} [6] and new experiments are in progress to reach 10^{-15}.

The uncertainty in the calculated energy structure is dominated by the uncertainties in the Rydberg constant (fractional uncertainty at 6.6×10^{-12}) and in the size of the proton. Because of this, the high-

precision spectroscopy experiments in hydrogen are used nowadays to infer these values from the measured energy structure [5]. As Drake points out, the leading QED shift is proportional to $\alpha^3 Z_{sc}^4$ [30], where Z_{sc} is the screened nuclear charge. This makes heavy hydrogen-like ions desirable candidates for spectroscopic tests of the quality of QED calculations. An interesting example of a heavy hydrogen-like ion, where the Lamb-shift was measured is uranium U^{91+} [37]. The experiment shows good agreement between the experimentally determined Lamb-shift (460.2±4.6 eV) and the calculated value (464.26 ± 0.5 eV). However, the difficulty in generation and calibration of the necessary short wavelength hampers precision experiments on such highly charged species. The experiment presented in this thesis can be viewed as paving the route towards high precision experiments with high photonic energies for further test of the QED theory. An interesting target that could be investigated with the developed XUV-frequency comb is the helium ion He^+. The Lamb-shift is bigger in He^+ than in neutral helium due to the unshielded nuclear charge. At the same time the photon energy required for the two-photon transition between two S-states is comparable to that used in the experiment presented in this thesis.

QED corrections are the largest source of the uncertainty in the binding energies of helium. With the recent contribution from Pachucki [31, 32] the expansion is now complete up to the order of α^6. The contributions can be expressed, in the simplest form, as a sum of two parts; the first, $\Delta E_{L,1}$ corresponds to the hydrogenic Lamb shift and refers to the electron-nucleus interaction. The second part, $\Delta E_{L,2}$, describes the interaction between the two electrons. For completeness, terms correcting the infinite mass approximation (ΔE_M) and relativistic effects (ΔE_D) must be included. The physical meaning of these higher order terms in the expansion can be comprehensively expressed with *Feynman-diagrams*, where *virtual particles** play a crucial role in the determination of the resulting energy shifts. The most prominent QED effects are *self-energy* and *vacuum-polarization*. Fig. 1.1 illustrates them with Feynman-diagrams.

*Virtual particles are entities, which exist for a limited amount of time in accordance to Heisenberg's uncertainty principle. They are allowed to have finite mass and energy due to their finite lifetime. The uncertainty principle dictates that the lifetime of virtual particles is inversely proportional to their energy-(mass-)content.

Term	$1\ ^1S_0$	$2\ ^3S_1$	$2\ ^1P_1$
$\Delta E_{L,1}(\alpha^5 Z)$	440708.4	4035.8	102.1
$\Delta E_{L,2}(\alpha^5)$	-4208.2	-36.9	-62.8
ΔE_M	-4.7	-0.3	-0.0
$\Delta E_{L,1}(\alpha^6 Z^2)$	771.1	67.6	1.7
$\Delta E_{L,1}(\alpha^6 Z)$	6.9	0.6	0.0
$\Delta E_{L,2}(\alpha^6)$	30.7	0.0	0.2
ΔE_D	52.6	-1.8	2.2
$\Delta E(2\ ^3P_1 - {}^1P_1$ mixing)	–	–	4.8
$\Delta E_{L,1}(\alpha^7 Z^3 \ln^2(Z\alpha)^{-2})$	-83.6	-7.3	-0.2
$\Delta E_{L,1}(\alpha^7 Z^3 \ln(Z\alpha)^{-2})$	52.3	6.0	0.2
$\Delta E_{L,1}(\alpha^7 Z^3)$	-37.4	-3.3	-0.1
$\Delta E_{L,1}(\alpha^7 Z^2)$	-3.9	-0.3	-0.0
$\Delta E_{L,1}(\alpha^7)$ total	-72(36)	-5.0(2.5)	-0.1(1.0)
Total	41284(36)	4058.8(2.5)	-1255.1(1.0)

Table 1.2: QED-Contributions to the binding energies of several lower lying states in helium [30]. All energies are expressed in MHz. The errors reflect the estimated size of the terms that were not calculated so far.

Self-energy (Fig 1.1(a)) describes emission and re-absorption of virtual photons by the electrons and leads to the biggest of the QED corrections in atoms. The momentum exchange with the photons takes place at a much shorter time scale than an orbital period of the electron, resulting in a jittery movement of the electrons. Due to this jitter, the charge of the particles loses its point-like nature and occupies a finite volume. This becomes important, as soon as the electron comes in the vicinity of another particle within the effective charge radius. The resulting deviation from the $1/r$-law in the Coulomb interaction reduces the binding energy of the electron to the nucleus but also reduces the repulsion between the two electrons in helium. The size of this effect depends on the amplitude of the electronic wave function, that overlaps with the nucleus. For that reason it is strongest for the ground state and diminishes rapidly for states of higher principal quantum number n and even more rapidly for states of high angular momentum quantum number ℓ. The inter-electronic contribution reduces the repulsion between the electrons, and because of that the spatial extension of their wave functions, leading to a slight increase of their binding energies.

Vacuum polarization(Fig 1.1(b) is the second biggest QED-effect, which refers to the creation and annihilation of electron-positron pairs. The created positronium exists long enough to align in the field of the nucleus and thus slightly screen the nuclear charge seen by the electrons.

There is an infinite number of Feynman-diagrams, which can be drawn depicting the interactions involved for an electron. An example of a *two-loop self-energy* process [38], which is an interaction of the electron with two virtual photons is given in Fig. 1.1(c). Figure 1.1(d) shows a higher-order process where a virtual photon interacts with a virtual electron-positron pair before being reabsorbed. Since each loop can thus be branched in a step-wise fashion into growing numbers og higher-order loops this results in an infinite amount of possible processes.

In practice it is a complicated task to calculate relativistic- and QED-effects in helium precisely. Generally, calculating QED-contributions is approached with an expansion in powers of α and Z. Again, deeper reviews of the present status of the calculations can be found in [30] and in [28], and in references therein. These two papers reflect two slightly different approaches, where the expansion is done in terms of the reduced mass and in terms of the rest masses respectively. Table 1.2 summarizes the results of calculations by Drake. Pachucki summarizes the corrections resulting from the rest-mass expansion in [31, 32]. A third approach that employs non-relativistic quantum electrodynamics [39] (NRQED) has been developed, where the problematic divergences are canceled at the operator level. Korobov calculates with this method the binding energy of the ground state of helium in [23]. His result of 5945204223(42) MHz is closest to the measured value: 5945204212(6) MHz, however, the uncertainties in the present calculations are too big to decide if NRQED is a better alternative to predict the energy-structure of few electron atoms.

1.4 Motivation and outline of this thesis

The motivation of the work presented in this thesis is two-fold. The first is to improve the accuracy of the ground state energy in helium, in order to solve the disagreement between previous measurements [40, 41] of the ground state energy, and to perform a stringent QED test based on the latest theoretical results [23, 32, 30]. Secondly, the extension of the frequency comb technology towards higher photon energies is a

strong force behind the instrumental development reported here. The achievement of frequency comb accuracy at PHz frequencies holds the promise of more stringent tests of the QED theory using highly charged ions (see the previous section). Because no XUV or X-ray comb existed to date, such experiments achieved a much lower accuracy than frequency combs are capable of. A XUV frequency comb could change this. Helium has the highest transition frequencies (in the XUV) and biggest QED effects of all neutral atoms. Therefore the excitation of atomic (neutral) helium from the ground state using an XUV frequency comb can be viewed as a landmark, and as a stepping stone towards precision comb spectroscopy of highly charged ions.

In the following chapters the development and successful application of a frequency comb in the XUV near 51 nm is described. In chapter two, a theoretical background is given on the most important aspects of light propagation and light-matter interaction related to the work described in this thesis. This includes electromagnetic wave packets, frequency comb generation and applications, and the theory of high-harmonic generation in gases. This is followed by chapter 3, where the instrumental aspects of the experiment are discussed, including the FCL, noncollinear optical parametric chirped pulse amplification (NOPCPA), the principle and setups for measuring differential phase shifts in the NOPCPA process, and the harmonic generation and excitation setup. Chapter 4 reports on the investigation of the phase stability of amplification in a NOPCPA. In chapter 5 the extension of the NOPCPA to pulse pairs and the stability of their phase-relation is reported. Finally, in chapter 6 an extensive report on the spectroscopy of helium is presented, and the thesis is concluded with an outlook in chapter 7.

Chapter 2

Theoretical background

The experiments reported in this thesis make use of a range of nonlinear and linear phenomena, which occur in the interaction of light with matter. In this chapter, the terms used in this thesis are introduced with a focus on the employed experimental techniques. As a first step an introduction and overview over the theoretical aspects of linear and nonlinear electromagnetic pulse propagation is given in the following section. The latter sections of this chapter elaborate on the principles behind frequency combs and high harmonic generation (HHG).

This theoretical introduction is complemented by an instrumental approach to the used methods and techniques in the third chapter of this thesis.

Because the purpose is to introduce the used terms and phenomena, the complexity of the description is reduced by keeping the space one-dimensional and by assuming a scalar electric field for subjects, which do not suffer from this simplification. The role the magnetic part of the light fields plays in the experiments is negligible. Therefore, it will not be taken into account in the following treatments.

2.1 Electromagnetic waves and wave packets

Propagation of electromagnetic fields is governed by Maxwell's equations, which in general form the basis of classical electrodynamics. Many textbooks cover this field of physics. A comprehensive treatment of ultrashort-pulse propagation in particular is given in [42] and the basics of the field of nonlinear optics can be found in [43, 44]. As a starting point we consider linear propagation and interaction of electromagnetic waves in media. One can write down the wave equation in vacuum derived from the Maxwell equations, which takes the following form:

$$\frac{\partial^2}{\partial x^2}E(x,t) - \mu_0\epsilon_0\frac{\partial^2}{\partial t^2}E(x,t) = 0. \tag{2.1}$$

A solution of this equation is given by plane waves, which propagate at the speed of light: $c = 1/\sqrt{\mu_0\epsilon_0}$. A general solution can be written as a sum of plane waves, propagating in opposite directions along the x-axis:

$$E(x,t) = Ae^{i(kx-\omega t)} + Be^{-i(kx+\omega t)}. \tag{2.2}$$

The waves described with this equation oscillate at the angular frequency ω. The wavenumber k expresses the spatial dimension of this oscillation, connecting it with the velocity of the wave: $k = \omega/c$. The linear equation 2.1 is solved by every superposition of the solutions given in 2.2. The general form results in wave packets which arise from the integration over a spectral range in the frequency domain:

$$E(x,t) = \int_{-\infty}^{\infty} A(\omega)e^{i(kx-\omega t)}d\omega + \int_{-\infty}^{\infty} B(\omega)e^{-i(kx+\omega t)}d\omega, \tag{2.3}$$

where $A(\omega)$ and $B(\omega)$ are spectral amplitudes of waves traveling in opposite directions. The first integral describes a wave packet, propagating in the positive x-direction. Assuming a moderately wide spectrum, which peaks around a frequency ω_c, this allows to expand $A(\omega)$ around a central frequency ω_c and wavenumber $k = k_c + \delta k$, so that the following equation is obtained:

$$\begin{aligned} E(x,t) &= \int_{-\infty}^{\infty} A(\omega-\omega_c)e^{i(k_c+\delta k)x}e^{-i(\omega+\omega_c)t}d\omega \\ &= e^{i(k_cx-\omega_ct)}\int_{-\infty}^{\infty} A(\omega-\omega_c)e^{i\delta k}e^{-i\omega t}d\omega \\ &= A(x,t)e^{i(k_cx-\omega_ct)}. \end{aligned} \tag{2.4}$$

The wave packet is represented here by a single-frequency carrier which is modulated by an envelope function $A(x,t)$. This temporal envelope is related to the spectrum $A(\omega)$ by means of Fourier transformation. In vacuum it propagates along the x-direction with the velocity of light c without changing its shape. The next step is to consider the more general situation of the behavior of electromagnetic wave packets in media.

Waves and pulses in media

The influence of a traversed medium is taken into account by introducing the polarization $P(x,t)$ induced by the electric field into wave equation 2.1:

$$\frac{\partial^2}{\partial z^2}E(x,t) - \mu_0\epsilon_0\frac{\partial^2}{\partial t^2}E(x,t) = \mu_0\frac{\partial^2}{\partial t^2}P(x,t). \tag{2.5}$$

Assuming first only a linear dependence of the polarization $P(x,t)$ on the electric field, one can write:

$$P(x,t) = \epsilon_0\int_{-\infty}^{\infty}\chi_e(t)E(x,t-t')dt', \tag{2.6}$$

with χ_e being the electric susceptibility of the medium. If the response of the medium is instantaneous, equation 2.6 simplifies to $P(x,t) = \epsilon_0\chi_e E(x,t)$. The perspective of a one-dimensional space with an isotropic medium adopted here is oversimplified. χ_e of an anisotropic medium in three dimensions is a rank 2 tensor, which couples the polarizability along the optical axes of the medium to all the components of the electric-field vector. However, this introduction to electromagnetic waves and pulses rather benefits from reducing the complexity of the problem.

Viewed in the frequency domain the polarization becomes $P(x,\omega) = \epsilon_0\chi_e E(x,\omega)$, with $E(x,\omega) = A(\omega)e^{-ikx}$. This allows to write equation 2.5 as:

$$\frac{\partial^2}{\partial x^2}E(x,\omega) + [1+\chi_e(\omega)]\frac{\omega^2}{c^2}E(x,\omega) = 0. \tag{2.7}$$

This equation is solved by assuming plane waves of the following shape:

$$E(x,t) = Ae^{i(k(\omega)x-\omega t)} + Be^{-i(k(\omega)x+\omega t)}, \tag{2.8}$$

which propagate with a frequency dependent phase velocity $v_{ph}(\omega) = c/\mathrm{Re}(n(\omega))$, where $n(\omega) = \sqrt{1+\chi_e}$ is the material-specific complex index of refraction. The wavenumber is related to $n(\omega)$ by the following equation:

$$k(\omega) = n(\omega)\frac{\omega}{c}. \tag{2.9}$$

With the absorption coefficient $\alpha(\omega) = \mathrm{Im}(k(\omega))$, and discarding one of the possible propagation directions, the plane-wave solutions can be written as:

$$E(x,t) = Ae^{-\alpha(\omega)x}e^{i(\omega x/v_{ph}(\omega)-\omega t)}. \tag{2.10}$$

Replacing the complex wavenumber $k(\omega)$ by the absorption coefficient $\alpha(\omega)$ and the phase velocity v_{ph} allows an insightful view at the propagation of monochromatic waves through linear media. We see that a wave can be attenuated or amplified (depending on the sign of $\alpha(\omega)$) and that the phase-velocity of light is a medium-dependent function of frequency.

As a next step the behavior of wave packets in linear media is considered. From equation 2.8 a wave packet can be formed, resembling the previous approach in vacuum (equation 2.3):

$$E(x,t) = \int_{-\infty}^{\infty} A(\omega)e^{i(k(\omega))x-\omega t)}d\omega. \tag{2.11}$$

Expanding the frequency around the carrier ω_c and the corresponding wave number $k(\omega) = k_c + \delta k(\omega)$ yields:

$$\begin{aligned} E(x,t) &= e^{i(k_c x-\omega_c t)}\int_{-\infty}^{\infty} A(\omega-\omega_c)e^{i\delta k(\omega)x}e^{-i\omega t}d\omega \\ &= A(x,t)e^{i(k_c x-\omega_c t)}, \end{aligned} \tag{2.12}$$

where $A(x,t)$ is generally a complex function connected to the spectrum of the considered wave packet by Fourier transformation. Knowledge of the spectral amplitudes and phases allows reconstruction of the wave packet in the time domain and vice versa. Some insight can be gained at this stage by considering two very simple spectra. The first one, in the form of a delta function $A(\omega) = A_0\delta(\omega-\omega_c)$, appears with a constant envelope in the time domain: $E(x,t) = A_0e^{i(k_c x-\omega_c t)}$. This means basically that the amplitude of monochromatic waves remains constant. A

more interesting example is a Fourier-limited spectrum* in the form of a Gaussian with the amplitude A_0 as:

$$A(x,\omega) = A_0(x)e^{-\frac{(\omega-\omega_c)^2}{2\Gamma_e^2}}, \tag{2.13}$$

with Γ_e being the half width of the spectrum at the $e^{-1/2}$-level of the amplitude A_0. Fourier transformation yields again a Gaussian profile of a pulse in the time domain:

$$A(x,t) = A_0(x)e^{-\frac{(t-t_0)^2}{2t_e^2}}, \tag{2.14}$$

where the pulse duration t_e relates to the spectral width Γ_e according to the so called *time-bandwidth product*: $t_e \times \Gamma_e \approx 0.64$. The spectral (and temporal) full width at half maximum $\Gamma_{1/2}$ ($t_{1/2}$) is obtained from: $\Gamma_{1/2} = \sqrt{2\ln 2}\Gamma_e$. The time-bandwidth product is a constant in the order of one for Fourier-limited pulses. The exact value varies according to the spectral (temporal) shape of the pulse. In practice this reciprocal relation between the bandwidth and the duration of a pulse is employed to generate short and powerful light pulses by distributing the light from a laser over a broad phase-locked spectrum. The light field of a state-of-the-art femtosecond oscillator, which emits in a 100 nm-wide spectrum centered around 800 nm at 1 W in 10 fs pulses at a repetition rate of 100 MHz, reaches a peak power of 1 MW. Amplifier systems at low repetition rate can reach peak powers of at least 1 PW [45], which (for the very short time of the pulse) is more powerful than all the power plants on earth combined.

Ultrafast pulsed lasers have therefore attracted a lot of attention from researchers interested e.g. in high field physics or nuclear fusion. With their high power and intensity levels, ultrashort pulse laser systems have become the workhorse in the field of nonlinear optics, revealing the occurrence of many unexpected phenomena. But before considering nonlinear interaction between light and matter, lets first take a look at the effects that linear polarization of matter has on traveling light wave packets.

*That is a spectrum in which the phase is a strictly linear function of the carrier frequency.

Pulse propagation in a linear medium with dispersion

For the description of electromagnetic wave packets in media, the pulse is considered in terms of carrier-wave and a pulse-envelope. Assuming that the envelope is a slowly varying function of x and t[†] (*the slowly varying envelope approximation*), one can neglect higher order derivatives in equation 2.7. We then obtain:

$$\left(\frac{\partial^2}{\partial x^2} + (1+\chi_e)\frac{\omega^2}{c^2}\right) A(x,\omega) e^{-i(k_c x - \omega_0 t)} = 0. \tag{2.15}$$

Leibniz law and division by the carrier wave yields:

$$\frac{\partial^2 A(x,\omega)}{\partial x^2} - 2ik_c \frac{\partial A(x,\omega)}{\partial x} - k_c^2 A(x,\omega) + (1+\chi_e)\frac{\omega^2}{c^2} A(x,\omega) = 0. \tag{2.16}$$

The second order derivative can be neglected in the slowly varying envelope approximation. To simplify things further a transparent medium is assumed, so that: $k^2(\omega) = (1+\chi_e)\omega^2/c^2$. Another assumption (which is reasonable in a transparent medium) made for the variation of $k(\omega)$ around k_c is that it is small in comparison to k_c. With these approximations equation 2.16 simplifies to:

$$\frac{\partial A(x,\omega)}{\partial x} + \frac{i}{2k_c}(k^2(\omega) - k_c^2) A(x,\omega) = 0. \tag{2.17}$$

In order to find a form which simplifies Fourier transformation into the time domain, $k(\omega)$ is expanded around ω_c, using $k(\omega) + k_c \approx 2k_c$:

$$\begin{aligned} k^2(\omega) - k_c^2 &\approx 2k_c(k - k_c) \\ &= 2k_c\left(k_c + \left.\frac{\partial k}{\partial \omega}\right|_{\omega_c}(\omega-\omega_c) + \frac{1}{2}\left.\frac{\partial^2 k}{\partial \omega^2}\right|_{\omega_c}(\omega-\omega_c)^2 + \cdots - k_c\right) \\ &= 2k_c\left(\sum_{n=1}^{\infty}\frac{1}{n!}k^{(n)}(\omega-\omega_c)^n\right), \end{aligned} \tag{2.18}$$

[†]which is given for pulses with a bandwidth Γ_e that is significantly smaller that their central frequency ω_c. For a central wavelength of 800 nm this is the case for pulses with a Fourier-limited duration of more than 100 fs.

with the notation $k^{(n)} = \frac{\partial^n k(\omega)}{\partial \omega^n}\Big|_{\omega_c}$. Equation 2.17 now becomes:

$$\frac{\partial A(x,\omega)}{\partial z} + i\Big(\sum_{n=1}^{\infty} \frac{1}{n!} k^{(n)} (\omega - \omega_c)^n\Big) A(x,\omega) = 0. \tag{2.19}$$

Fourier transformation yields a differential equation for the slowly varying envelope in the time domain:

$$\frac{\partial A(x,t)}{\partial x} - \sum_{n=1}^{\infty} \frac{(-i)^{n+1}}{n!} k^{(n)} \frac{\partial^n A(x,t)}{\partial t^n} = 0. \tag{2.20}$$

The assumed slowly varying pulse envelope allows again to discard the higher-order derivatives and we are left with the following simplified form of the equation, often referred to as the *parabolic wave equation* in literature [46]:

$$\frac{\partial A(x,t)}{\partial x} + k^{(1)} \frac{\partial A(x,t)}{\partial t} - \frac{ik^{(2)}}{2} \frac{\partial^2 A(x,t)}{\partial t^2} = 0. \tag{2.21}$$

The approximations made to arrive at 2.21 make the equation suitable only for many-cycle (>100) pulses. In order to deal with shorter pulses, higher order derivatives from equation 2.20 should be included.

Once we have a solution to the wave equation 2.5 for a given point in time, $E(\tau)$, the evolution of the wave packet can be determined in a very convenient way using the Green function formalism [42]. As a first step the wave packet from equation 2.11 is taken. Fourier transformation of $A(\omega)$ therein into the time domain yields:

$$\begin{aligned} E(x,t) &= \int_{-\infty}^{\infty} \frac{1}{2\pi} \int_{-\infty}^{\infty} E(\tau) e^{i\omega\tau} d\tau e^{ik(\omega)x} e^{-i\omega t} d\omega \\ &= \frac{1}{2\pi} \int_{-\infty}^{\infty} E(\tau) \int_{-\infty}^{\infty} e^{ik(\omega)x} e^{-i\omega(t-\tau)} d\omega d\tau \\ &= \int_{-\infty}^{\infty} E(\tau) G(t-\tau) d\tau \end{aligned} \tag{2.22}$$

$$\text{with}: G(t-\tau) = \frac{1}{2\pi} \int_{-\infty}^{\infty} e^{ik(\omega)x} e^{-i\omega(t-\tau)} d\omega. \tag{2.23}$$

The Green function $G(t-\tau)$ in equation 2.22 propagates the initial field $E(\tau)$ along the x-axis, starting from the point $x = 0$. It can be used to show the effects of propagation through a dispersive medium on the carrier wave of a short pulse. For this the wavenumber $k(\omega)$ is expanded again as done in Eq. 2.18, but keeping only the first two terms: $k(\omega) = k_c + k^{(1)}(\omega - \omega_c)$. The field at a distance x follows from 2.22:

$$\begin{aligned} E(z,t) &= \frac{1}{2\pi}\int_{-\infty}^{\infty} E(\tau)\int_{-\infty}^{\infty} e^{i[k_c+k^{(1)}(\omega-\omega_c)x]}e^{-i\omega(t-\tau)}d\omega d\tau \\ &= e^{i(k_c-k^{(1)}\omega_c)x}\int_{-\infty}^{\infty} E(\tau)\delta(\tau - t + k^{(1)}x)d\tau) \\ &= e^{i(k_c-k^{(1)}\omega_c)x}E(t-k^{(1)}x). \end{aligned} \tag{2.24}$$

This result shows that linear dispersion does not change the shape of the pulse-envelope. Inserting the previously introduced phase velocity $v_{ph} = \omega_c/k_c$ and a group velocity, given by: $v_g = 1/k^{(1)}$ puts the equation 2.24 in a more readable form:

$$E(z,t) = e^{i(\frac{1}{v_{ph}}-\frac{1}{v_g})\omega_c x}E(t-\frac{x}{v_g}). \tag{2.25}$$

It becomes clear here, that the velocity of a pulse in a medium is generally not identical with the velocity at which the carrier propagates. As a result the carrier wave constantly moves underneath the envelope while the pulse propagates. This is of particular importance for the frequency comb laser, which is a major topic in this thesis and will be discussed in more detail in the following section.

In the previous example only the linear part of the material-related dispersion was considered. In this simple case the shape of the pulse envelope remains constant, while the carrier exhibits a phase shift, related to the linear dispersion in the traversed medium. The situation becomes more complex if higher-order terms are present in the medium (and in the analysis). In order to investigate the effect of the second order dispersion, the linear term is omitted in the following. The wavenumber is now expanded to: $k(\omega) = k_c + \frac{k^{(2)}}{2}(\omega - \omega_c)^2$ and a Gaussian shape is assumed for the initial field $E(\tau)$ in the integral 2.22.

$$
\begin{aligned}
E(x,t) &= \frac{1}{2\pi}\int_{-\infty}^{\infty} e^{-\frac{\tau^2}{2t_e^2}} \int_{-\infty}^{\infty} e^{i[k_c+\frac{k^{(2)}}{2}(\omega-\omega_c)^2]x} e^{-i\omega(t-\tau)} d\omega d\tau \\
&= \frac{1}{2\pi}\int_{-\infty}^{\infty} e^{-\frac{\tau^2}{2t_e^2}} \int_{-\infty}^{\infty} e^{i[\frac{k^{(2)}}{2}x\omega^2+(\tau-t-k^{(2)}x\omega_c)\omega]} d\omega d\tau \\
&= \frac{1}{\sqrt{2\pi i k^{(2)}x}}\int_{-\infty}^{\infty} e^{-\frac{\tau^2}{2t_e^2}} e^{\frac{k^{(2)}}{2}x(\tau-t)^2} d\tau \\
&= \frac{t_e}{\sqrt{t_e^2+ik^{(2)}x}} e^{-\frac{\tau^2}{2t_x^2}+i\phi(t)}. \qquad (2.26)
\end{aligned}
$$

Note that constant phase terms have been neglected in this derivation. The pulse in a quadratically dispersive medium keeps its Gaussian shape, but is stretched in time according to:

$$
t_x = t_e\sqrt{1+\left(\frac{k^{(2)}x}{t_e^2}\right)^2}. \qquad (2.27)
$$

After traveling a distance long enough to satisfy: $k^{(2)}x \gg t_e^2$ the pulse duration can be approximated with $t_x \approx k^{(2)}xt_e^{-1}$, or using the time-bandwidth product of a Fourier-limited Gaussian pulse: $t_x \approx \frac{1}{2}k^{(2)}x\Gamma_e$. The time-dependent phase factor $\phi(t)$ describes the way the phase of the carrier wave is modulated:

$$
\phi(t) = \frac{t_e^2}{2k^{(2)}xt_x^2}t^2. \qquad (2.28)
$$

The quadratic time dependence of this term reflects a linear time dependence of the carrier frequency ω, which is the time-derivative of the phase. The pulse becomes linearly *chirped*. The amount of chirp depends on the type and amount of material traversed by the pulse.

More complicated dispersive behavior, which plays a bigger role with increasing spectral width of the pulse, is tackled using higher order dispersion terms $k^{(n)}$, with $n > 2$. These terms distort the shape of the pulse often in an asymmetric way, e.g. third-order dispersion (TOD) forms trains of pre- or after-pulses (depending on the sign of the TOD)

and introduce frequency chirps with a nonlinear time dependence along the pulse. However, because of the relatively narrow spectral bandwidth of the pulses used in the experiments described in this thesis, these effects are not considered further. Note that also a description of attenuation and amplification has been omitted in this derivation.

Pulse propagation in a nonlinear medium

In the previous section a linear response of a medium exposed to electromagnetic waves was considered. This treatment is an approximation which does not take into account a possible non-linear response of the medium to the electric field of the light. Higher-order dependencies become more important for the large electric fields that can easily be reached with ultrashort laser pulses. Considering only an immediate response of the medium allows to expand the polarization of the medium (equation 2.6) to:

$$\mathbf{P} = \epsilon_0(\chi^{(1)}\mathbf{E} + \chi^{(2)}\mathbf{EE} + \chi^{(3)}\mathbf{EEE} + \cdots), \tag{2.29}$$

where $\chi^{(n)}$ is a rank $n+1$ tensor called the n^{th}-order susceptibility. This approach is generally valid in the perturbative regime, where the intensity of the light field is smaller than 10^{12} W/cm^2. Nonlinear phenomena beyond this intensity require a different treatment. In the previous chapter some basic effects of $\chi^{(1)}$ like e.g. absorption, dispersion and the carrier-envelope phase shift were discussed for one dimension. Although the even-order susceptibilities disappear in isotropic media, the non-zero $\chi^{(2)}$ found in birefringent crystals is used e.g. for frequency doubling, the Pockels effect, frequency mixing and especially the parametric amplification, which will be inspected more closely in the next chapter.

Effects associated with $\chi^{(3)}$ do not rely on on an anisotropy of the medium. Assuming a material can be described by only the first and third-order susceptibility, wave equation 2.7 takes the following form[‡]:

$$\nabla^2\mathbf{E}(\mathbf{r},\omega) + [1 + \chi_e^{(1)}(\omega) + \chi_e^{(3)}(\omega)|\mathbf{E}(\mathbf{r},\omega)|^2]\frac{\omega^2}{c^2}\mathbf{E}(\mathbf{r},\omega) = 0. \tag{2.30}$$

[‡]this time incorporating all three spatial dimensions

The third-order susceptibility is responsible for e.g third harmonic generation, self-phase modulation, self focusing and four-wave mixing. At this place the nonlinear refractive index $n_2(\omega)$ can be introduced as:

$$n(\omega) = \sqrt{1 + \chi_e^{(1)} + \chi_e^{(3)}}|\mathbf{E}(\mathbf{r},\omega)|^2 \approx n + n_2|E|^2. \tag{2.31}$$

This approximation, together with those used to derive equation 2.21, makes it possible to write the evolution of the pulse-envelope $A(x,t)$ as:

$$\frac{\partial A(x,t)}{\partial x} + k^{(1)}\frac{\partial A(x,t)}{\partial t} - \frac{ik^{(2)}}{2}\frac{\partial^2 A(x,t)}{\partial t^2} = \frac{in_2\omega_c}{c}|A|^2 A(x,t). \tag{2.32}$$

This differential equation is a slightly modified form of what is frequently called the *nonlinear Schrödinger equation*. It differs by an attenuation/amplification term, which has been omitted here. The approximations, used to derive this equation limit its validity for optical pulses with durations > 0.1 ps. However, its relatively simple form allows to gain insight into the nonlinear interaction of strong pulses propagating in media.

Let us now consider only the nonlinear response, skipping the dispersion-related terms. Equation 2.32 then becomes:

$$\frac{\partial A(x,t)}{\partial x} = \frac{in_2\omega_c}{c}|A|^2 A(x,t), \tag{2.33}$$

which is solved by:

$$A(x,t) = A(0,t)e^{i\omega_c n_2|A(x,t)|^2 x/c}. \tag{2.34}$$

The pulse envelope is not affected by the Kerr non-linearity, but the phase of the carrier wave exhibits a phase shift $\delta\phi = \omega_c n_2|A(x,t)|^2 x/c$, which is proportional to the nonlinear refractive index n_2, as well as the length x of the passed material and the field intensity. The dependence on the intensity results in a time-dependent phase-shift along the pulse and gives rise to the name of this non-linear effect: *self-phase modulation*. It is interesting to take a look at the derivative of the modulated carrier phase, which is[§]:

[§]assuming an initially Fourier-limited pulse interacting with the non-linear medium

$$\omega = -\frac{d\delta\phi}{dt} = \omega_c - \frac{\omega_c n_2 x}{c}\frac{d}{dt}|A(x,t)|^2. \tag{2.35}$$

This means for pulses traveling in materials with a positive n_2 that their carrier frequency will be reduced in the leading, and increased in the trailing edge. New frequency components will be generated and as a result the spectrum of the pulse broadens. If such a spectrum can be compressed (brought closer to the Fourier limited case), shorter pulses can be generated. This has been successfully employed e.g. in [47] to create pulses with two optical cycles FWHM duration (5.0 fs at 800 nm), starting from a duration of 20 fs.

While self-phase modulation only broadens the spectrum of an intense pulse, n^{th}-order susceptibilities facilitate the production of new frequency components at n^{th}-order harmonic frequencies of the fundamental. The powers in which the electric field appears in equation 2.29 implicate harmonic radiation for odd n, while even orders are possible in non-centro-symmetric materials, such as those exhibiting birefringence. The second harmonic of an optical frequency was generated for the first time in quartz by Franken et al. in 1961 [48] with a ruby laser. Boyd shows [43] that the magnitude of $\chi^{(n)}$ can be approximated by:

$$\chi_e^{(n)} \approx \frac{\chi_e^{(1)}}{E_a^n}, \tag{2.36}$$

with E_a being the field in the vicinity of the electrons residing in the ground state of the medium. This means for electric fields which are much smaller than E_a, that the nonlinear polarization will be dominated by the lowest orders of the expansion. The yield of the harmonics will decrease exponentially with the harmonic order as:

$$P(n\omega_c) \propto \left(\frac{E(\omega_c)}{E_a}\right)^n. \tag{2.37}$$

In fact, fields comparable to E_a lead to ionization of the medium and related effects, and thus can not be treated in a perturbative approach. For instance, the process of high harmonic generation (applied in the experiments described in the later chapters), occurs in the non-perturbative

regime for intensities $I > 10^{12}$ W/cm^2, and therefore requires a different approach, which is presented in section 2.4. But first the principle of frequency combs is explained, which employs mainly phenomena, that take place in the perturbative regime.

2.2 Frequency-comb lasers

The invention of the frequency comb laser (FCL) in the year 2000 brought about a revolution in metrology [9, 10]. The first optical frequency combs bridged the gap between radio- (typically tens to hundreds of MHz) and optical frequencies (typically hundreds of THz). Because of that, precise frequency measurements in the optical domain were almost immediately improved by an order of magnitude and more [49, 50]. Soon the wavelength range covered by these lasers was extended down to the the mid- and far infrared frequency region [51] and recently to frequencies of the order of THz [52]. FCLs in the UV and VUV have been demonstrated in [19, 17] and more recently in [53].

Besides frequency metrology and the closely related field of high-precision spectroscopy, the frequency comb laser was applied for distance measurements [54], laser noise characterization [55], cooling of molecules [56] and shows good prospect for telecommunication [57]. Recently the performance of the best atomic clocks has been investigated, using a FCL as a gear wheel [11].

The basic principles behind FCLs are introduced in this section particularly with regard to the instrument employed in the experiments described in this thesis.

Principles behind frequency-comb lasers

A laser that emits pulses at a fixed repetition rate $f_{rep} = 1/\tau$ and carrier-envelope phase-shift $\Delta\phi$ between consecutive pulses exhibits a comb of narrow equidistant modes in its spectrum (see Fig 2.1). The carrier-envelope phase-shift $\Delta\phi$ is defined here as the difference in the phase of the carrier-wave at the maxima of the pulse-envelopes of consecutive pulses from the FCL. The spectrum of such a laser can be derived mathematically by means of Fourier transformation of the pulse train emitted

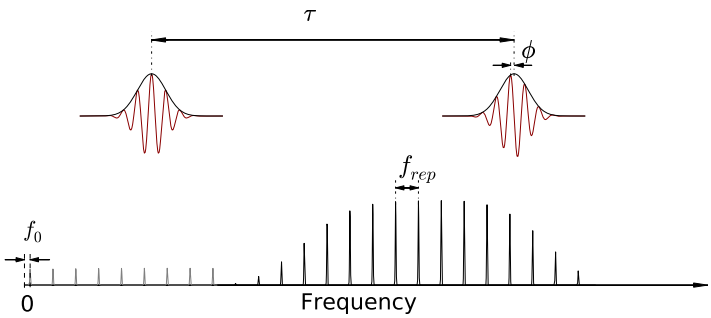

Figure 2.1: The basic principle of a frequency comb source: an infinite train of equidistant pulses emitted at the frequency $f_{rep} = 1/\tau$ with a fixed carrier-envelope phase shift between consecutive pulses $\Delta\phi$ (here $= \phi_{\mathrm{CEO}} = \pi/2$, the carrier-envelope phase offset) exhibits a spectrum of equidistant narrow lines, separated by the repetition rate f_{rep}. These lines are shifted with respect to the integer multiples of f_{rep} by the offset-frequency $f_0 = f_{rep} \times \Delta\phi/2\pi$.

by this device. The electric field of such a pulse train at a fixed location can be written as [58]:

$$E(t) = \sum_{m=0}^{\infty} \hat{E}(t - m\tau) e^{i(\omega_c t + m(\Delta\phi - \omega_c \tau) + \phi_0)}, \tag{2.38}$$

where $\hat{E}(t) = \hat{E}(t - m\tau)$ is the single pulse envelope, ω_c the carrier frequency and ϕ_0 the carrier-envelope phase-offset of the first pulse ($m = 0$). The corresponding spectrum is:

$$E(\omega) = e^{i\phi_0} \sum_{m=0}^{\infty} e^{i(m\Delta\phi - m\omega\tau)} \tilde{E}(\omega - \omega_c), \tag{2.39}$$

with $\tilde{E}(\omega) = \int \hat{E}(t) e^{-i\omega t} dt$. This equation is non-zero for frequencies, at which the exponentials add coherently. For those frequencies the phase shift between consecutive pulses is an integer multiple of 2π which is equivalent with: $\Delta\phi + \omega\tau = 2n\pi$. These frequencies satisfy the equation:

$$\omega_n = \frac{\Delta\phi}{\tau} + \frac{2n\pi}{\tau}, \tag{2.40}$$

or, with $f_0 = \frac{\Delta\phi}{2\pi} f_{rep}$:

$$f_n = f_0 + n f_{rep}. \tag{2.41}$$

This equation shows a spectrum of equidistant lines, separated by the repetition frequency f_{rep} of the FCL and offset from integer multiples of f_{rep} by the so called offset-frequency f_0. The offset frequency is determined by the pulse-to-pulse carrier-envelope phase-shift. While f_{rep} can easily be measured with a photo diode and stabilized to a radio frequency by correcting the length of the oscillator cavity with e.g a piezoelectric crystal in a PID loop, detection and stabilization of the f_0 was a revolutionary step, which became possible after the invention of micro-structured photonic fibers [59]. Using a photonic fiber, octave-spanning spectra which maintain the original comb structure can be generated from ultrashort pulses. This technique allows the offset frequency f_0 to be detected in the form of an interference beat signal. To this end the 'red' part of the (broadened) spectrum is frequency doubled so that it can interfere with the 'blue' part of the spectrum. This so called $f-2f$ technique (see Fig. 2.2) produces a beat at f_0 as the offset frequency of the frequency-doubled light amounts to twice that of the original spectrum. With this method the first self-referenced FCLs were built in JILA, Boulder [60, 9] and at the MPQ, Munich [10]. To control the measured offset-frequency f_0, the spectrum was spatially dispersed in the cavity and reflected of a high-reflector end-mirror mounted on a piezoelectric transducer. Tilting this end-mirror with the piezo introduced a linear dispersion in the pulse spectrum, thereby changing the carrier-envelope phase shift in the cavity (see Eq. 2.25). The repetition-frequency was controlled by longitudinal translation of the end mirror. Nowadays f_0 is typically controlled via the pump laser power, which has a strong influence on the carrier-envelope phase shift in the commonly used Kerr-lens modelocked Ti:sapphire laser [61, 62]. Another interesting scheme of f_0-stabilization, where the measured offset frequency is subtracted from the light field using an acousto-optic modulator, was recently demonstrated in [63].

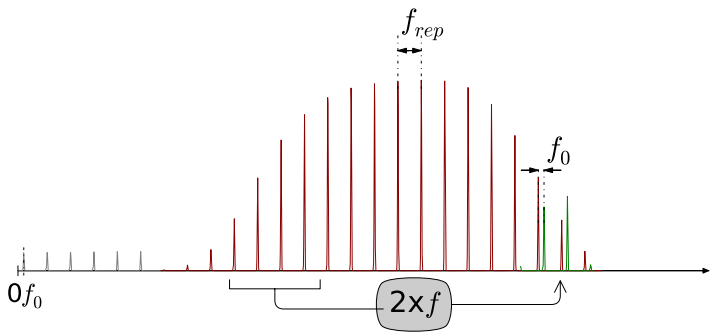

Figure 2.2: Frequency-doubling the 'red wing' of a more than one octave wide frequency comb yields another frequency comb allocated in the 'blue wing'. The offset frequency of the generated comb is twice as large as the original, which allows to find it in a beat signal between the doubled and the fundamental frequency comb.

2.3 Spectroscopy with frequency combs

Due to the amazing properties of frequency comb lasers they found a wide variety of interesting applications already in the first decade of their existence. Some of these applications have been mentioned in section 2.2. With regard to the subject of this thesis it is appropriate to take a closer look at the various uses of spectroscopy with FCLs. The unique frequency and timing accuracy made possible with FCLs in the optical domain is used in two different ways in spectroscopy. In some experiments the comb-like spectrum is used to calibrate the frequency of a narrow-band laser that is used for spectroscopy. We refer to this approach as classical frequency comb spectroscopy, in contrast to direct frequency comb spectroscopy, where the FCL is used to directly excite an atomic or molecular transitions. This thesis reports on a realization of the second approach.

Spectroscopy calibrated with frequency combs

The development of the FCL finds its roots in the field of precision spectroscopy, where the first ideas emerged to use modelocked lasers in the 1970s. Eckstein et al. used a comb structure from a mode locked laser

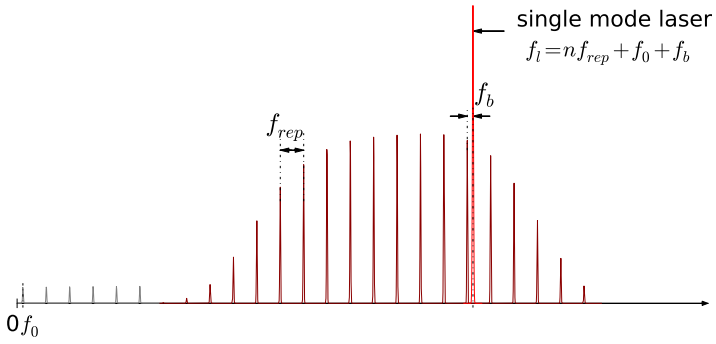

Figure 2.3: Measurement of a cw-laser frequency f_l using the beat-signal f_b with a FCL.

in 1978 for relative frequency measurements on the fine-structure splitting in sodium [64]. The first self-referenced FCLs with full f_0 and f_{rep} control were therefore naturally employed in spectroscopy to measure (and confirm) the frequencies of continuous sources [60] and of a frequency chain [10] previously used in a hydrogen spectroscopy measurement. These optical-frequency measurements resemble a spectroscopic approach, where an auxiallary narrow-band laser, with a known frequency is tuned over a resonance. The frequency comb can be used to measure and monitor the frequency of the tunable laser, calibrating this way the obtained spectrum. This frequency is detected, analogously to the $f - 2f$-scheme, with the beat-signal f_b between the spectroscopy laser and the frequency comb. Figure 2.3 illustrates, how a single-mode laser frequency f_l is obtained from such a measurement. If the measured resonance is known with sufficient accuracy (much) better than the repetition rate f_{rep} of the FCL¶, the calibration is obtained instantaneously from:

$$f_l = \pm f_0 + n f_{rep} \pm f_b. \tag{2.42}$$

The sign of the beat frequency f_b follows together with n from the initial accuracy of the measured resonance. It can also be found by tuning f_{rep}. Similarly if the initial accuracy is not sufficient to determine n,

¶ This error should include the systematic uncertainties of the measurement. To be safe a standard deviation of one tenth of the repetition frequency is sufficient for an unambiguous determination of f_l.

then it is possible to repeat the calibration at different repetition rates of the FCL and still obtain an unambiguous result by looking for the coincidence point which identifies the proper mode number $n(f_{rep})$, where all measurements result in the same f_l.

Direct frequency-comb spectroscopy

The previous section described how spectroscopic experiments are calibrated with FCLs, which bridge the frequency gap between the state-of-the-art atomic clocks operating at radio frequencies and the optical frequency range. In a slightly different approach, a FCL can be used directly to measure a resonance, omitting a tunable continuous source for the spectroscopy.

A frequency comb source can be perceived as an ensemble of phase-locked cw-lasers, emitting a comb of equidistant frequencies in the same beam. The lower part of figure 2.1 illustrates this point of view, but for visualization purposes the number of modes is kept quite low (in other words, the FCL is pulsing at a unrealistic high rate compared to the carrier-frequency of the emitted pulses). A more realistic source, that emits 30 fs long 800 nm Gaussian pulses at $f_{rep} = 100$ MHz contains ≈ 150000 cw frequencies within the FWHM of its spectrum. The mode numbers n in the comb-equation 2.41 enumerating the frequencies is on the order of 4 million for such a comb at 800 nm.

The electronic access to the frequencies f_0 and f_{rep} allows to scan the modes. Changing f_0 results in a constant shift of all the modes simultaneously. Alternatively, it is possible to change f_{rep} to scan the modes. As can be seen from the comb-equation 2.41, in this case also the distance between the modes changes during a scan. For instance, changing the repetition rate by ≈ 27 Hz in the example of a FCL mentioned above, brings the frequency of the modes to the positions previously occupied by their neighbors.

Direct frequency comb metrology is performed by exciting a resonance directly with a mode from a FCL. Scanning the comb spectrum over such resonance yields a periodic signal in which the comb-spectrum is convoluted with the response of the measured system[‖]. The interpre-

[‖] Comprising the width and shape of the resonance and the instrument related systematic effects, which affect the shape of the signal.

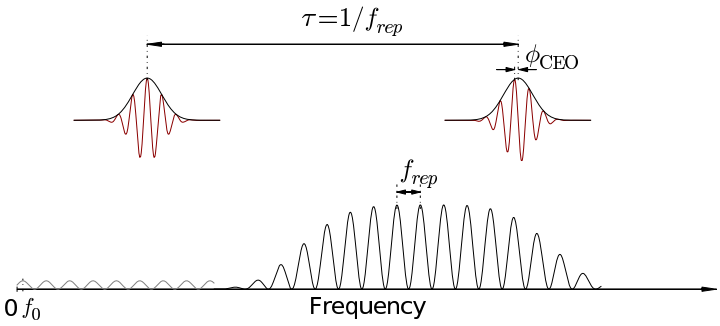

Figure 2.4: The principle of a frequency comb formed by two pulses separated by τ with a carrier-envelope phase shift between consecutive pulses ϕ_{CEO}. The spectrum looks like is a cosine-modulated continuum with its maxima separated by the repetition rate f_{rep}. As in the case of an infinite pulse train these maxima are shifted with respect to the integer multiples of f_{rep} by an offset-frequency $f_0 = f_{rep} \times \Delta\phi/2\pi$.

tation of such a measurement requires to identify the number(s) n of the mode(s) actually responsible for the excitation. This is again fairly trivial (provided all systematic effects are known), if the resonance is known better than the repetition rate of the FCL. If this information is not available, similarly to the measurement of a laser frequency, the position of the investigated resonance can be deduced by remeasuring the transition with various repetition rates until only one set of mode numbers results in a frequency, that is consistent for all the used repetition rates. The latter approach was used in the measurements [19, 65] and also in the experiments reported here.

The measurements presented in this thesis represent a particular form of direct frequency comb spectroscopy with only two phase-coherent pulses. In contrast to the frequency comb formed by an infinite train of equidistant phase-locked pulses, we generate a comb in the XUV by means of harmonic upconversion of an infrared-pulse pair. The spectrum of such a pulse-pair in the infrared resembles a cosine-modulated continuum, with maxima of the cosine wave sitting at the frequencies predicted by the comb equation $f_n = nf_{rep} + f_0$. Figure 2.4 illustrates together with Fig. 2.1 the similarity between a two-pulse frequency comb and the previously introduced FCL.

2.4 An analysis of the interaction of a two-level system with a phase-locked pulse-pair

The time-domain representation

In view of the experiments reported in this thesis, a model for resonant excitation of an electronic transition by two phase-locked pulses is given here. The helium atom is modeled as a two-level system, which is justified because the spectrum of the pulses used in the experiments reported here is too narrow-band to excite more than one transition. Such a system can be described with the state vector $|\psi_t\rangle = c_1(t)|1\rangle + c_2(t)|2\rangle = \begin{pmatrix} c_2(t) \\ c_1(t) \end{pmatrix}$, where $|n\rangle (n = 1, 2)$ are the two energy-eigenstates of the system that correspond to the ground and the excited state with energy $E_2 > E_1$. The coefficients $c_n(t)$ describe the evolution of the probability amplitudes of these eigenstates.

The Hamiltonian can be expressed as a sum of the free atom Hamiltonian H_0 and a laser-field interaction term V.

Let us consider the interaction of a short pulse $\mathbf{E}(x,t) = \mathbf{A}e^{-i\omega_l t} + c.c.$ with this system, in which a transition between the two states is resonantly excited. The pulse envelope is approximated by a flat top shape for the duration τ and zero everywhere else. The interaction term of the Hamiltonian can be then expressed as a product of the dipole moment operator $\mathbf{d}_{21}$ that connects the two eigenstates and the electric field $\mathbf{E}(x,t)$ of the pulse:

$$\begin{aligned} V &= -\mathbf{d} \cdot \mathbf{E} \\ &= -(\mathbf{d}_{21}|2\rangle\langle 1| + \mathbf{d}_{21}^*|1\rangle\langle 2|) \cdot (\mathbf{A}(x)e^{-i\omega_l t}) + \mathbf{A}^*(x)e^{i\omega_l t}) \\ &= -\hbar(\Omega e^{-i\omega_l t} + \tilde{\Omega}e^{i\omega_l t})|2\rangle\langle 1| - \hbar(\tilde{\Omega}^* e^{-i\omega_l t} + \Omega^* e^{i\omega_l t})|1\rangle\langle 2|, \end{aligned} \tag{2.43}$$

where $\Omega = \mathbf{d}_{21} \cdot \mathbf{A}(x)/\hbar$ is the Rabi frequency [66] and $\tilde{\Omega} := \mathbf{d}_{21} \cdot \mathbf{A}^*(x)/\hbar$ is the counter-rotating frequency. With the transition frequency $\omega_{tr} = (E_2 - E_1)/\hbar$ the Hamiltonian of the free atom can be written as:

$$H_0 = \frac{\hbar}{2}\omega_{tr}(|2\rangle\langle 2| - |1\rangle\langle 1|). \tag{2.44}$$

The complete Hamiltonian can be now expressed by a 2x2 matrix:

$$H = \hbar \begin{pmatrix} \omega_{tr}/2 & -\Omega e^{-i\omega_l t} - \tilde{\Omega} e^{i\omega_l t} \\ -\tilde{\Omega}^* e^{-i\omega_l t} - \Omega^* e^{i\omega_l t} & -\omega_{tr}/2 \end{pmatrix}. \tag{2.45}$$

As a next step the time dependence is removed by transforming to the Schrödinger picture. This is done by a unitary transformation with the operator:

$$U = \begin{pmatrix} e^{-i\omega_l t/2} & 0 \\ 0 & e^{i\omega_l t/2} \end{pmatrix}. \tag{2.46}$$

The transformed state $|\bar{\psi}\rangle$ is related to $|\psi\rangle$ through $|\psi\rangle = U|\bar{\psi}\rangle$. The transformed Hamiltonian $\bar{H}$ results from inserting $U|\bar{\psi}\rangle$ into the Schrödinger equation and multiplying it with $U^\dagger$:

$$\begin{aligned} \bar{H} &= -i\hbar U^\dagger \dot{U} + U^\dagger H U \\ &= \hbar \begin{pmatrix} -(\omega_l - \omega_{tr})/2 & -\Omega - \tilde{\Omega} e^{i2\omega_l t} \\ -\Omega^* - \tilde{\Omega}^* e^{-i2\omega_l t} & (\omega_l - \omega_{tr})/2 \end{pmatrix}. \end{aligned} \tag{2.47}$$

The terms that oscillate at the frequency $2\omega_l$ can be neglected, because their contribution will average out at a timescale of the interaction. This approximation is called the *rotating wave approximation* in the literature. With $\Delta = \omega_l - \omega_{tr}$ the transformed Hamiltonian can be written as:

$$\bar{H} = -\hbar \begin{pmatrix} \Delta/2 & \Omega \\ \Omega^* & -\Delta/2 \end{pmatrix}. \tag{2.48}$$

To simplify the derivation we assume one rectangular pulse with the duration τ. The probability amplitudes after the interaction with the pulse can be then derived from the Schrödinger equation, which becomes in the Heisenberg representation:

$$|\bar{\psi_\tau}\rangle = e^{-i\bar{H}\tau/\hbar} |\bar{\psi_0}\rangle. \tag{2.49}$$

Writing the Hamiltonian $\bar{H}$ as a vector product $\hbar \boldsymbol{w} \cdot \boldsymbol{\sigma}$, where $\boldsymbol{w} = (Re(\Omega), -Im(\Omega), \Delta/2)$, $w = |\boldsymbol{w}| = \sqrt{|\Omega|^2 + (\Delta/2)^2}$, $\sigma_x = \begin{pmatrix} 0 & 1 \\ 1 & 0 \end{pmatrix}$,

$\sigma_y = \begin{pmatrix} 0 & -i \\ i & 0 \end{pmatrix}$ and $\sigma_z = \begin{pmatrix} 1 & 0 \\ 0 & -1 \end{pmatrix}$ allows the following notation of the operator in equation 2.49:

$$e^{-i\bar{H}\tau/\hbar} = e^{i\boldsymbol{w}\cdot\boldsymbol{\sigma}\tau} = \cos(w\tau)\mathbf{1} + i\frac{\boldsymbol{w}\cdot\boldsymbol{\sigma}}{w}\sin(w\tau), \tag{2.50}$$

where $\mathbf{1}$ is the unity matrix. With this notation the matrix that describes the interaction of a pulse with a two level atom can be written as:

$$M_\tau = \begin{pmatrix} \cos(w\tau) + i\frac{\Delta}{2w}\sin(w\tau) & i\frac{\Omega}{w}\sin(w\tau) \\ i\frac{\Omega^*}{w}\sin(w\tau) & \cos(w\tau) - i\frac{\Delta}{2w}\sin(w\tau) \end{pmatrix}. \tag{2.51}$$

The state of the atom after the interaction with the laser pulse can be obtained from:

$$|\bar{\psi_\tau}\rangle = M_\tau|\bar{\psi_0}\rangle. \tag{2.52}$$

If we assume the atom initially in its ground state ($|\bar{\psi_0}\rangle = \begin{pmatrix} 0 \\ 1 \end{pmatrix}$), the amplitudes of the two levels after interaction with the laser pulse become:

$$\begin{aligned} c_1(\tau) &= \langle 1|\psi_\tau\rangle = \cos(w\tau) - i\frac{\Delta}{2w}\sin(w\tau) \\ c_2(\tau) &= \langle 2|\psi_\tau\rangle = i\frac{\Omega}{w}\sin(w\tau). \end{aligned} \tag{2.53}$$

A low-power driving field allows an approximation $\Omega \ll \Delta$ and the Rabi-flopping frequency $w \approx \Delta/2$. The resulting excited state probability then becomes:

$$|c_2(\tau)|^2 = 4\left(\frac{\Omega}{\Delta}\right)^2 \sin^2\left(\frac{\tau\Delta}{2}\right). \tag{2.54}$$

In order to determine the state of the atom after interaction with a phase-locked pulse pair, the field-free evolution, and the interaction with the second pulse still need to be calculated. The matrix for the free evolution

can be obtained from the pulse matrix M_τ by setting the electric field and, thus Ω, to zero:

$$M_{free} = \begin{pmatrix} e^{i(T-\tau)\Delta/2} & 0 \\ 0 & e^{-i(T-\tau)\Delta/2} \end{pmatrix}. \tag{2.55}$$

The time T is here the delay between the pulses. As in the experiments, the second pulse is assumed to have the same envelope as the first pulse but differs in phase of the carrier. This phase is the carrier-envelope phase (CEP-)shift between the pulse that determines the spectral structure of a frequency comb laser or, like in this case, of two phase-locked pulses. To describe the interaction with it, this phase must be accounted for. This can be done using the transformation U, defined in 2.46 and a second unitary transformation $U_2^\dagger$:

$$U_2^\dagger = \begin{pmatrix} e^{i(\omega_l(t-T)+\phi)/2} & 0 \\ 0 & e^{-i(\omega_l(t-T)+\phi)/2} \end{pmatrix}. \tag{2.56}$$

The transformation becomes then:

$$U_2^\dagger U = \begin{pmatrix} e^{-i(\omega_l T-\phi)/2} & 0 \\ 0 & e^{i(\omega_l T-\phi)/2} \end{pmatrix}. \tag{2.57}$$

With these ingredients the final state of the two-level atom, after interaction with a coherent pulse pair can be determined from:

$$|\psi\rangle = M_\tau U_2^\dagger U M_{free} M_\tau |1\rangle \tag{2.58}$$

which yields for the excited state amplitude:

$$\begin{aligned} c_2(T+\tau) = i\frac{2\Omega}{w}\sin(w\tau)\Bigg[& \cos(w\tau)\cos\left(\frac{\omega_{tr}T+\phi+\tau\Delta}{2}\right) \\ & +\frac{i\Delta}{2w}\sin(w\tau)\sin\left(\frac{\omega_{tr}T+\phi+\tau\Delta}{2}\right)\Bigg] \end{aligned} \tag{2.59}$$

The prefactor of his expression is equal to twice the amplitude of the excited state after interaction with one pulse $c_2(\tau)$. This allows to write this amplitude as:

$$c_2(T+\tau) = i\frac{2c_2(\tau)}{w}\sin(w\tau)\Big[\cos\left(\frac{\omega_{tr}T+\phi}{2}\right)\Big(w\cos(w\tau)\cos\left(\frac{\tau\Delta}{2}\right) + \frac{\Delta}{2}\sin(w\tau)\sin\left(\frac{\tau\Delta}{2}\right)\Big) - \sin\left(\frac{\omega_{tr}T+\phi}{2}\right)\Big(w\cos(w\tau)\sin\left(\frac{\tau\Delta}{2}\right) - \frac{\Delta}{2}\sin(w\tau)\cos\left(\frac{\tau\Delta}{2}\right)\Big)\Big]. \tag{2.60}$$

With the same assumptions as for Eq. 2.54 Eq. 2.60 can be approximated with:

$$c_2(T+\tau) = 2c_2(\tau)\cos\left(\frac{\omega_{tr}T+\phi}{2}\right). \tag{2.61}$$

So the probability to find the atom in the excited state becomes:

$$|c_2(T+\tau)|^2 = 4|c_2(\tau)|^2\cos^2\left(\frac{\omega_{tr}T+\phi}{2}\right). \tag{2.62}$$

This simple expression can be used to gain some insight into the result of an interaction between an atom and a pair of short phase-coherent pulses. The approximations that led to this simple formula correspond to the situation present in the experiments reported in this thesis. The spectrum of the light interacting with helium was resonant with only one electronic transition in helium. The intensity was small enough to exclude nonlinear effects or Rabi-oscillations; the spectral power at the transition frequency ω_{tr} resulted in a population of the excited state that is estimated to be much smaller than 1‰.

From equation 2.62 follows that the excited state population exhibits an oscillating behavior if the delay $T = 1/f_{rep}$ between the pulses is scanned, very similar to the excitation method of spatially separated oscillatory fields as invented by Norman F. Ramsey in 1949 [67]. The period of the modulation is equal to $2\pi/\omega_{tr}$ and the position of the maxima is determined by this period, the delay and by the CEP-shift between the pulses. This means that an exact knowledge of the repetition time and CEP-shift of the pulse pair allows to determine the investigated transition frequency ω_{tr} modulo f_{rep}. The absolute value of ω_{tr} can also

be determined directly if ω_{tr} is known already better than a fraction** of f_{rep}. Alternatively, several scans at different repetition rates have to be made (see 2.3).

The frequency-domain representation

It is insightful to consider the excitation with a coherent pulse pair in the frequency domain as well. The spectrum of such a pulse pair is a cosine-modulated continuum with maxima that coincide with the teeth of frequency comb created by an infinite train of pulses, where consecutive pulses exhibit the same delay T and CEP-shift as the the coherent pulse pair under consideration. Figure 2.4 illustrates such a frequency comb formed by a pulse pair. The probability to find an atom in the excited state after interaction with a pulse sequence is proportional to the overlap between the spectrum of the pulse sequence and the atomic transition. The spectrum of the coherent pulse pair can be scanned across the transition either by changing the CEP-shift between the pulses or by changing the delay between them. Because the frequency of the excited helium transition is very high in comparison to the repetition rate of the laser, the mode number n in equation 2.41 is of the order of 50×10^6. Therefore already a small change of a few Hertz in $f_{rep} = 1/T$ moves the next adjacent mode into resonance while the distance between the modes is hardly changed.

Scanning the delay between the pulses results in a sinusoidal excitation spectrum, where each peak corresponds to a mode of the pulse pair that became resonant with the investigated transition frequency in the atom. The acquired spectrum does not provide the actual mode number n but a comb of frequencies separated by the repetition rate f_{rep} that could be resonant with f_{tr}. This ambiguity can be resolved by the approach that is discussed in section 2.3.

**With a very precise signal where the errorbar is negligible this fraction would be one half of the repetition rate. In reality it must be smaller in order to exclude the adjacent possibilities ($\pm f_{rep}$).

2.5 Theory of non-collinear optical parametric amplification

Optical parametric amplification is a special case of pulse propagation in a nonlinear medium which was introduced in sec. 2.1. We deal here in particular with a form of three-wave mixing which is commonly described by a set of wave equations coupled via the nonlinear susceptibility $\chi_e^{(2)}$ in a transparent birefringent crystal [68, 43, 44]. In an optical parametric amplifier a signal-wave E_s is amplified by a strong pump-wave E_p under the creation of an idler-wave E_i. The frequency of the idler-field satisfies energy conservation in the process by fulfilling the equation: $\omega_p = \omega_s + \omega_i$. Assuming the involved electromagnetic waves E_n can be expressed as: $E_n = A_n(x,t)\exp(i\mathbf{k}_n x - \omega_n t)$, the equations take the form [69]:

$$\frac{dA_p}{dx} = -i\chi_e^{(2)}\frac{\omega_p}{2n_p c}A_s A_i e^{i\Delta\mathbf{k}x} \tag{2.63a}$$

$$\frac{dA_s}{dx} = -i\chi_e^{(2)}\frac{\omega_s}{2n_s c}A_p A_i^* e^{-i\Delta\mathbf{k}x} \tag{2.63b}$$

$$\frac{dA_i}{dx} = -i\chi_e^{(2)}\frac{\omega_i}{2n_i c}A_p A_s^* e^{-i\Delta\mathbf{k}x}, \tag{2.63c}$$

with the wave-vector mismatch $\Delta\mathbf{k} = \mathbf{k}_p - \mathbf{k}_s - \mathbf{k}_i$. The indices p, s, and i refer to the pump-, signal- and idler-wave respectively. These equations receive their simple form partly due to the slowly varying envelope approximation and partly as a result of neglecting dispersion-related effects on the propagation of the three pulses. Analytical solutions exist for some cases, otherwise a numerical solution to these equations can be found. Still, from the set of equations 2.63 some insight into optical parametric amplification can be gained. The efficiency of the energy-transfer between the interacting wave packets depends mainly on their intensities and on the wave-vector mismatch $\Delta\mathbf{k}$ that should ideally fulfill the phase-matching condition:

$$\mathbf{k}_p = \mathbf{k}_s + \mathbf{k}_i. \tag{2.64}$$

Using the wave-vector $\mathbf{k}$ instead of the previous notation as wavenumber k indicates that the phase-matching condition can be satisfied in a

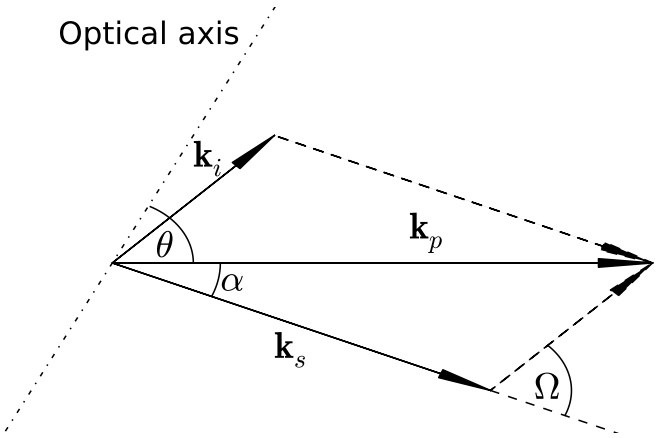

Figure 2.5: Geometry of the waves in optical parametric amplification aligned for perfect phase-matching

non-collinear alignment of the pump- with respect to the signal-beam. Fig. 2.5 illustrates the geometry of perfect phase-matching in such a non-collinear case. When this condition is fulfilled, a fixed phase relation is maintained between the signal wave and the nonlinear polarization, thus extracting the energy most efficiently from the incident waves [43]. The field emitted by the individual dipoles is in phase for $\Delta k = 0$, so that contributions from all parts of the beam in the nonlinear crystal again add coherently in the forward direction, resulting in a maximal gain. If $\Delta\mathbf{k} \neq 0$ the amplification in the NOPCPA is less efficient. The phase-matching condition plays a prominent role in amplification of short pulses with their extremely broad bandwidths. In order to amplify the a broad bandwidth, $\Delta\mathbf{k}$ must be minimized over the spectrum of the signal pulse. In practice this can be achieved by aligning the angles (α and θ in Fig. 2.5) between the appropriately polarized beams and the optical axis of the birefringent crystal that is used (e.g. BBO = $\beta-\mathrm{BaB_2O_4}$), so that (near) phase matching can be achieved for spectra spanning hundreds of nanometers in the visible to near-infrared range. An excellent review of broadband NOPCPA can be found in the thesis of S. Witte [70] and in [71].

As the bandwidth of the pulses used in the experiments presented in this thesis was only 6 nm centered around 773.5 nm, sufficient phase-matching could easily be achieved by keeping the non-collinear angle α within a range of a few tenths of a degree around 2.5° and tuning the phase-matching angle θ (by rotating the BBO-crystal placed in the intersection of the beams), until the gain was maximized. In fact, α and θ were set to support amplification of ≈ 30 nm around the central wavelength. This was done to obtain a flat spectral phase-mismatch within the desired bandwidth and thus, as will be shown in the following, reduce amplification related shifts of the carrier-envelope phase of the pulses.

Ross shows in his analysis [72] how the phase of the pulses evolves in a NOPCPA. A set of equations for the phases of the signal-, idler- and the pump-pulse is obtained by writing out the imaginary part of the coupled wave equations 2.63. The following set of equations is obtained:

$$\frac{d\phi_s}{dx} = -\chi^{(2)} \frac{\omega_s}{2n_s c} \frac{\rho_i \rho_p}{\rho_s} \cos\theta \tag{2.65a}$$

$$\frac{d\phi_i}{dx} = -\chi^{(2)} \frac{\omega_i}{2n_i c} \frac{\rho_s \rho_p}{\rho_i} \cos\theta \tag{2.65b}$$

$$\frac{d\phi_p}{dx} = -\chi^{(2)} \frac{\omega_p}{2n_p c} \frac{\rho_s \rho_i}{\rho_p} \cos\theta, \tag{2.65c}$$

where $\theta = \phi_p - \phi_s - \phi_i$ is the NOPCPA phase and $\rho_m = A_m e^{\phi_m}$. The equations can be integrated and combined to find an expression for $\cos\theta$. By assuming that the idler intensity is initially zero[††], and using the *Manley-Rowe relations*, which express energy conservation in the parametric process, we obtain:

$$\frac{d\phi_s}{dx} = -\frac{\Delta k}{2}\left(\frac{f}{f+\gamma^2}\right) \tag{2.66a}$$

$$\frac{d\phi_i}{dx} = -\frac{\Delta k}{2} \tag{2.66b}$$

[††]In the non-collinear geometry the angle at which the idler-beam leaves the crystal is bigger than α for a signal wavelength smaller than two times the pump wavelength. However, in a multi-stage OPA that operates with small non-collinear angles an idler wave can enter subsequent amplification stages, which can cause the break down of this approximation.

$$\frac{d\phi_p}{dx} = \frac{\Delta k}{2}\frac{f}{1-f}. \tag{2.66c}$$

With $\gamma^2 = \frac{\omega_p I_s(0)}{\omega_s I_p(0)}$ and a fractional pump-depletion term f:

$$f = 1 - \frac{I_p(x)}{I_p(0)} \tag{2.67}$$

integration of equations 2.66 leads to the following expressions for the evolution of the phases:

$$\phi_s = \phi_s(0) - \frac{\Delta k}{2}\int_0^x \frac{f}{f+\gamma^2}dx' \tag{2.68a}$$

$$\phi_i = \phi_p(0) - \phi_s(0) - \frac{\pi}{2} - \frac{\Delta k x}{2} \tag{2.68b}$$

$$\phi_p = \phi_p(0) - \frac{\Delta k}{2}\int_0^x \frac{f}{1-f}dx'. \tag{2.68c}$$

In these equations $\phi_s(0)$, $\phi_p(0)$ and $\phi_i(0)$ are the initial phases at $x = 0$ for respectively signal, pump and idler beam. It has been shown in section 2.2 that the shift in the carrier-envelope-phase offset equals $\Delta\phi = \Phi^{(2)}_{CEO} - \Phi^{(1)}_{CEO}$, where (n) denotes the pulse, determines the spectrum of a pulse-pair. (Fig. 2.4 illustrates such a wave packet and its spectrum.) With the focus on the intended Ramsey-type frequency measurement, a major part of the work presented in this thesis deals with phase shifts induced by amplification in the NOPCPA. This makes equation 2.68a, which describes the amplification-induced phase-evolution of a signal wave, of major importance.

Fortunately, the phase of the signal wave does not depend on the phase properties of the pump and, as mentioned before, the influence of the idler in this approximation is excluded by the non-collinear geometry. However, there is a residual contribution from the pump energy, represented by the integral in equation 2.68a. This contribution is a product of the alignment-dependent phase mismatch Δk (and also due to local wavefront deviations, especially in the pump beam), multiplied with an integral over a "pump-depletion" term. The size of the pump depletion also depends on the phase mismatch and additionally on the starting intensities of the pump and the signal wave. The influence on signal intensity and phase of a phase-mismatch in a NOPCPA was extensively

investigated in numerical simulations [73]. Because the phase shift in the infrared is multiplied by the harmonic order, it is paramount to keep it small. A change of 200 mrad results in a phase shift of half an XUV-cycle at the 15^{th} harmonic. Chapter 4 reports on the results of these simulations and experimental investigations for a NOPCPA in broad-band operation. The analysis reveals a high sensitivity of the amplifier-induced phase-shifts on alignment and pump intensity. This insight was used in the design of the amplifier-system for precision Ramsey spectroscopy, which is introduced in chapter 3. In the following section the theoretical background of high harmonic generation is given, with a focus at the phase properties of the generated radiation.

2.6 High harmonic generation

One-photon excitation of helium from the ground state, as done in the experiments described in this thesis, requires radiation in the XUV region at wavelengths around 50 nm. This radiation is conveniently produced by means of high harmonic generation (HHG). This nonlinear effect takes place in the non-perturbative regime at intensities higher then 10^{12} W/cm^2. The theory of this phenomenon is introduced in this section.

That the perturbative approach assumed for equation 2.37 breaks down above 10^{13}W/cm^2 was observed by McPherson et al. [74] and Ferray et al. [75] in noble gases as a deviation of the exponential fall-off with harmonic order for HHG in noble gases. They observed a spectrum of up-converted radiation, which decayed exponentially up to the 5^{th} harmonic order, followed by a plateau of odd-order harmonics of the fundamental field. This plateau extended up to 17^{th} [74] and the 33^{rd} [75] harmonic order respectively, and a sharp *cutoff* thereafter was observed.

The observed spectrum could not be explained with the perturbative approach of the previous section. It took indeed several years before the first, so called *two- or three-step model* (also known as the *simple-man's model*) for this behavior was put forward by Corkum [76] and Kulander [77] in 1993. This model was validated by a more accurate quantum-mechanical description of the HHG-process derived by Lewenstein et al. [78, 79, 80] shortly after, providing a deeper insight into the HHG-process. A discussion of these approaches will be followed by a dis-

cussion of the macroscopic response of a noble gas medium to a laser pulse focused to an intensity approaching $10^{14}\mathrm{W/cm^2}$.

The single atom response

The three step model [76] is a semi-classical treatment of multi-photon ionization. It takes into account that there is a significant probability for the electron to return to the vicinity of the ion with a very high kinetic energy within the first few laser periods after ionization. In the first step (see Fig. 2.6(a)), the electron tunnels out of the Coulomb potential of the atom, which is tilted by the electric field component of a powerful laser pulse.

The second step (Fig. 2.6(b,c)), considers classically the kinetic energy, accumulated by the electron in the oscillating field of the laser pulse. In the third step (Fig. 2.6(d)) the electron eventually collides with the parent ion, releasing the kinetic energy together with the recombination energy [‡‡] in the form of odd-order harmonic radiation. Based on this model the maximum energy of the electrons, and therefore of the emitted photons, depends on the ionization potential of the atom and the maximum energy an electron can acquire in an oscillating field. The latter is called the ponderomotive energy, introduced by Keldysh [81]:

$$U_P = \frac{E^2}{4\omega^2}, \tag{2.69}$$

where E is the amplitude of the electric field oscillating at the angular frequency ω. The maximum photon energy is then equal to $I_P + 3.2U_P$ according to the recollision model.

Despite the neglect of the uncertainty principle, Corkum could calculate the spectral shape of the harmonic radiation in a qualitatively good agreement with experimental findings. However, this model systematically overestimates the energy of the cutoff, which is found to be significantly lower (at $\approx I_P + 2U_P$) in experimental spectra. The actual position of the cut-off region could be calculated by considering the velocity distribution of the tunneled-out electrons [78] and the influence of phase-matching effects on the emitted radiation [82]. The kinetic energy of returning electrons is displayed in Fig. 2.7 as a function of the time τ

[‡‡] the binding energy of the ground-state electron

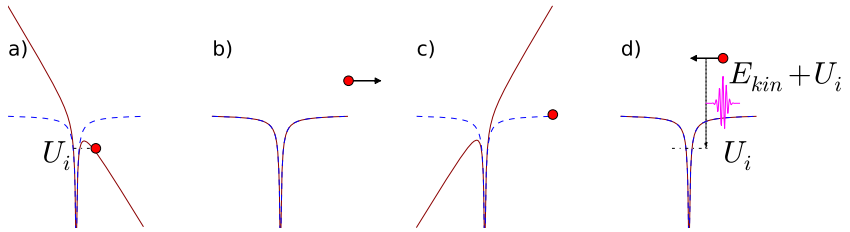

Figure 2.6: Three-step model of HHG. The coulomb potential (blue dashed lines) of an atom is strongly deformed by the electric field of an incident pulse, resulting in an oscillating potential represented by the solid red lines. (a) An electron (red dot) tunnels out of the atom due to the lowering of the coulomb barrier in the electric field of an incident laser pulse. (b),(c) The released electron is accelerated in the oscillating laser field. (d) Eventually the kinetic energy accumulated by the electron is re-emitted in form of harmonic radiation if the electron re-captured by the parent ion. E_{kin} denotes the accumulated kinetic energy of the electron, U_i is the ionization potential of the ground-state atom.

spent in the continuum after ionisation. A complete theory for a linearly polarized driving field was developed by Lewenstein 1994 [79, 80], and was generalized to include elliptical polarization by Antoine et al. [83].

The Ramsey-type frequency metrology described in this thesis hinges on the exact knowledge about the relative phase of the participating fields. Because these are produced in a HHG-process, the phase of the emitted radiation receives a central significance here. In the following description the phase of the emitted harmonics is studied, in view of the conditions typically used in the experiments. The theoretical basis for it can be found in [79, 80, 84] and the references therein. This model is valid in the tunneling regime, where $U_P \geqslant I_P > \hbar\omega$. Further, it assumes negligible contribution from all the bound states except the ground state $|0\rangle$ and neglects depletion of this ground state. A fourth assumption is that the electron can be considered a freely moving particle in the continuum, which means that the parent ion potential is omitted in the calculation of the electron trajectory.

The harmonic radiation finds its origin in the atomic dipole moment, induced by the fundamental radiation. With $|\mathbf{v}\rangle$ denoting the electrons, outgoing with velocity $\mathbf{v}$, the dipole moment proportional to $\mathbf{x}(t) = \langle\psi(t)|\mathbf{x}|\psi(t)\rangle$, and can be expressed (omitting the complex conjugate) as:

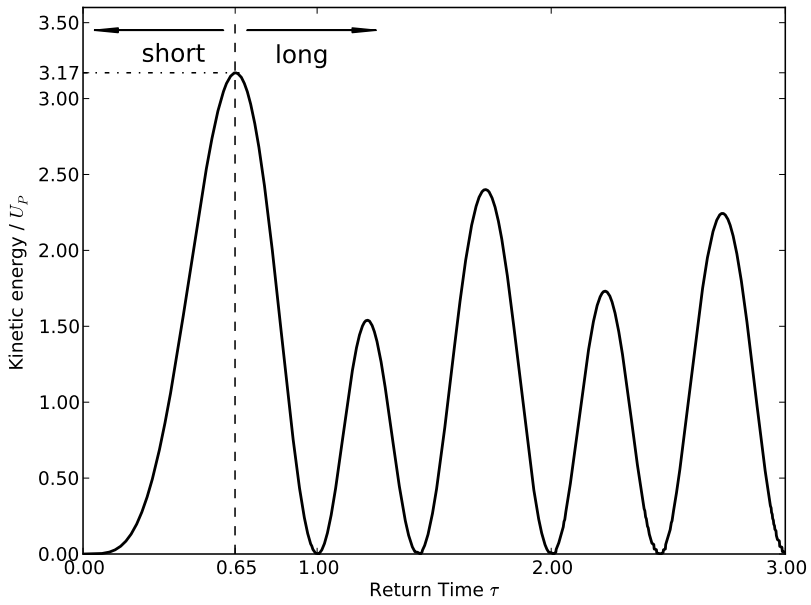

Figure 2.7: Kinetic energy of the returning electron, expressed in units of the ponderomotive potential U_P, plotted against the return time τ, which is counted in cycles of the driving field. The dashed vertical line emphasizes the degeneracy between the short and long electron trajectories in the cutoff region of the emitted radiation

$$\mathbf{x}(t) = i \int_0^t dt' \int d^3\mathbf{p} \quad \mathbf{d}^*(\mathbf{p} - \mathbf{A}(t)) e^{-iS(\mathbf{p},t,t')} \mathbf{E}(t') \cdot \mathbf{d}(\mathbf{p} - \mathbf{A}(t')), \tag{2.70}$$

where $\mathbf{A}(t)$ denotes the vector potential of the incident radiation, $\mathbf{d} = \langle \mathbf{v}|\mathbf{x}|0\rangle$ is the field-free dipole transition matrix element and the integration variable $\mathbf{p}$ is the canonical momentum $\mathbf{p} = \mathbf{v} + \mathbf{A}(t)$ of the electron. The term in the exponential is the *quasi-classical action*:

$$S(\mathbf{p}, t, t') = \int_{t'}^{t} dt'' \Big(\frac{(\mathbf{p} - \mathbf{A}(t''))^2}{2} + I_P \Big). \tag{2.71}$$

Equation 2.70 is interpreted as a sum of probability amplitudes corresponding to the three steps of the process. The last term $\mathbf{E}(t') \cdot \mathbf{d}(\mathbf{p} -$

$\mathbf{A}(t')$) is the probability amplitude of the electron to appear in the continuum with velocity $\mathbf{v}$ at time t'. The phase factor in the middle describes the motion of the electron in the driving laser field. Although the field of the parent ion does not appear here, some influence of the Coulomb potential is included with the binding energy I_P. The probability amplitude of recombination is given by $\mathbf{d}^*(\mathbf{p} - \mathbf{A}(t))$.

The quasi-classical action 2.71 varies for return-times $\tau = t - t'$ on the order of a period of the driving field, much faster than the two other contributions in the integral 2.70. Quantum diffusion (i.e. the spread of the electronic wave packet) effects reduce these variations, scaling as $\propto 1/\tau$. The biggest share comes therefore from stationary points in $S(\mathbf{p}, t, t')$. It turns out that these correspond to the momenta $\mathbf{p}$, for which the electron returns to the vicinity of the ion. Neglecting the magnetic field component and assuming linear polarization of the driving field causes only electrons with negligible starting velocities to reach the parent ion and emit the harmonic radiation. It is remarkable, how the quantum theory justifies here the semi-classical model [76, 77], which assumed electrons tunneling out the atom with initially zero velocity.

The spectrum of the emitted radiation is obtained from the Fourier transform of $\mathbf{x}(t)$. With the help of expression 2.70 the Fourier components of the spectrum can be written as:

$$\mathbf{x}_M = \int_0^{2\pi} dt \quad \mathbf{x}(t) e^{iMt}, \tag{2.72}$$

where M is the angular frequency of the considered Fourier component. The calculation of this integral is difficult and can be done either numerically or approximated analytically with a saddle-point method applied to all five integration variables ($\mathbf{p}(x, y, z)$,t and τ) of Eq. 2.72, in which $\mathbf{x}(t)$ is replaced by expression 2.70. The calculated spectrum fulfills the energy conservation law, yielding stable results in noble gases only for energies of the returning electron that are equal to odd-order harmonics of the driving field. The even-order harmonics are excluded here by the symmetry of the problem, but they can be generated using two color driving fields [85].

The result depends only weakly on the actual form of $\mathbf{d}(\mathbf{p})$. This observation allows to approximate it by assuming it constant. Equation 2.72 takes in this case the following form:

$$\mathbf{x}_M \propto \int_0^{2\pi} dt \int_0^{\infty} d\tau \int d^3\mathbf{p} \quad e^{-iS(\mathbf{p},t,\tau)+iMt}. \tag{2.73}$$

The previously mentioned saddle-point method comprises finding the stationary points of the quasi-classical action. This is done by setting the partial derivatives of $S(\mathbf{p},t,\tau)-Mt$ with respect to $\mathbf{p}$, t and τ equal to zero, which yields:

$$\tau\mathbf{p} - \int_{t-\tau} tdt'\mathbf{A}(t') = 0 \tag{2.74a}$$

$$\frac{(\mathbf{p}-\mathbf{A}(t))^2}{2} - \frac{(\mathbf{p}-\mathbf{A}(t-\tau))^2}{2} = M \tag{2.74b}$$

$$\frac{(\mathbf{p}-\mathbf{A}(t-\tau))^2}{2} + I_P = 0. \tag{2.74c}$$

Equation 2.74a expresses that electron trajectories relevant for the process come in the vicinity of the parent ion after time τ. Energy conservation is expressed in equation. 2.74b, while the last saddle point equation: 2.74c describes tunneling that occurs at the time $t-\tau$. Note that this equation has only complex solutions for $I_P > 0$. Equations 2.74 have many, typically complex solutions, and the task is to find and identify saddle-points $(\mathbf{p}_s, t_s, \tau_s)$, which contribute to the high-harmonic emission. The solution can be understood as a weighted sum of the values of the integrand at these points, and can be written as:

$$x_M = \sum_s a_{Ms} e^{-iS(\mathbf{p}_s,t_s,\tau_s)+iMt_s}. \tag{2.75}$$

The weighting factors a_{Ms} contain the dipole transition amplitudes and the sizes of the corresponding saddle points.

It is worthwhile to first consider the special case, where the ionization potential I_P is zero. For energies above the cutoff, where $M > 3.17U_P$, there are only complex solutions. One of those $(\mathbf{p}_2, t_2, \tau_2)$, with a real part of the complex return time $Re(\tau_2) \approx 4.08$, becomes real at the cutoff and bifurcates into two real solutions in the plateau region. The first $(\mathbf{p}_1, t_1, \tau_1)$ corresponds to a *short trajectory* of the electron with return times τ_1 close to 0. The second solution $(\mathbf{p}_1, t_1, \tau_1)$, the *long trajectory*,

corresponds to electrons with return times approaching 2π. If viewed classically, the short trajectory corresponds to the electrons, that recombine with the parent ion when returning to its vicinity for the first time. The long trajectory corresponds to electrons, which recombine upon the second arrival at the ion. These trajectories can be found in Fig. 2.7 as the rising and falling flanks of the first and highest peak. Following this interpretation, further thresholds for the harmonic order ($M = 2.4U_P$, $M = 2.2U_P$, see Fig. 2.7) are found in this diagram, at which more real solutions appear for longer return times τ. They all correspond to electron trajectories, which pass the nucleus multiple times before a recombination occurs. The contribution to the emitted field from these electrons can be neglected due to quantum diffusion effects.

The situation becomes more complicated for real atoms with a finite ionization potential, because there are no real solutions to equation 2.74. However, the two solutions $(\mathbf{p}_1, t_1, \tau_1)$ and $(\mathbf{p}_2, t_2, \tau_2)$ can be still identified and it turns out that a slightly bigger contribution comes from the long trajectory electrons, which tunnel out of the atom close to the maximum of the driving field, when the potential barrier is narrowest (and lowest). Electrons with a short recombination time, tend to have tunnelled out when the field is much smaller. Apparently the long trajectory finds a better compromise between the damping related to tunneling and the effect of travel-time dependent quantum diffusion.

Solutions 1 and 2 do not merge for $M > 3.17U_P$, like in the case where the ionization potential has been neglected. Instead the imaginary part of solution 1 becomes positive, making it unphysical.

As can be seen in equation 2.75, the phase of the emitted radiation is determined by the quasi-classical action, which mainly depends on U_P. The term e^{iMt_s} gives a constant shift for each trajectory and harmonic, as the ionization time t_s (first step one in the three-step model) is defined with respect to the phase of the driving IR-Field. From that contribution it can be estimated as $-4.08U_P$ at the cutoff and $-6.28U_P$ for higher intensities, and does not depend on the considered high-harmonic order.

Lewenstein et al. have calculated the dependence of the strength and phase of the single atom dipole response in HHG [80] on the intensity of the driving field. The results of their calculation for the two most relevant saddle points (which are the long and the short trajectory) is shown for the 45^{th} harmonic in neon in Figure 1a and 1b in [80]. This

comparison reveals the magnitudes of contributions from these trajectories to the single-atom response. The most relevant long trajectory shows a smooth laser-power dependence of the dipole intensity in the plateau region, which rises by an order of magnitude between the cutoff intensity at $2 \times 10^{14}\mathrm{W/cm}^2$ and $5 \times 10^{14}\mathrm{W/cm}^2$. The dipole intensity drops very quickly to zero before the cutoff. When the short trajectory is included into the analysis, the dipole intensity in the plateau region is dominated by quantum interference effects. This leads to a strong modulation of the dipole intensity, which is already in excellent agreement with the exact solution that incorporates all relevant saddle points. A similar behavior is shown by the dipole phase dependence on the intensity. However, the modulation of the phase dependence from the interference between the two trajectories is much less pronounced than the previously mentioned modulation of the dipole intensity. The actual dependence of the phase on the ponderomotive potential is smaller than the estimation based on the ponderomotive energy, due to contributions from tunneling and recombination to the action. It turns out to be $\propto -3.2U_P$ below, and $\propto -5.8U_P$ above the cutoff intensity. A closer look reveals that it is in fact a slowly varying function of U_P, that starts at -3.3 for small U_P and slightly increases, as U_P approaches the threshold to the plateau. At the threshold the coefficient quickly changes to -5.7 and decreases slowly towards the asymptotic limit of -2π for an infinite ponderomotive potential. The dominant contribution from the long trajectory predicts the single atom response quite well. However, the contribution from the short trajectory (emitted predominantly close on axis) becomes crucial in the calculation of the macroscopic response. The exact solution, that takes into account all physical saddle points, deviates very slightly in phase and intensity from the approximation based on the first two trajectories. The two trajectories account for most of the quantum interference effects in the intensity dependence of the dipole phase and intensity. Lewenstein points out that the described behavior varies very little for different high-order harmonics and media. The considered 45^{th} harmonic in neon can therefore be understood as a representative for this process.

In a realistic HHG experiment the radiation is generated not by a single atom, but in a focus located close to a small cloud of atoms (a gas jet or cell). The intensity distribution in a focus and the calculated phase dependence of a single atom emission on intensity make apparent

that it is necessary to integrate the dipole response over the whole focal volume to calculate the actual high harmonic emission from a noble gas medium. The following subsection elaborates on this approach.

Macroscopic response

The single-atom response to an intense laser field, that was discussed before, shows considerable dependence of the phase of the emitted radiation on the intensity of the driving field. As has been shown in [80] the dependence is steep, but rather smooth in the cut-off region and becomes steeper in the plateau, where it is modulated with random looking oscillations. That oscillatory behavior results from different phases of trajectories which contribute to the emission of the individual harmonics in the plateau region. Note, that although the actual shape of this oscillation varies between different media and harmonics, the underlying general behavior changes only slightly for different cases, and can be considered universal in HHG.

The strong dependence of the dipole phase on the intensity of the driving field results in a spatial and temporal variation in the phase of the emitted harmonic. Additionally a Gouy phase shift [86], ϕ_G that occurs in the propagation of a beam through a focus, must be taken into account. For the q^{th} harmonic, a Gaussian driving field and a Rayleigh length of the focus equal to z_r it can be written as:

$$\phi_G = -q \arctan \frac{z}{z_r}, \tag{2.76}$$

where z is the distance from the focus waist along the beam direction. The radial distribution of the intensity is Gaussian, while the longitudinal profile obeys:

$$I(z) = I_0/(1 + \frac{z^2}{z_r^2}). \tag{2.77}$$

The generation of harmonics is optimal, if the produced radiation remains in phase with the driving field, while both propagate through the medium. It is therefore interesting to take a look at the sum of both phase effects. The phase variation goes in the same direction in the

trailing part of the focus. However, in the leading part of the focus the intensity-induced phase shift and the Gouy phase have opposite signs and compensate, especially for cutoff harmonics, for which the intensity dependence of the phase is smaller. This effect is commonly used in HHG setups, by focusing the driving field in front of the medium* to obtain best phase-matching conditions on the beam axis. The spatial and spectral shape of the harmonics there is smooth and Gaussian-like.

A focus centered in the harmonic medium, exhibits poor phase matching conditions and the conversion efficiency is reduced there. A second maximum in efficiency appears for a focus placed shortly after the medium. In that case phase matching remains impossible on axis, but occurs off axis instead. However, the high conversion efficiency is corrupted by distorted spectral and temporal profiles of this radiation. Interestingly, these two contributions result in two spatially separated modes in the far field, emitted in forward direction. Harmonics generated in the front part of the focus are emitted in a Gaussian mode in the center of the driving beam. The mode from the rear part of the focus appears as a donut-shaped cone around the central mode.

An analysis of the contributions from the saddle-point analysis reveals that the donut mode originates from the long trajectory, while the harmonics emitted in the center correspond to a combination of short quantum path (typically dominant) and long quantum path contributions. The crucial role of the phase in the experiment presented in this thesis demands to pay special attention to the intensity dependence of the phase of the emitted radiation. The analysis reveals that the intensity dependence of the phase is smallest for the cutoff harmonics and that it is smaller for the short trajectory emission than for radiation originating from the long trajectory electrons. An experimental investigation by Pirri et al. [87] confirms this conclusion. The coefficient that relates the phase of the high order harmonics to the intensity of the driving field was found to be 5 to $10 \times 10^{-14}\mathrm{cm}^2/\mathrm{W}$ for harmonics $13-19$, generated in argon at 800 nm.

Note that the treatment given above represents still an approximation of the physics that takes place in electromagnetic fields in the tun-

*The effective length of the interaction zone, in which the harmonic radiation is generated is assumed is a few times smaller than the Rayleigh length of the focus (tight focusing).

neling regime. A more precise description reveals e.g. parametric amplification that can occur in such an intense focus [88]. However, for the experiments presented in this thesis the approximate model of HHG is sufficient.

Introduction

This chapter gives an overview of the implemented experimental techniques, which include non-collinear optical parametric chirped pulse amplification (NOPCPA) of a near-infrared pulse pair, the measurement principle of the amplifier-related differential phase shift between these pulses, their harmonic upconversion to a phase-coherent XUV-pulse pair, and the vacuum setup used for the measurement of transitions in helium with the created XUV-frequency comb.

3.1 The frequency comb laser

The near-infrared FCL, which is the front-end of the setup described in this thesis, is a home-built linear Kerr-lens modelocked Ti:Sapphire oscillator. A scheme of this oscillator is depicted in Fig. 3.1. It is pumped with 5 W at 532 nm from a Verdi-V10 (Coherent) and served as a source

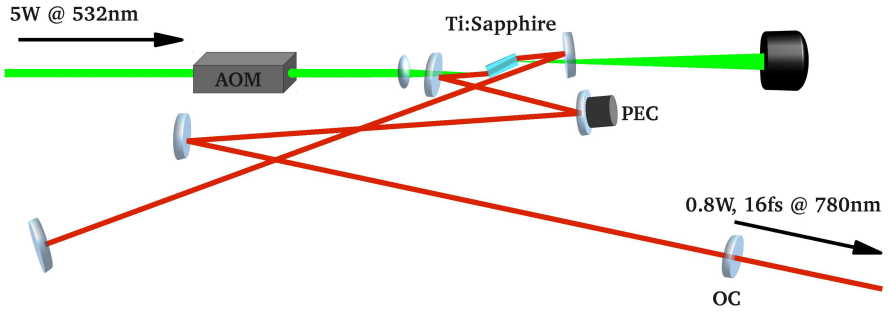

Figure 3.1: A schematic of the used frequency comb laser. AOM = acousto-optic modulator, PEC = piezo-electric crystal, OC = output coupler.

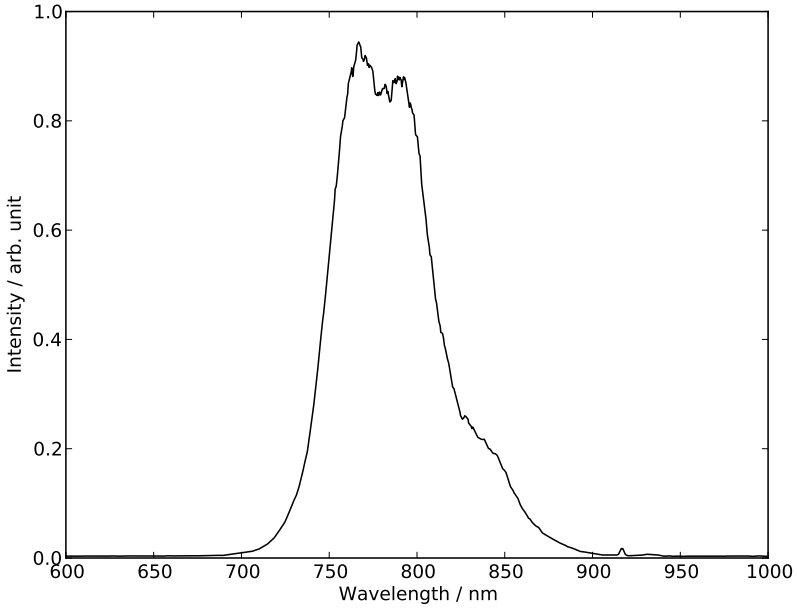

Figure 3.2: The spectrum of the used oscillator.

for the first TW-class NOPCPA (see [89]). This oscillator was adapted to the experiments presented here by using a different set of *chirped mirrors** which support a 60 nm bandwidth in the oscillator (see Fig. 3.1) while maintaining an output of approximately 900 mW.

The frequency comb repetition rate f_{rep} can be coarsely adjusted between 100 and 185 MHz by moving the end mirror using a translation stage. One of the flat cavity mirrors is mounted on a piezo for electronic feedback. This is used to lock f_{rep} to either a frequency equal to the repetition rate, or to a multiple harmonic using a combination of a mixer and a PID controller. The frequency equal to the repetition rate is produced by an Agilent 33250A arbitrary waveform generator, while a Agilent PSG-L E8241A generator provides a frequency close to 10 GHz for harmonic locking (which improves the quality of the locking). A GPS-disciplined Rb-clock (Stanford research PRS 10) serves as a time

*Besides 'holey fibers', the range of photonic materials developed in the recent decades also includes 'chirped mirrors'. The latter employ multi-layered dielectric coatings, with a varying layer-thickness to impose artificial frequency chirps on the reflected wave packets.

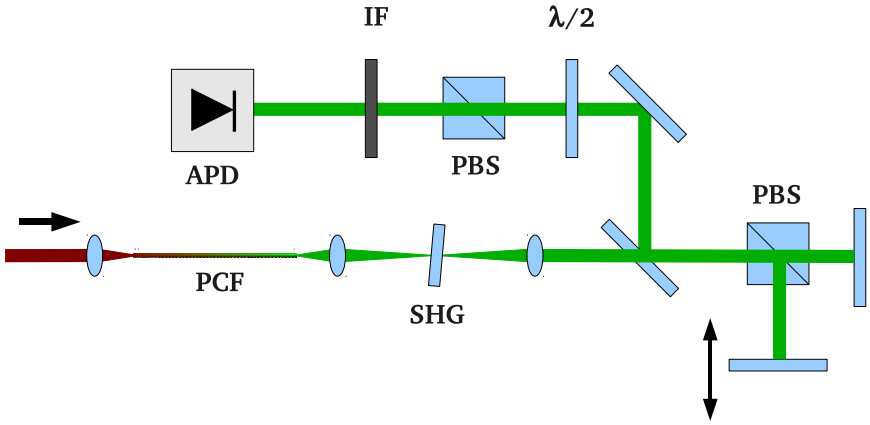

Figure 3.3: Implementation of the $f-2f$ detection of f_0 with a Michelson interferometer. PCF: photonic crystal fiber, SHG: second harmonic generation, PBS: polarizing beam splitter, IF: interference filter, APD: avalanche photo diode.

standard for both frequency generators to which the FCL is locked. The frequency accuracy of this standard reaches 10^{-11} after a few seconds, and 10^{-12} after a few hours of operation. The actual repetition frequency of the FCL is measured with a 1 GHz bandwidth photo-diode DET-210 (Thorlabs) or with a fast (10 GHz) photo-diode ET-4000 (EOT) for the fundamental and the high-order frequency lock respectively. A set of resistive heating elements is used to keep the temperature of the underlying optical board constant and the repetition rate lock within the range of the piezo.

The offset frequency f_0 is measured with the $f-2f$-scheme (Fig. 2.2), in a Michelson-type interferometer as depicted in Figure 3.3. The 60 nm wide pulses, centered around 780 nm are broadened in a photonic fiber to a more than octave-wide spectrum. The infrared wing at 1000 nm is frequency doubled in a thin BBO-crystal. This brings the green wing of the fundamental (original spectrum) in overlap with the frequency-doubled infrared part. However, the frequencies of the doubled frequency comb (f_m) are shifted by the offset-frequency with respect to the original (f_n) according to:

$$f_m = 2f_0 + mf_{rep}. \tag{3.1}$$

Comparing equation 3.1 with 2.41 shows that the lowest beat frequency between the fundamental and the frequency-doubled comb equals f_0.

Strong nonlinear interaction in a photonic fiber, such as self-phase modulation and four-wave mixing, is used to create pulses from the oscillator with an octave wide spectrum for $f-2f$ interferometry. The microstructured geometry of the fiber is designed to keep the group velocity dispersion (GVD) of the pulse small, thus to keep the power of the light pulse and therefore the nonlinearity of the medium high for an extended duration. However, the dispersion compensation is not perfect and the pulse eventually breaks up into several solitons. As a result the infrared and the green part of the spectrum leave the fiber temporally separated. The temporal overlap between the doubled light and the fundamental is established again in a Michelson interferometer positioned after the doubling crystal. The spatially and temporally overlapped pulses are sent through an interference filter and onto an avalanche photo-diode, where the beat-signal f_0 (plus several harmonics and products of mixing with the repetition rate) is detected. The $\lambda/2$-waveplate (together with the polarizing beam splitter) in Fig. 3.3 enables to optimize of the ratio between the two green components for an optimal detection of f_0.

Fast feedback of f_0 of the comb laser is obtained with an acousto-optical modulator (AOM, model AFM804A1 with the driver ME-802N, both from IntraAction), by modulating the intensity of the pump-beam in the Ti:Sapphire crystal. Coarse (slow) adjustment of f_0 is accomplished by changing the amount of material in the cavity with two thin fused silica glass wedges. The modulation of the pump intensity changes the dispersion properties of the lasing crystal, affecting the phase and group velocity in a different way. In particular self-phase modulation and self-steepening effects are mainly responsible for pump-intensity related CEP-shifts [90]. The small change in the round-trip time of the pulse due to these effects is compensated by the repetition-rate control-loop.

The actual sign of f_0 is not detectable in the $f-2f$ interferometer. Instead it can be deduced in a spectroscopic experiment from an apparent frequency shift in the phase of the detected Ramsey fringes. Changing the locking frequency for f_0 in the helium spectroscopy reported in this

thesis by 1 MHz shifted the signal (measured at the 15^{th} harmonic) by 30 MHz, if the wrong sign was assumed for f_0 in the analysis.

3.2 Non-collinear optical double pulse parametric amplification

Radiation in the XUV spectral range is generated by focusing strong infrared pulses into a dilute noble gas, where high-order harmonics of the fundamental are generated. In order to obtain the necessary pulse energies, non-collinear optical chirped pulse amplification (NOPCPA) has been employed. Amplification in a NOPCPA has several advantages over the conventional approach of using an optically pumped crystal (such as Ti:sapphire). The instantaneous nature of NOPCPA, where no energy is being dissipated in the crystal, allows to directly transfer the energy from a strong pump-pulse into a weaker seed without significantly changing the optical properties of the medium. The main advantage for this experiment is that two pulses which are separated in time by only a few nanoseconds can be amplified under the same conditions. Further, the high gain per crystal length that can be achieved in a NOPCPA enables to boost the pulse energy by several orders of magnitude in only few mm of material. These two properties ensure that differential phase shifts between the pulses, which can occur in the amplifier and potentially have the ability to destroy the calibration of the spectrum, remain small and therefore manageable. In a Ti:sapphire based multi-pass amplification scheme, as typically employed to boost pulses from Ti:sapphire oscillators to the millijoule level, the second pulse would travel through a gain medium that was partly depleted by the precursor. Hence, the pulses would experience different optical properties in the amplifier material. Additionally, as the gain per length is much lower in such schemes, the pulses would need to travel for a longer distance in the bulk material (i.e. in a multi-pass setup) in order to reach comparable energy levels. One can therefore expect complicated differential phase shifts between the pulses from such an approach. Gain depletion also makes it more difficult to obtain two equal intensity pulses required for upconversion of a frequency comb. An NOPCPA scheme does not have

these drawbacks, and is therefore the best choice for XUV-comb Ramsey spectroscopy of the ground state of helium.

The employed NOPCPA amplifier is based on one that was initially used to demonstrate amplification of few-cycle infrared laser pulses to the TW level [91, 89, 70]. For the purpose of this thesis a short introduction to parametric amplification with a focus on phase-effects on the amplified light will be given in this section, including a description of the modifications of this NOPCPA to convert it to a double-pulse amplifier.

Experimental realization of an optical parametric amplifier for a Ramsey-type measurement

As discussed in section 2.4, even with broadband ultrafast pulses, it is possible to perform high precision spectroscopy by using the temporal phase coherence as obtaind from a frequency comb laser. A NOPCPA is used to amplify two comb laser pulses to reach enough peak power for upconversion of the IR pulses to shorter wavelengths. The instantaneous nature of parametric amplification therefore requires also two pump pulses, which are temporally separated according to the repetition rate of the FCL. For many reasons it is desirable to amplify with pump pulses that are essentially equal. The sensitive dependence of the signal phase on the intensity and the direction of the pump pulse puts in fact strict requirements on the quality of the "equality" of the wavefronts of the pulses and the intensity. The previously mentioned simulations [73] have shown that already a difference of 0.2 mrad in the direction of the pump pulse changes the phase mismatch considerably and therefore has a significant impact on the spectral phase and power resulting from the amplification process.

Variations in the pump intensity exhibit a complex influence on the amplified pulses. Besides the direct impact on the signal gain, which scales exponentially with the pump intensity (in the absence of saturation), the wavelength-dependent phase mismatch in NOPCPA results in a wavelength dependence of the parametric gain. This can lead to significant changes in the spectral shape of the pulse and therefore in the Fourier-limited pulse duration. A change of 4% in the pump intensity can lead to a change by 5% in the amplified pulse duration [73] and therefore of the peak intensity. This is significant as the experimentally

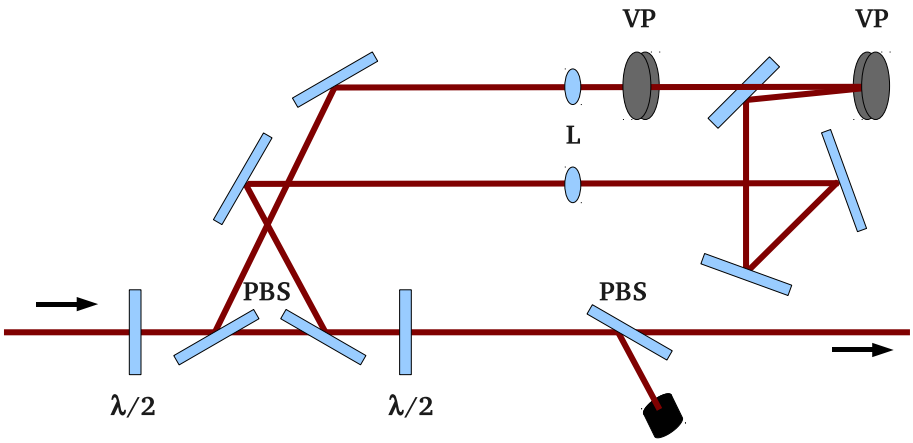

Figure 3.4: Relay-imaged delay line with two vertical periscopes and an odd number of reflections to facilitate a perfect spatial overlap between the original and the delayed beam. L: lenses with equal foci, PBS: polarizing beam-splitter, VP: vertical periscope, arrows indicate the direction of the beam.

determined power law that relates the energy in the 15^{th} harmonic to that of the fundamental is 7 ± 2. So the pump-pulse peak intensity must be kept equal within 5% in order to produce XUV pulse-pairs that do not differ by more than 50% in energy.

The considerations above have a big impact on the layout of the NOPCPA, as any differences in the spatial intensity and phase front of the pump pulses will translate into a spatial variation of f_0 in the spectrum of the signal-pulse pair after amplification. In order to minimize this and other effects, the pump pulse has been split in two identical replicas, separated by the repetition time of the FCL. In order to maintain the spatial intensity- and phase-profile of the delayed replica, it must be relay imaged onto the beam path of the original pulse. However, straightforward relay-imaging is not enough, because the spatial profile of the pulse is inverted in such a setup. Figure 3.4 illustrates how the delayed replica is spatially overlapped properly with the path of the original pulse, using two periscopes and an odd number of reflections. The ratio between the pulses is set with a $\lambda/2$-wave plate in front of the delay line. The wave plates afterwards rotates the polarization of the pulses by 45° to project them onto the same axis with a subsequent polarizing beam splitter. To

ensure that the alignment of the replica pulse matches the original, a Shack-Hartmann sensor has been used to align the position, direction and divergence of the delayed pulse. The alignment was readjusted on a daily basis. The differences in direction and displacement between the pulses were on the same level as the effects of air turbulence and acoustic influences (mechanical vibrations) in each individual beam line. The displacement between the pulses stayed within 10 μm. The (relative) direction of the beams fluctuated within several μrad.

The necessity of using polarizing beam splitters to obtain a well-defined polarization in the NOPCPA costs 50% of the energy of the pulse from the regenerative amplifier. However, the remaining energy of 0.5 mJ per pulse is still high enough to saturate the gain in the power amplifier that follows. Because the amplification of the pump pulses is based on stimulated emission from two, doubly passed, flash-lamp pumped Nd:YAG crystals, the second pulse will travel through a medium that has been depleted in gain by the precursor. This happens twice in the double-passed power amplifier. To compensate for the different gain of the two pulses, the second one is injected in the power amplifier with a higher energy. The experimentally determined injection ratio of 2 : 3 between the pulses, results in two equal pulses at 1064 nm after the power amplifier, each of them containing $140-180$ mJ in ≈ 50 ps. With a conversion-efficiency of $\approx 60\%$ to 532 nm by frequency doubling in a 5 mm long BBO crystal there is enough pump energy (85-110 mJ) to amplify infrared pulses in the NOPCPA beyond the mJ-level.

The excitation scheme with two ultrashort, and therefore broadband pulses, can lead to unwanted excitation to neighboring helium nP states in the helium atom. The obvious way to prevent this is to reduce the spectral bandwidth of the amplified pulses. However, a simple reduction of the linearly-chirped seeding spectrum comes at the cost of a reduced output of the amplifier due to the instantaneous nature of the amplification process. To match the seed pulse to the pump-pulse duration, a stretcher with 1200 l/mm gratings in a $4f$ geometry was built, with a group-velocity dispersion (GVD) of ≈ 690000 fs^2. A movable and adjustable slit is positioned in the Fourier plane of this stretcher to adjust the bandwidth and central wavelength of the seed pulse (Fig. 3.5). This stretcher supports a spectral bandwidth up to ≈ 40 nm around a central wavelength of 770 nm. The geometry of the amplifier (Fig. 3.6) was

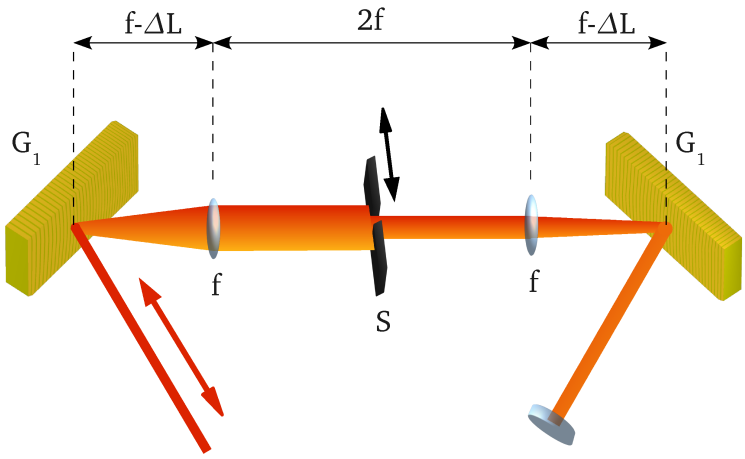

Figure 3.5: The used grating-based stretcher in the $4-f$ geometry with a movable, adjustable slit (S) in its Fourier plane. Gratings G_1 and G_2 with 1200 grooves/mm, $f = 20$ cm, $\Delta L = 1.2$ cm.

only slightly changed compared to [89]. To compensate the intensity loss due to the reduction of the energy in the pump pulses that came about with the double-pulse operation, the beam size in the last stage of the NOPCPA has been reduced by changing the relay-imaging telescope in this branch. Also the FCL has been adapted to seed the narrow-band operation of the NOPCPA with an appropriate set of chirped mirrors. For the experiments with helium the NOPCPA is configured to amplify a bandwidth of 6 nm to energies of 5 mJ per pulse. Compression and spatial filtering leave up to 2 mJ per pulse for HHG, which is discussed in the last section of this chapter.

The differential phase-shifts, which occur in the amplification of pulse pairs in the NOPCPA, have been extensively investigated. The following section reports on the phase measurement setup (PMS) and the findings of this analysis.

3.3 Phase measurement setup

Amplification of a wave packet (pulse) can result in a shift of its CEP. Although the NOPCPA scheme ideally does not alter the phase of the amplified field, deviations from perfect phase matching ($\Delta k = 0$) result

in spectral phase shifts, which can result in a change of the CEP after amplification. The possibility of different CEP shifts in the two amplified pulses demands to measure the differential CEP-shift *between* the pulses, because the spectrum of the pulse pair is determined by this phase shift (see Eq. 2.40).

A setup, dedicated to detect and measure those phase shifts using spectral interferometry was built and is introduced here. The NOPCPA is placed in one arm of a Mach-Zehnder interferometer so that a fraction of the amplified pulses is recombined with the unamplified original pulses and projected via a grating on a CCD-camera, where two spectral interferograms (one for each pulse pair) are detected. A combination of two Pockels cells (Lasermetrics 5046E) is used, one to improve the contrast of the two interferograms (PC1), and the other (PC2) for spatially separating the interferograms on the CCD. PC2 rotates the polarization by 90 degrees within a few nanoseconds between the two pulse pairs. Combined with polarization optics, this rotation results in a vertical displacement for the two interferograms on the CCD. The order of the projection (up-down) can be altered by changing the timing of PC2. A scheme of this setup can be found in figure 5.4 in chapter 5. Note that this setup has been adjusted to satisfy the needs of the helium spectroscopy experiment. The focal length of the lens, used to project the spectral interferograms on the CCD, was doubled to 40 cm in order to adjust the spectral resolution of the device to the amplified bandwidth. The photonic fiber, that is used to accurately overlap the beams from the two interferometer arms, has been replaced by a large mode area photonic fiber to increase the energy that can be coupled into this fiber without introducing nonlinear effects. For this reason the pulses are also stretched to approximately 10 ps before incoupling into this fiber. The final important improvement to the setup is a motorized moving aperture in the Mach Zehnder interferometer beam path of the amplified pulses. This aperture is used to map out the spatial variations of the phase shift across the wavefront of the laser beam. This is necessary to investigate the spatial dependence of the differential CEP shift because the fraction of the pulse that is coupled into the fiber does not exactly correspond to the entire pulse, and is therefore not representative for the total effective phase shift in the beam. The detected spatial phase shift between the pulses appears typically as a phase-front tilt, which can be detected by

simply scanning the angular dependence within the beam profile at a fixed distance to the center of the beam (effectively scanning the position along the donut-like beam profile as it is used for the HHG). More complicated patterns are not expected nor found because of the spatial filtering of the amplified pulse pair in a 80 μm large pinhole, employed between the NOPCPA and the PMS.

The delay between the amplified and the original pulses determines the period of the fringes in the interferograms. The phase (fringe position relative the spectral envelope) of the interferogram depends on the difference in phase accumulated in the respective interferometer arms, and most importantly on the phase-shift due to amplification in the NOPCPA. Also the alignment of the interferograms relative to each other on the CCD detector is interpreted as a phase difference. For the case where the interferogram of the first pulse is projected in the top half of the CCD (and therefore the other one in the bottom), the phase of the two interferograms can be expressed as:

$$\begin{aligned} \phi_{11} &= \phi_{MZ} + \phi_{amp1} + \phi_{CCD1} \\ \phi_{22} &= \phi_{MZ} + \phi_{amp2} + \phi_{CCD2}, \end{aligned} \tag{3.2}$$

where ϕ_{nm} denotes the n^{th} interferogram formed by the m^{th} pulse with the original pulse. The phase ϕ_{MZ} refers to the Mach-Zehnder interferometer alignment and is assumed common for both pulses. This assumption is valid for the small delay time of a few nanoseconds between the two pulses, because the mechanical jitter and drifts on the optical table takes place at much longer timescales. The amplification related phase shift of each pulse is denoted with $\phi_{amp1,2}$. The alignment of the interferograms on the camera is independent of the actual pulse that is projected on the CCD. Therefore the index of ϕ_{CCDn} ($n = 1, 2$ where 1 is the upper and 2 is the lower position on the CCD) denotes only the interferogram under consideration.

As mentioned before, Pockels cell PC2 can rotate the polarization of the pulses such that the projection order (up-down on the CCD) is reversed. By comparing the differential phase shifts for both situations, the alignment-induced phase shift ($\phi_{CCD1,2}$) can be eliminated. In the experiment this switching of the projection is done every second. In the situation, where the first pulse (with its original pulse) is projected onto

the position of the second (lower) interferogram, the phase readouts of the interferograms become:

$$\begin{aligned}\phi_{12} &= \phi_{MZ} + \phi_{amp2} + \phi_{CCD1} \\ \phi_{21} &= \phi_{MZ} + \phi_{amp1} + \phi_{CCD2}.\end{aligned} \tag{3.3}$$

The differential amplifier phase shift $\Delta\phi = \phi_{amp1} - \phi_{amp2}$ can be now derived from the difference in phase of the interferograms by subtracting the values for the two projections:

$$(\phi_{11} - \phi_{22}) - (\phi_{12} - \phi_{21}) = 2(\phi_{amp1} - \phi_{amp2}) = 2\Delta\phi. \tag{3.4}$$

The comb-like spectrum of the amplified pulse pair is then determined by adding the detected differential phase shift to the CEP-shift of the original FCL (see Eq. 2.40).

After the amplifier phase shift determination, a coherent pulse pair with a known phase (and therefore FC spectrum) is obtained at millijoule level which can then be used to generate a pair of high-order harmonic pulses in a noble gas medium to upconvert the comb to the XUV. The vacuum apparatus, in which the HHG and the spectroscopy of helium is done is introduced in the following section.

3.4 Harmonic generation and excitation setup

The electronic dipole transitions in helium that are addressed in the experiments, oscillate with a frequency of ≈ 6 PHz, corresponding to light with a wavelength close to 50 nm. This light is generated by means of high-harmonic generation, which was discussed in section 2.6. An outcome of this analysis is that two main electron trajectories contribute to HHG. One is a long trajectory, that emits a donut-shaped mode with a rather complicated phase structure. The short trajectory results in a Gaussian-like mode with a smooth phase evolution and a narrow (few mrad) emission cone on axis, in part due to constructive interference with the long trajectory emission. It is this short-trajectory mode which also shows the smallest phase dependence of the generated XUV on the intensity of the driving pulse (see e.g. [92]), which is therefore preferred.

The two modes emerge from different parts of the focus: the front part favors phase matching for the short trajectory, while optimal conditions for the long trajectory are found shortly behind the focal point. Destructive interference between the two contributions suppresses the emission from the intensity maximum at the focus. This spatial dependence allows to choose the favored mode, by focusing at the appropriate position with respect to the medium. For this reason the driving field is focused in most experiments, and the ones described in this thesis, in front of the gas jet in favor of the emission from the short trajectory.

The IR-pulse pair is shaped spatially before producing high-harmonics. This is done first by focusing the IR beam through a 80 μm diameter pinhole placed in a vacuum tube, resulting in a near-perfect Gaussian profile. The Gaussian shape of the beam is changed to a donut mode by sending the pulses through a mask that consists of a 1.9 mm diameter copper plate and an iris around it (typically set to a diameter of 6 mm). The iris is used to adjust the intensity in the focus to the level at which the desired 15^{th} harmonic emerges at the cutoff of the generated spectrum. In this fashion higher-order harmonics (corresponding to frequencies above the ionization threshold of helium) are suppressed, thereby reducing background signal due to direct ionization of helium to about 10% of the total signal. XUV is generated by focusing the IR (central wavelength 773.5 nm, $1.0 - 1.5$ mJ, 300 fs long pulses) with a 500 mm lens slightly in front of a krypton jet. This jet has an effective interaction length of 1 mm, and an estimated pressure on the order of 10 mbar.

The donut shape of the IR mode facilitates the separation of the fundamental IR from the XUV beam that is generated with low divergence (2 mrad) on the axis of the fundamental beam. The IR is blocked by a 0.8 mm pinhole placed in the image plane in the vacuum chamber of the afore-mentioned mask. The contrast of this separation was measured to be 1:27, which sufficiently suppresses AC-Stark effects in helium from the high intensity IR beam.

A metal grid, connected to an electrode outside the vacuum was placed underneath the krypton nozzle after the helium measurements were completed. With the grid it is possible to detect a signal of the electrons or ions produced in the focus of the IR-pulses. This signal was used to verify the quadratic relation between the amount of ionization

and the XUV-yield, which has been used for the experiment described in chapter 6 to extrapolate the phase shifts in the harmonics induced by ionization to zero krypton density. The relation between XUV intensity and ion density is expected to be quadratic, because ionization and HHG are of common origin in this tunneling regime. The difference is that ionization depends only on the density of atoms (and therefore ions), while HHG depends on the square of the density (number of HHG emitters). For more details see chapter 6.

After the HHG chamber, the XUV beam is sent into an interaction chamber where it perpendicularly crosses an atomic beam of pure helium or a 1:5 helium : noble gas mixture. This intersection is also crossed by an pulsed laser beam of 2 mJ energy per pulse, 50 ps duration and at a wavelength of 1064 nm, used to ionize the excited helium atoms for detection in a time of flight spectrometer. The ionizing pulse is timed 1 ns after the Ramsey-pulse pair to avoid temporal overlap and thus AC-Stark effects. The atomic beam is injected into the interaction chamber from a pulsed valve via two skimmers. The first skimmer has a round opening of 0.3 mm diameter. The second is a slit of 0.25 mm that can be moved across the atomic beam to adjust its direction with respect to the XUV beam. The distance between the skimmers is approximately 10 cm, leading to an atomic beam divergence of $3 - 4$ mrad. After interaction with the atomic beam the light is monitored in a grating-based monochromator and recorded using an electron multiplier, placed behind a 200 nm thin Aluminum foil.

All the elements described in this chapter together have lead to the first demonstration of an XUV comb and its application to spectroscopy in helium. The following three chapters report on the three major milestones achieved during my PhD research towards this goal, namely:

1) The characterization of the phase stability of mJ-level parametric amplification

2) Development of a double-pulse NOPCPA and an investigation of the induced phase shifts in the amplified pulses.

3) Upconversion of a frequency comb to XUV wavelengths and the application of this source for a Ramsey-type high-accuracy spectroscopic experiment in helium.

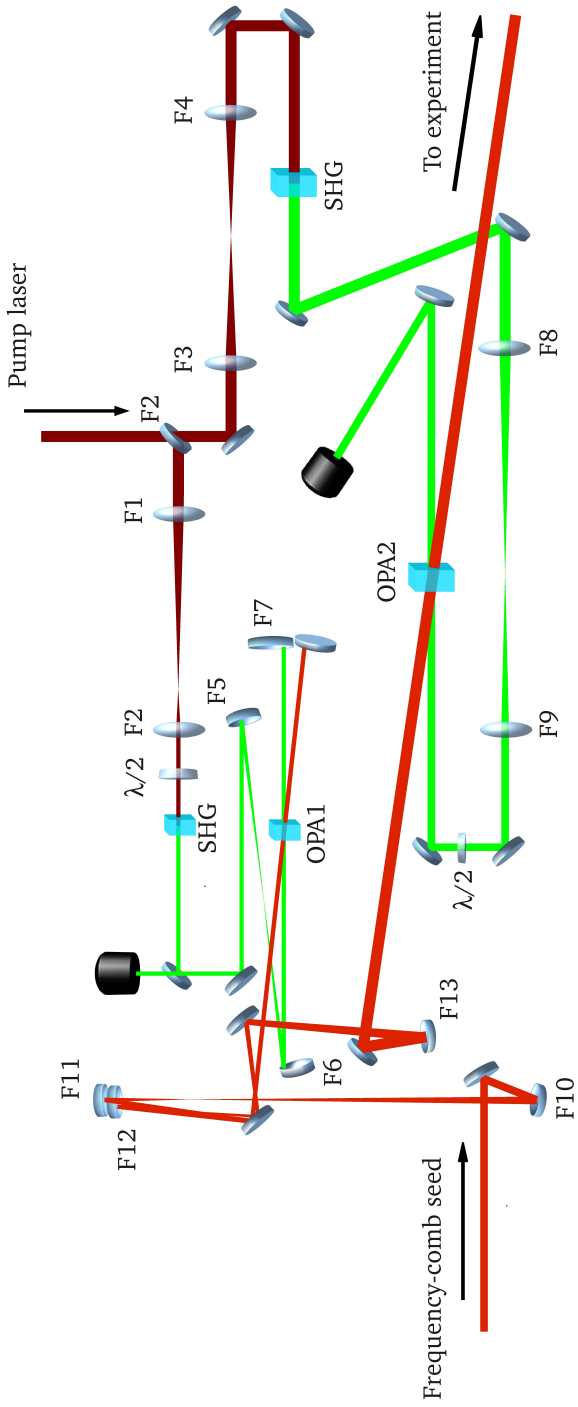

Figure 3.6: Scheme of the NOPCPA setup. SHG: second harmonic generation KDP-crystals, OPA: 5 mm BBO crystals, focal lengths: F1 = 550 mm, F2 = 150 mm, F3 = F4 = 750 mm, F5 = F6 = 375 mm, F7 = 250 mm, F8 = 600 mm, F9 = 400 mm, F10 = 300 mm, F11 = 125 mm, F12 = 50 mm, F13 = 500 mm

Phase stability of optical parametric amplification

The phase stability of broadband (280 nm bandwidth) TW-class parametric amplification was measured for the first time, with a combination of spatial and spectral interferometry. Measurements at four different wavelengths from 750 nm to 900 nm were performed in combination with numerical modeling. The phase stability is better than $1/25^{th}$ rms of an optical cycle for all the measured wavelengths of the amplified spectrum, and depending on the phasematching conditions in the amplifier.

Introduction

The generation and amplification of phase-controlled few-cycle laser pulses is a necessity for applications such as quantum interference metrology [19], attosecond science [93] and quantum control of e.g. molecular dynamics [94]. Intense, phase-stable few-cycle laser pulses have been produced using Ti:sapphire amplifiers and subsequent spectral broadening in filaments. However, filamentation in gas-filled hollow fibers [95], or directly in a gas cell [96], is difficult to scale beyond ≈ 0.2 TW. In parametric amplification phase-stable pulses, albeit at moderate energies of a few hundred microjoules [97, 98, 99, 100] have also been demonstrated. The generation of multi-millijoule level phase-controlled few-cycle pulses with terawatt (TW) intensity has not been demonstrated to date.

In this Letter we report what is, to the best of our knowledge, the first measurement of the phase stability of TW-class ultrafast amplification. The amplifier is based on non-collinear optical parametric chirped pulse amplification (NOPCPA), and was described already elsewhere in detail [89]. It consists of a double-pass pre-amplifier and a single-pass power amplifier using BBO crystals. The seed laser is a home-built 6.2 fs frequency comb oscillator, producing phase-locked 5.5 nJ pulses

at 75 MHz repetition rate. The carrier-envelope phase (CEP) stability is 1/46 rms of an optical cycle. The 532 nm pump laser provides 170 mJ pulses with a duration of 60 ps, and is synchronized to the oscillator laser. The system operates at a repetition rate of 30 Hz and is capable of generating 7.6 fs pulses at 2 TW (15.5 mJ after compression) when the normal full seed energy of 1 nJ per pulse is available.

The phase stability of the NOPCPA output is measured with linear interferometry. The advantage of this method over the frequently used $f : 2f$ technique [101] is that pulse intensity fluctuations (typically a few percent) do not influence the measurement; also the wavelength dependence can be measured. The system is based on a double interferometer, to be able to correct for optical path fluctuations due to external noise and drift (see Fig. 4.1). The interferometer path length variations, of the order of a wavelength, are too small to influence the CEP. Changes induced by thermal effects due to the20 mm of optical material in the NOPCPA path are small and are in addition compensated by a similar amount of material in the reference arm. The interferometer compares interference [102] between parametrically amplified and non-amplified frequency comb pulses with a spatial interference pattern generated by a reference He-Ne laser beam travelling the same path as the infrared (IR) light. About 50% of the IR seed light is split off (0.5 nJ) behind the stretcher as a phase reference; the He-Ne laser is coupled in both arms via this beam splitter. Several telescopes are used to match the beam parameters for the He-Ne laser and the IR beam at the end of the interferometer. The remaining 0.5 nJ of the IR seed light is amplified in the NOPCPA up to 23 mJ at 30 Hz repetition rate with a 280 nm-wide spectrum. Because of the reduced seeding to the amplifier, this is slightly less than reported before [89], but still sufficient to generate pulses exceeding 1 TW. The pulses are measured before the compressor to avoid nonlinear effects in the interferometer in order to measure only the influence of parametric amplification. Negligible additional phase noise is expected from the compressor given its stable construction and small compression ratio of 1:2000 [103].

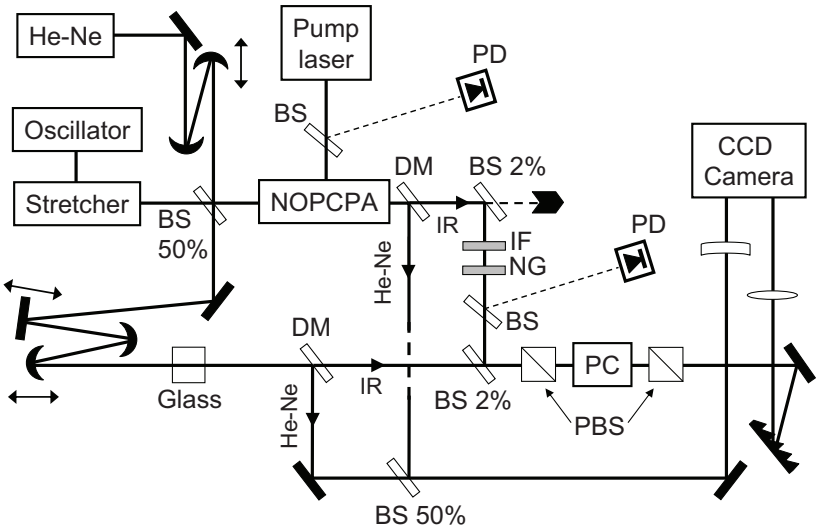

Figure 4.1: Setup used to measure the phase stability of the TW NOPCPA system. The path through the NOPCPA is 5 m, while the recombination section is in reality only a few tens of cm. BS: beamsplitter, DM: dichroic mirror, PD: photodiode, IF: interference filter, NG: neutral grey filter, PBS: polarizing beamsplitter, PC: Pockels cell, IR: infrared beam, G: grating 1200 lines/mm.

4.1 Setup

Both the IR and He-Ne laser beams are recombined individually with their respective reference beams behind the amplifier. The IR beam is attenuated using 2% beam splitters and a 10^{-5} filter to match the intensity with that of the reference pulses. Also, an interference filter is inserted here (bandwidth 10 nm, with a wavelength centered at either 750, 795, 850, or 900 nm), so that the wavelength dependence can be investigated. A home-built spectrometer is used to measure spectral fringes from the IR pulses on a CCD. The delay between amplified and reference pulses is set such, that as many as 10 fringes are visible over the 10 nm bandwidth. A spatial interference pattern is recorded on the same CCD as a length reference by recombining the He-Ne laser beams at a small angle on a 50% beam splitter.

Measurements of the phase are performed by recording every third pulse of the amplifier for several minutes. The phase is extracted from the two interference patterns using a Fourier-method described in [104], taking the difference in wavelength between He-Ne and amplified beam

into account. In Fig. 4.2 the result is shown for a typical measurement at 850 nm. The pump laser intensity stability is 1% in this case, while the amplifier output stability ranges from 6% at 750 nm, to 1.3% at 900 nm. The IR and He-Ne phase individually fluctuate due to external influences, but the difference is rather stable. With the NOPCPA switched off, a minimum phase noise detection limit of 0.09 rad (rms) is found at 795 nm. For the measurement of Fig. 4.2, correcting for this detection limit, a rms phase noise of 0.27 rad at 750 nm, 0.23 rad at both 795 and 850 nm, and 0.10 rad at 900 nm (1/63 of an optical cycle) results.

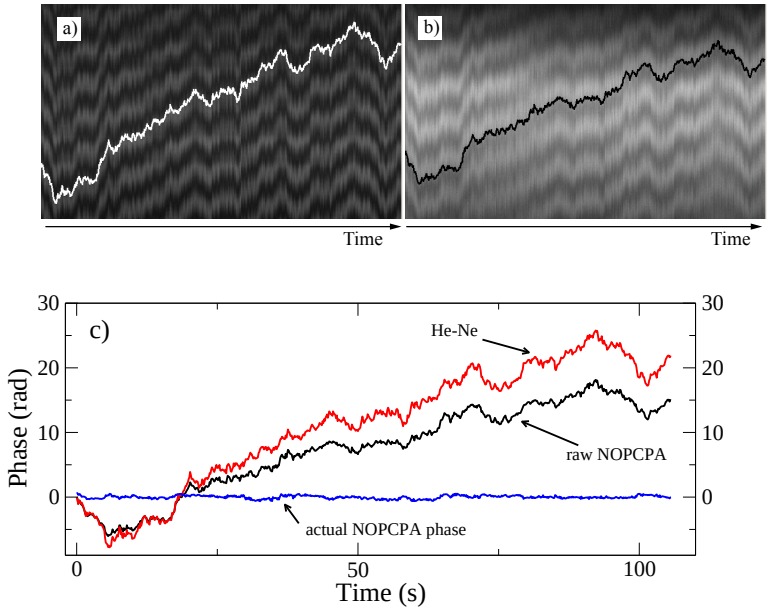

Figure 4.2: Evolution in time of the interference pattern for He-Ne (a) and NOPCPA (b) (λ = 850 nm) together with the derived phase traces, which are also depicted in c) (He-Ne: red and raw NOPCPA: black), as well as the corrected phase noise of the NOPCPA (see text).

4.2 Results and diuscussion

Theoretically the phase of the amplified beam is influenced mostly by the parametric process itself, and slightly by (cross-)phase modulation due to nonlinear refractive index effects. For the latter, phase fluctuations on the order of 0.01 rad are expected, based on a calculated nonlinear

phase shift of 0.36 rad for the amplifier, and a pump intensity variation of a few percent. The influence on the phase of the signal beam due to parametric amplification is given by [72]:

$$\varphi_s(L) = \varphi_s(0) - \frac{\Delta k}{2} \int_0^L \frac{f}{f + \gamma_s^2} \mathrm{d}z \tag{4.1}$$

here $f = 1 - I_p(z)/I_p(0)$ is the fractional pump intensity depletion, and $\gamma_s^2 = \omega_p I_s(0)/\omega_s I_p(0)$. In this expression L is the interaction length, Δk is the phase mismatch, I_s is the seed intensity and ω_s and ω_p are the seed and pump frequencies. Eq. 4.1 states that there is a coupling between pump intensity and phase of the seed pulse. To estimate the influence of this effect, numerical simulations have been performed for a three-pass NOPCPA system using a split-step Fourier algorithm [73]. In Fig. 4.3 the results are shown for the calculated phase matching conditions and shifts, together with the calculated and experimental spectrum for the measurement depicted in Fig. 4.2. From Fig. 4.3 it can be seen that the pump-induced phase shifts are proportional to $-\Delta k$, as predicted by Eq. 4.1.

A direct quantitative comparison with the experiment is hampered by the extreme sensitivity of Δk on the angles in the three different amplifier passes. This means that the experimental Δk is difficult to determine. It is, however, clear that the calculated phase shifts as a function of pump-power variations are several times lower then the typical values seen in the experiment, especially at 750 nm. We attribute this to a combination of slightly differently aligned passes (leading to local larger Δk), possible (pump) beam pointing fluctuations, and the influence of pulse-to-pulse intensity variations on the phase readout.

To detect the correlation between the (pump) intensity and the phase we use Spearman's rank correlation coefficient (RC), as it is particularly suited for noisy datasets [105]. An RC of $(-)1$ signifies full (anti)correlation, while 0 means no correlation. With sufficient gain the RC should in principle incrase for a larger Δk, and change sign together with Δk. For the spectrum shown in Figure 4.3 no significant correlation could be detected between pump intensity and output phase. However, the situation is different when the NOPCPA is less well aligned, leading to a bigger Δk and a strongly modulated spectrum. Significant (anti)correlations can then sometimes be observed, such as the case

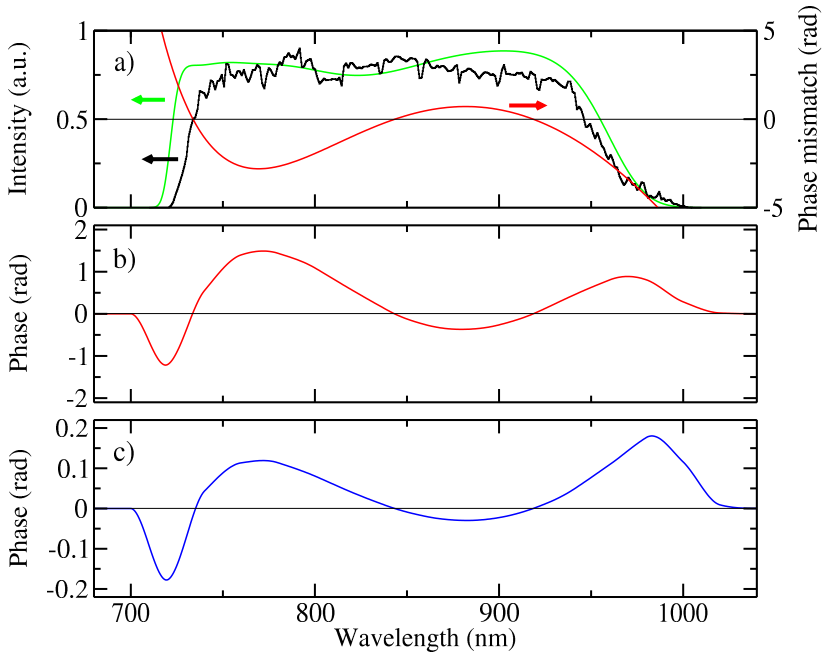

Figure 4.3: (a) Measured spectrum of the amplified NOPCPA output (black trace), along with a simulated spectrum for phase-matching angle $\theta = 23.887°$ and noncollinear angle $\alpha = 2.40°$ (green curve) and the phase mismatch curve ΔkL for a 5 mm long BBO crystal with the phase-matching angles as used in the simulation (red curve). (b) Total pump-induced phase shift introduced by a complete pass through the amplifier according to Eq. 4.1. (c) Wavelength-dependent phase shift resulting from a 5% increase in pump intensity.

where the phase-pump intensity RC changes sign from +0.4 at 750 nm to −0.3 at 795 nm. In this situation over-saturation (back-conversion) was observed at 795 nm. At other wavelengths the RC is normally too small to draw conclusions.

To further study the Δk effects at a fixed wavelength of 795 nm, we deliberately induced a strong phase-mismatch by rotating the last crystal from $\theta \approx 23.8°$ to $\theta + 0.06°$. The pump intensity was modulated by about 10% to make the measurement more sensitive to correlations. The result is shown in Fig. 4.4; the RC changed sign from +0.4 to −0.2, in qualitative agreement with simulations. A strikingly big phase jump of 1.7 rad is seen that is not present when the NOPCPA system is switched off. Such a big phase shift is theoretically possible if the integral in Eq. 4.1

would stay large for a big Δk. This can be explained by assuming an average pump power of 7 GW/cm^2 (20% higher than initially estimated).

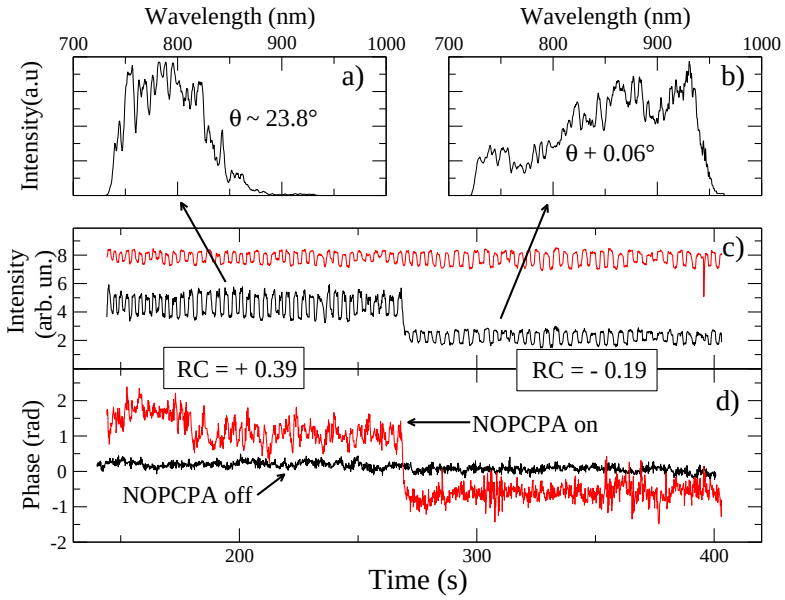

Figure 4.4: Influence of the phase-matching angle on the phase of the NOPCPA. (a),(b) NOPCPA spectra for two different phase-matching angles, seperated by 0.06° (c) NOPCPA-intensity at 795nm (black) and pump intensity (red). (d) Phase evolution with (red) and without (black) the NOPCPA switched on (For RC between pump intensity and phase see text).

4.3 Conclusions

In conclusion, we demonstrated phase-stable TW-class parametric amplification for the first time. On average the phase stability is better than 1/25 of an optical cycle across the amplified spectrum for the measured pump laser fluctuations of 1% rms. The measured phase noise is several times larger than numerically simulated, but qualitative agreement is found for the expected Δk dependence. The average phase stability of 1/25 of an optical cycle gives an upper bound for the influence on the carrier-envelope phase when the pulses would be fully compressed,

demonstrating that TW peak power few-cycle laser pulses can be produced with NOPCPA.

Chapter 5

Phase stability of a double-pulse OPA

We demonstrate phase stable, mJ-level parametric amplification of pulse pairs originating from a Ti:Sapphire frequency comb laser. The amplifier-induced phase shift between the pulses has been determined interferometrically with an accuracy of ≈ 10 mrad. Typical phase shifts are on the order of 50-200 mrad, depending on the operating conditions. The measured phase-relation can be as stable as 20 mrad rms ($1/300^{th}$ of an optical cycle). This makes the system suitable for Ramsey spectroscopy at short wavelengths by employing harmonic upconversion of the double-pulses in nonlinear media.

Introduction

High-power phase-controlled ultrashort laser pulses are essential for various applications, such as attosecond science [106], quantum control of molecular dynamics [94] and Ramsey spectroscopy [107, 108, 19]. Stabilization and control of the phase φ_{CE} between the field and envelope of low power oscillator pulses was demonstrated several years ago [10, 9] and has revolutionized the measurement of optical frequencies. The frequency comb technique has become a standard tool for spectroscopy in many laboratories across the world. The spectral range of frequency comb lasers is typically in the near-infrared, but can be extended through nonlinear interactions. One example is the generation of harmonics from frequency comb laser pulses to extend the spectrum to the extreme ultraviolet (XUV). Aiming at Ramsey spectroscopy of Helium at ≈ 50 nm, we pursued the amplification of two subsequent pulses from such a laser to an energy level suitable for generation of the desired wavelength. Direct excitation with the upconverted pulses should allow measurement of the ground state energy of helium and hydrogen-like atoms with an unprecedented precision for tests of e.g. quantum-electrodynamics. The

minimum requirements for such an experiment are two phase-coherent pulses with enough intensity to generate harmonics. One approach is to use a Michelson interferometer to split an amplified pulse in two, as is e.g. done in [108]. The drawback of this method is that the resolution is limited by the calibration of the pulse delay and by the stability of the interferometer. An interesting technique that avoids those problems was demonstrated in [16, 109], where an external cavity was used to build up the desired power level for high-harmonic generation from a frequency-comb pulse train. Alternatively, one can amplify multiple subsequent pulses from a frequency comb laser for harmonic upconversion. With pulses amplified to a level of tens of μJ, high-resolution direct frequency comb spectroscopy was demonstrated at 212 nm and 125 nm [19, 20]. To reach the XUV spectral region a higher pulse energy is required.

Phase-stable amplification of single ultrashort pulses using Ti:sapphire amplifiers [95, 96] and parametric amplification [89, 91] has been demonstrated before. For Ramsey-type experiments the latter approach is advantageous, as it is theoretically capable of amplifying two subsequent pulses in the same way while maintaining saturation for each pulse. It also gives more freedom in choosing the output spectrum. Here we show that noncollinear optical chirped pulse amplification (NOPCPA) can indeed be extended to two-pulse amplification (with a time separation of 6.6 ns) while maintaining a high mutual phase stability. This phase stability is one of the key issues, and therefore investigated in detail, as any phase deviation will be multiplied in harmonic upconversion to the extreme ultraviolet. Also the stability of the amplified pulses has been investigated because variations in the intensity can induce additional phase shifts in the harmonic generation process itself [110].

In contrast to the previous working conditions of our NOPCPA system (where we generated single laser-pulses with a spectral width of ≈ 300 nm [89]) we limited the spectral width of the pulses to 30 nm. This bandwidth is a good compromise between harmonic conversion efficiency and spectral power density in the XUV, and it reduces complications due to wavelength dependence of the phase [91]. This is the condition that will be used for harmonic generation in later experiments. As a result the energy per pulse is $1 - 2$ mJ. The phase shift relative to the comb laser of the two pulses induced by the amplification has been measured using

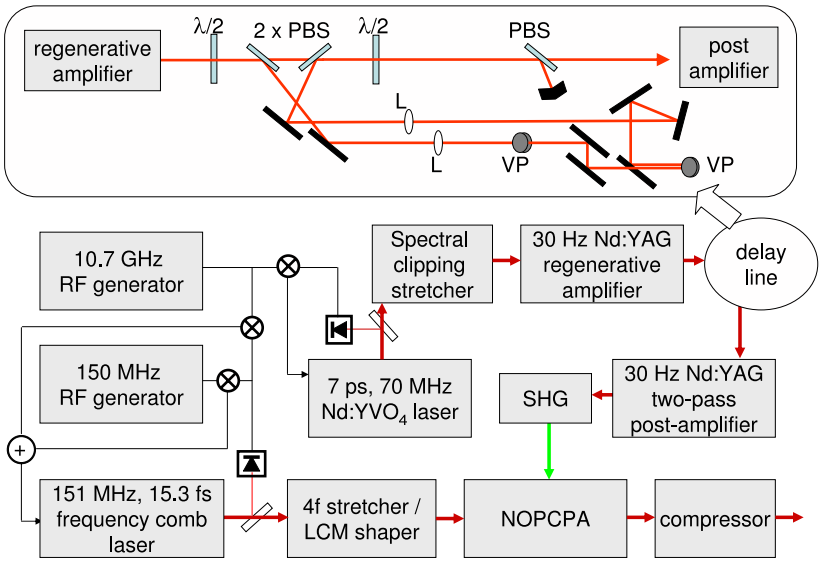

Figure 5.1: Schematic of the noncollinear optical parametric chirped pulse amplifier (NOPCPA), showing in detail the relay imaged delay line that splits the pulses in two replica. PBS: polarizing beam splitter, VP: vertical periscope, LCM: liquid crystal modulator, L: relay image lens f = 50cm, SHG: second harmonic generation

spectral interferometry in a Mach-Zehnder interferometer. In addition the spatial dependence has been investigated, as well as the influence of unequal amplification of the two pulses on their relative phase.

5.1 Amplification of pulse pairs

Ramsey spectroscopy requires a well known and stable phase relationship between the pulses used for excitation of a transition. We make sure that this is the case by employing the pulses from a frequency comb laser as a seed for the NOPCPA. However, optical parametric amplification can induce a phase shift depending on the phase-matching conditions of the amplifier and the intensity of the pump pulse [91, 72, 73]. The phase of the amplified seed pulse φ_s is given by [72]:

$$\varphi_s(L) = \varphi_s(0) - \frac{\Delta k}{2} \int_0^L \frac{f}{f + \gamma_s^2} dz \tag{5.1}$$

Here the fractional pump intensity depletion is defined as: $f = 1 - I_p(z)/I_p(0)$ and $\gamma_s^2 = \omega_p I_s(0)/\omega_s I_p(0)$. I_p and I_s are the intensity of the pump and the seed respectively, while ω_p and ω_s are the corresponding angular frequencies. L is the length of the parametric interaction. A change in the alignment in the range of 0.01° for the noncollinear angle between pump and seed changes the phase of the amplified pulse on the order of 0.3 rad after 5 mm of propagation in the BBO-crystal. Amplification in a NOPCPA of two subsequent laser pulses from the oscillator requires two strong pump pulses separated by the period of the frequency comb. Because of the reasons stated above, these two pulses need essentially the same intensity profile and wave front. We realized this by a modification in the pump laser of the previously demonstrated single pulse NOPCPA system [89].

The starting point of the pump laser is a Nd:YVO_4 oscillator, emitting 7 ps pulses at a repetition rate of 70 MHz. Clipping the spectrum stretches the pulses to ≈ 100 ps duration. The stretched pulses are amplified at 30 Hz repetition rate in a diode-pumped regenerative Nd:YAG amplifier, where the energy is boosted to 2 mJ per pulse. The required two pump pulses are produced by implementing a delay line behind the regenerative amplifier, where part of the energy is split off, delayed and recombined with the original beam using polarizing beam splitters. The total arm length of the delay line is ≈ 2 m, and corresponds exactly to the pulse delay of the comb laser of 6.6 ns. Fig. 5.1 shows a scheme of the laser system together with a detailed layout of the delay line.

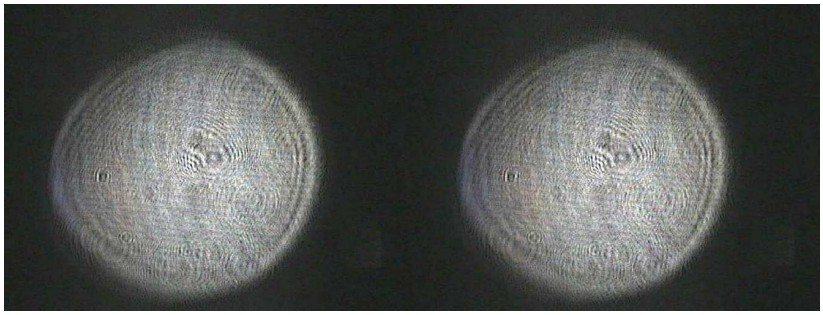

Figure 5.2: Spatial profiles of the 1st and 2nd pump pulse after the post-amplifier. The small diffraction patterns are due to dust particles on the camera and other optics, and are not part of the actual beam profile.

Since the NOPCPA is very sensitive to the alignment (see e.g. [73]) the two pulses generated by the delay line need to have identical wave fronts and spatial profiles. This is achieved by a 4f relay-imaging system in the delay arm. The image inversion of the 4f system is counteracted by using an odd number of mirror reflections together with two vertical periscopes. To meet the requirements for precise identical alignment of the two pump pulses in NOPCPA, they are compared on a CCD camera behind the postamplifier at a distance of 6 m after the delay line in the relay-image plane, and at 9 m distance out of the relay-image plane. Figure 5.2 gives an example of the spatial profiles of the two pump pulses 9 m after the delay line, showing that they are essentially indistinguishable after this procedure. In this Mach-Zehnder arrangement half of the power is lost when projecting the pulses onto a common polarization, so that each of them contains 0.5 mJ of energy. The resulting beam is enlarged and sent into a flash-lamp pumped Nd:YAG postamplifier (Fig. 5.1), where it reaches 180 mJ per pulse at 1064 nm. The relative intensity between the pulses can be adjusted using the half-wave plate in front of the delay line to compensate for the gain depletion seen by the second pulse in the postamplifier. Seeding the postamplifier with 50% more energy in the second pulse leads to equal output energy for both pulses.

Making the power and direction of the pump pulses the same is not yet enough for proper amplification. The time between the pulses must match the round-trip time in the frequency-comb oscillator exactly. This means that the repetition rate of the frequency-comb oscillator must be adjusted as the relay-image condition fixes the delay-line length. After coarsely setting it to the right value, we scan the delay between the seed and the pump beam in the NOPCPA while looking at the power level of the amplified pulses. If the delay between the seed pulses does not match the delay between the pump pulses, the ratio between them will vary after amplification. This information is used for fine-tuning the repetition rate of the frequency comb, until both pulses are amplified in the same way. The result is a stable intensity ratio between the amplified pulses on a level of $3\% - 6\%$ rms. Fig. 5.3 shows typical energy traces of the two amplified pulses together with their ratio.

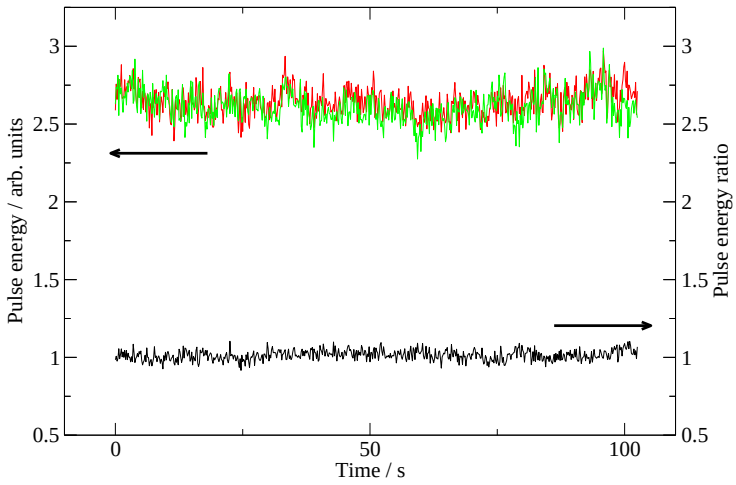

Figure 5.3: Energy of the first and second amplified pulse (upper, red and green traces) and the ratio between them (lower, black trace). The energy stability here is 3.6% and 3.8% rms for the first and second pulse respectively and 3.3% rms for the ratio between them.

5.2 Measurements of the amplifier phase shift

The phases after amplification are measured relative to the frequency comb pulses with a Mach-Zehnder interferometer, as depicted in Fig. 5.4. In this setup half of the seed beam is sent into the NOPCPA, while the other half is split off as a reference. This reference is combined with a small fraction of the amplified pulses on a 5% beam splitter and sent through a single-mode optical fiber. Thus the mode profiles of the two beams are filtered and a perfect overlap of the amplified and reference pulses after the interferometer is established.

The amplified pulses are delayed with respect to the reference by about 1 ps, causing spectral interference in the combined beam. The interference fringes are detected with a spectrometer consisting of a CCD camera, a lens (f=20 cm) and a grating with 1200 l/mm. A Pockels cell (PC1) is used to select only the two pulses from the oscillator that give an interference signal. This Pockels cell is double-passed to provide a contrast better than 10000 : 1 within a bandwidth of 30 nm, rendering

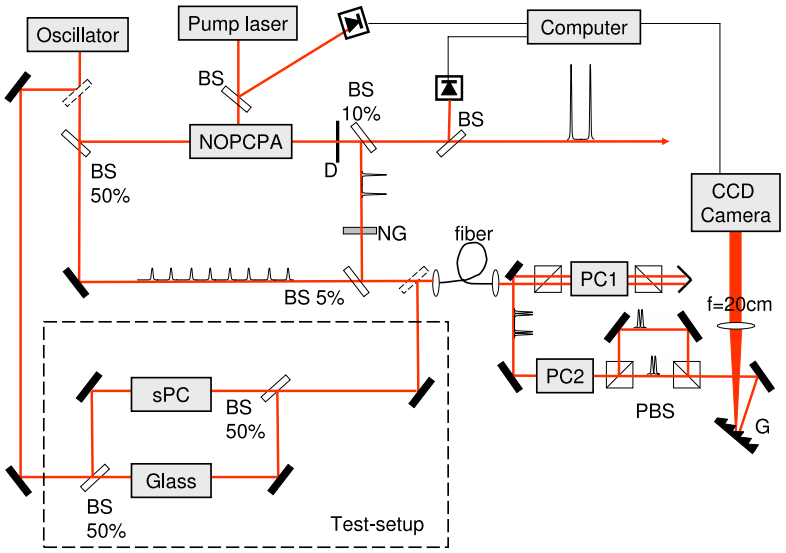

Figure 5.4: Mach-Zehnder interferometer for measurement of the differential phase shift accumulated during the amplification in a NOPCPA, and the setup used to test the reliability of the measurement (dashed box). BS: Beam splitter, PBS: polarizing beam splitter, PC1/2: Pockels cells, sPC - slow Pockels cell, NG: neutral grey filter, D: diaphragm, G: 1200 l/mm grating

the background due to other oscillator pulses essentially invisible within the exposure time of the camera (3 μs).

The two signal-reference pulse pairs are separated spatially using a second Pockels cell (PC2) and polarizing beam splitters in order to be able to analyze the interference patterns individually (see Fig. 5.5). The phase of the recorded fringes is determined using a Fourier transform based method, as described in [104]. This method determines the phase as a function of wavelength for every interferogram. By integrating this phase over a certain range and dividing it by the number of data points used, a single value for the phase is obtained, which reflects the actual position of the interference pattern. This phase of the fringes depends on many possible effects, which need to be taken into account in order to extract the influence of the amplification. These are: the alignment of the interferometer and fluctuations thereof, the actual part of the wavefront coupled into the fiber, nonlinear phase shifts in the fiber, spatial and temporal inhomogeneity of the Pockels effect, the contrast of the separation in PC2, and finally the phase shift induced in the NOPCPA.

In the following we give a detailed overview of how these issues are dealt with.

The phase shift of the interferograms is determined mainly by the relative lengths of the ≈ 10 m long interferometer arms, which can vary by a few μm due to environmental influence. However, these variations are virtually identical for both pulse pairs, due to the small temporal delay (6.6 ns) between them. Therefore they cancel when evaluating the phase difference between the upper and the lower interferogram.

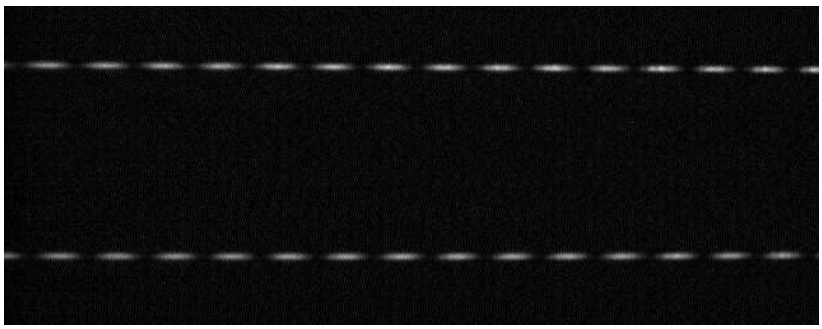

Figure 5.5: Spectral interference fringes between the two amplified pulses and their respective reference pulses

Misalignment of the two beam paths after PC2 can lead to a small horizontal shift of the two fringe patterns. To cancel this effect and extract only the relative phase shift of the amplified pulses we employ an alternating switching scheme: In one configuration the polarization of the first pulse is rotated, the other configuration rotates the polarization of the second pulse. In this way we can exchange the paths of the first and second pulse towards the CCD, which means that we exchange the contribution of the NOPCPA phase shift on the phase of the fringes, but not the contribution of the alignment. This switching is performed every five seconds. The differential phase shift of the amplification can be now determined by subtracting the detected phase differences for both cases from each other. The contribution of the alignment disappears in the obtained phase trace, while the differential phase shift changes for the two switching positions of PC2. The resulting phase traces show a characteristic shape of a rectangular function, where a difference between the upper and the lower value gives *two* times the differential phase shift

between the first and second pulse amplified in the NOPCPA (see e.g. the lowest, black trace in Fig. 5.6.)

As mentioned before, when using the source for high harmonic generation, any phase shift is multiplied by the harmonic order factor. Therefore a high accuracy better then $1/200^{th}$ of an optical cycle in the infrared is required to identify the upconverted frequency comb mode in the XUV that is involved in the Ramsey excitation. The desired accuracy asks for additional testing of our measurement technique. We have performed such tests, using a Mach-Zehnder interferometer with a slow Pockels cell (sPC) instead of the NOPCPA in one of its arms (dashed box in Fig. 5.4). The Pockels cell was turned by 45°, to make it work as an electro-optic phase modulator without changing the polarization of the passing beam. It has a relatively long switching time of 60 ns in comparison to the time between the pulses. This still can produce small differential phase shifts in subsequent laser pulses traveling through the sPC. Two pulses are selected as in the normal measurement with PC1 and the introduced phase shifts are measured in two different ways. In one case the sPC in the interferometer is switched on and off, alternating between each measurement. The spectral interference between the pulse and its replica is recorded in a single interferogram that moves back and forth, corresponding to the phase shift induced by the sPC (see Fig. 5.6, the red and green traces). The differential phase shift between two subsequent pulses can be determined from two such measurements (one for each pulse). The comparison to the value measured instantaneously with the PC2-switching method used to determine phase shifts induced by the NOPCPA, gives a difference in the order of 5 mrad, confirming the reliability of the measurement method. Furthermore, comparing the spread in the values measured with the test scheme and the PC2-switching scheme (80 mrad rms and 10 mrad rms respectively, see Fig. 5.6, measurement time: 90 s), demonstrates the high precision of the method used. Another test was performed, measuring a zero phase shift, by keeping the sPC in the interferometer off. The results of five such measurements (measurement time: 90 s) gave a differential phase shift of (-2 ± 2) mrad, showing again the accuracy of the method.

PC2, which is used to separate the pulses before projecting them on the CCD camera, has a switching time of $\approx$ 5 ns, which is very close to the temporal separation of the pulses (6.6 ns). This leaves a

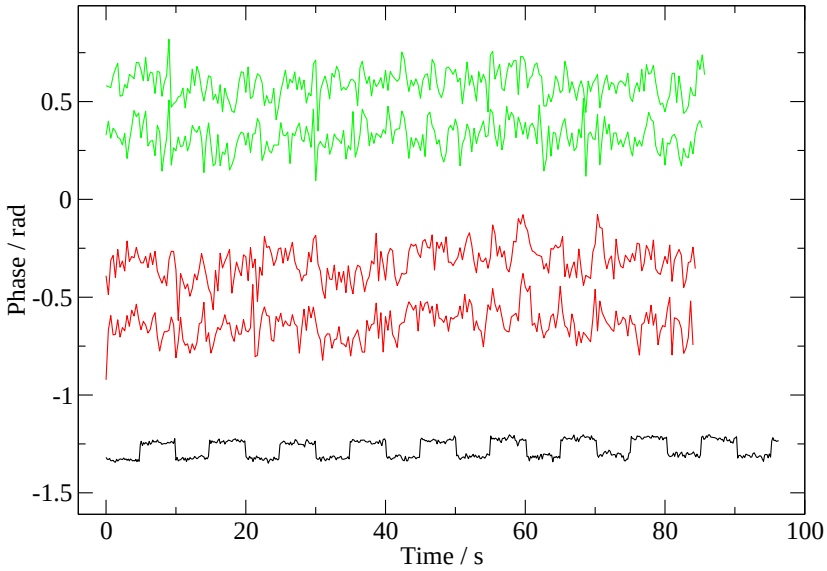

Figure 5.6: Artificial phase shift measured with the interferometric switching technique (black/lower trace) and tested in a single interferogram for each pulse, with alternate switching the phase shift on and off (first pulse - green/upper traces, second pulse - red/middle traces).

possibility for the pulses to leak fractionally into the other channel, due to the imprecise time delays introduced by the Pockels cell electronics. We have investigated the possible influence of such behavior by setting the switching point of the Pockels cell PC2 to slightly wrong positions on purpose. Using pulses with a differential phase shift of 55 mrad we could only see a significant effect if the amount of light leaking into the wrong channel became comparable to the pulse itself (20% or more). Under normal operating conditions (5% leakage) the effect can be neglected.

Another possible source of error can be the optical fiber, used for cleaning the mode profile and perfect overlap of the amplified and reference pulses in the Pockels cells. Sending ultrashort pulses through an optical fiber with a core diameter of 3μm may change the phase of the investigated pulses due to self phase modulation. The phase of each pulse could change in a different way, if they differ in intensity. To investigate this, we moved the slow Pockels cell (sPC) from the test setup (Fig. 5.4)

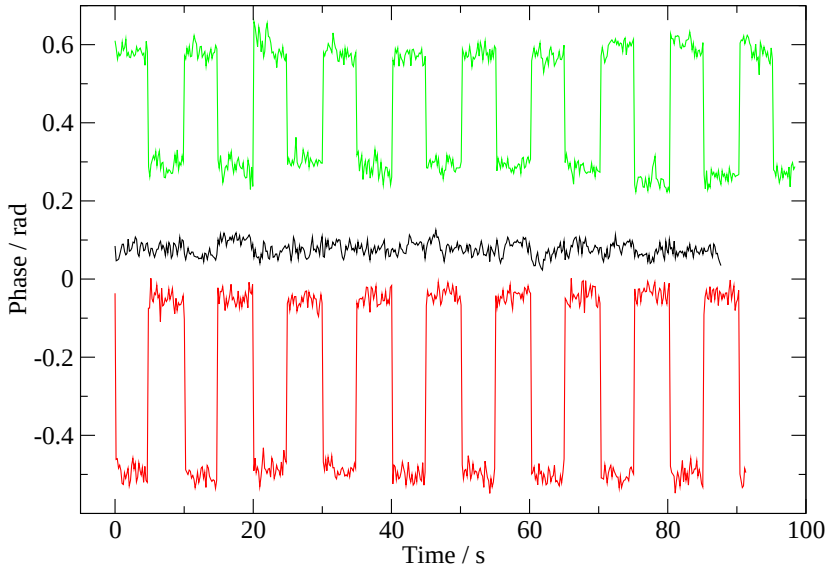

Figure 5.7: Phase traces, measured on three different days, showing two times the difference in phase shift of 151 mrad (upper/green trace), −227 mrad (lower/red) and −4 mrad (black/middle trace).

into the beam before the interferometer. Despite the slow switching time of this device we could change the intensity of subsequent pulses using a polarizer to a ratio of 5 : 4. Doing this in front of the interferometer makes sure that the phase shift in the interferometer is zero, if nonlinear effects in the fiber have no influence. The differential phase shift was measured with an intensity ratio between the two interferometer arms of 1 : 2 and no phase deviations have been detected.

The result of these tests is that the single-shot accuracy of the interferometer technique is better then 10 mrad. With this knowledge we investigated the influence of the NOPCPA on the phase of the pulses under different circumstances; in particular the stability of the phase between the pulses, spatial homogeneity, spectral dependence and the influence of unequal amplification on the phase shift.

Fig. 5.7 shows three typical examples of a phase shift difference measured under normal operating conditions. These examples are taken from measurement series recorded on three different days, corresponding to

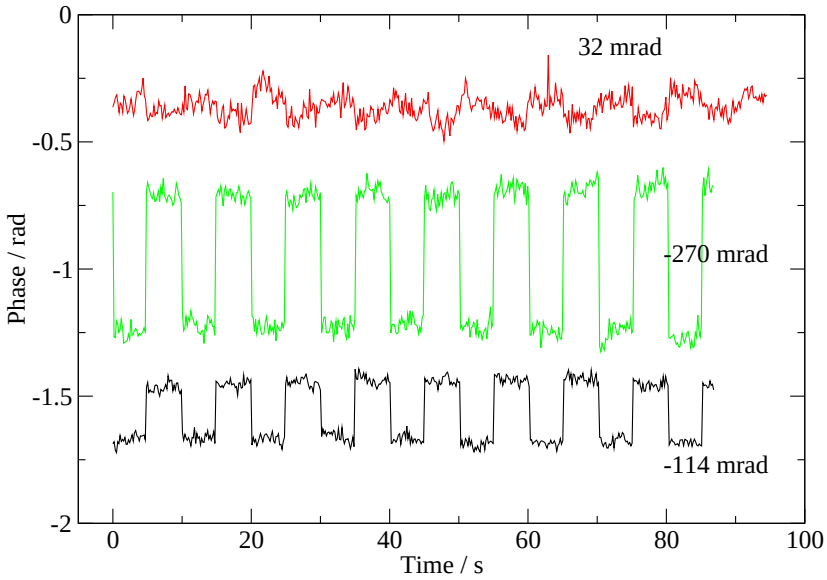

Figure 5.8: Different phase shifts of −114 mrad, 32 mrad and −270 mrad, emerging from different pump-intensity ratios between two pulses (equal pulses (black), second pulse stronger (red) and first pulse stronger (green) respectively with a ratio of 2:1).

slightly different alignments of the NOPCPA. The upper (green) trace corresponds to a difference in phase shift of 151 mrad with a rms variation over the measurement interval of 22 mrad. The difference in the lower (red) trace is as big as −227 mrad with a variation of 20 mrad rms. The black trace in the middle shows a phase shift of −4 mrad between the pulses and a variation of 16 mrad rms. Despite the relatively big change in the phase-shift difference of ≈ 380 mrad, the measured values spread only by 70 mrad (peak-peak) during the day. Notice that the short term stability of the differential phase shift does not depend on its actual value.

A dependence of the differential phase shift on the intensities of the pump pulses is expected from Eq. 5.1 and as well from the single pulse phase measurements performed previously [91]. We have investigated this for several operating conditions of the parametric amplifier. The influence of different intensities of the pump pulses on the phase shift is

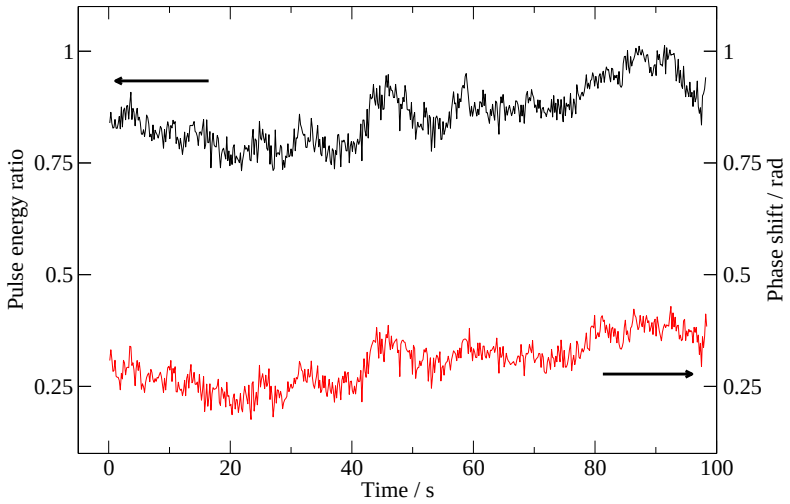

Figure 5.9: Ratio between the energies of the first and second amplified pulse (black/upper trace) and the measured phase shift (red/lower trace)

illustrated in Fig. 5.8. We have measured in three situations: one with equal pump power for both pulses and two with a ratio between the pump-pulses set such, that one seed pulse is amplified to half the energy of the other one. It results in three different values for the phase shift: -114 mrad for two equal pulses, -270 mrad and 32 mrad, for the first pulse stronger and second pulse stronger respectively. This behavior qualitatively confirms the model of NOPCPA presented in [72]. For normal (stable) operating conditions of the NOPCPA (see Fig. 5.3) the phase-intensity coupling is too small to be observed. In contrast, Fig. 5.9 shows a case with an unstable phase shift (red/lower trace) emerging from an exceptionally unstable ratio between the amplified pulses (black/upper trace). The Spearman rank-order correlation coefficient* gives in this case a clear correlation of $r = 0.95$.

The phase mismatch Δk is a function of the seed wavelength [73], which can lead to different phase shifts during amplification for different spectral components (see Eq. 5.1). We have investigated this dependence for changes of the phase of single pulses in our previous measure-

*Pearson's line. ar correlation coefficient is not appropriate, as it assumes a linear relationship between the variables, which is not the case here

ments [91] with a broad spectrum. In the present situation the spectrum of the amplified pulses is relatively narrow (30 nm) and most of it (20 nm) covers the CCD-Camera in the interferometer. This allows us to compare the differential phase-shifts of different spectral components, selecting the corresponding parts of the recorded interferograms for the analysis. The analysis of the differential phase shifts in three spectral regions with a width of 3 nm around 790 nm, 793 nm and 796 nm respectively, shows small deviations (typically < 10 mrad) from the mean values obtained by analyzing the whole spectral range at once. The deviation from the mean value is least for the central wavelength of the pulses and goes in opposite directions for the outer regions.

From Eq. 5.1 it can be seen that the induced phase shift depends on the phase mismatch Δk (which is inaccurately known [†]) and the fractional depletion of the pump beam. The latter depends strongly on the intensity of the pump beam, which also determines the conversion efficiency in the parametric process. A higher starting intensity will usually deplete the pump beam quicker, causing a bigger phase shift in the amplified pulses. Because the pump-pulse depletion in the first pass is negligible, hardly any phase shift is expected to occur there. In the second pass, however, there is more pump depletion and the pump beam is simply imaged (instead of relay imaged) onto the crystal, resulting in a significant divergence of the beam in the crystal. This leads to different noncollinear angles across the beam and therefore suboptimal conditions for parametric amplification. The contribution from this stage to the differential phase shifts was checked, by comparing it with and without the last stage of the amplifier. The amplification in the last crystal can be easily switched off by rotating the polarization of the pump beam therein. The measurements indeed confirm the expectations, giving a differential phase shift of -109 mrad for the whole NOPCPA and -125 mrad for the first two passes only. With a different alignment of the amplifier we detected a phase shift of -77 mrad in three passes and the same value without amplification in the last crystal. This is strong evidence for the assumption that the second amplification stage is the major source of the observed differential phase shifts.

[†]The phase mismatch is very sensitive to the angles in the parametric amplification . It is extremely difficult to measure them accurate enough to be able to determine Δk

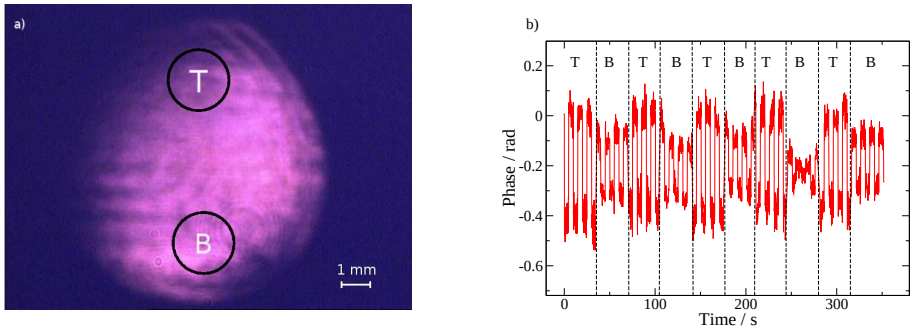

Figure 5.10: a) Intensity profile of the amplified pulses after the last amplification stage. The circles refer to the beam sections chosen for the measurement, depicted in: b) Measurement of the phase-shift difference for two sections of the amplified pulse pair (as indicated in 5.10 a). The dashed lines indicate the switching between the two sections. T/B - top/bottom section.

Finally, in a series of measurements we have investigated differential phase shifts in different sections of the amplified beam. Those phase shifts can vary up to ≈ 100 mrad across the beam or be as low as ≈ 30 mrad, depending on the alignment of the amplifier. The measured variation across the beam is of the same order of magnitude as the variations during a day at a fixed position in the beam profile. To detect whether the changes in phase really correspond to the chosen beam section (and not the time when they are measured), we took a series of measurements while switching between two positions in the beam during the data acquisition. Figure 5.10 b shows a phase trace taken by alternating the measured section between the two positions marked in Fig. 5.10 a. The phase shift in this case is -192 mrad in the upper part of the beam and -95 mrad in the lower section. This measurement clearly shows the temporal and spatial variations of the differential phase shift between the beams, giving two distinguishable values for the two sections, which on their own show temporal variation of a similar extent. We attribute the spatial dependence again to the second pass in the amplifier, where the pump pulse is not relay-imaged onto the BBO crystal. This can only be fixed by a new design of the NOPCPA (a substantial redesign is needed, because of the relay imaging and timing constraints).

5.3 Conclusions

In conclusion, we have demonstrated phase- and intensity-stable double-pulse parametric amplification at the millijoule level. To measure the phase stability we employed a sensitive interferometric technique, capable of detecting single shot phase differences smaller than 10 mrad. The investigated NOPCPA laser system induces a phase shift up to $\approx \pm 200$ mrad, depending on the operating conditions with a typical stability of 20 mrad rms over 2 minutes. The change of the phase shift during a day and between different sections of the beam typically lies within a range of 100 mrad. Because this can be monitored on line, the phase relation between the pulses is always well known.

The precision of the relative phase shift determination presented here is high enough for obtaining MHz-scale accuracy in the XUV (e.g. at the He 1s-4p transition at 52 nm or the 15^{th} harmonic of the 780 nm). Nonlinear phase shifts in optics and the harmonic upconversion itself are of concern for such an experiment. However the observed high relative intensity stability of the two output pulses gives good prospects for high resolution Ramsey spectroscopy in the XUV.

Chapter 6

XUV frequency comb metrology on the ground state of helium

In this chapter the operation of a frequency comb at extreme ultraviolet (XUV) wavelengths based on pair-wise amplification and nonlinear upconversion to the 15^{th} harmonic of pulses from a frequency comb laser in the near-infrared range is reported. It is experimentally demonstrated that the resulting spectrum at 51 nm is fully phase coherent and can be applied to precision metrology. The pulses are used in a scheme of direct-frequency-comb excitation of helium atoms from the ground state to the $1s4p$ and $1s5p$ $^1\mathrm{P}_1$ states. Laser ionization by auxiliary 1064 nm pulses is used to detect the excited state population, resulting in a cosine-like signal as a function of the repetition rate of the frequency comb with a modulation contrast of up to 55%. Analysis of the visibility of this comb structure, thereby using the helium atom as a precision phase ruler, yields an estimated timing jitter between the two upconverted comb laser pulses of 50 attoseconds, which is equivalent to a phase jitter of 0.38(6) cycles in the XUV at 51 nm. This sets a quantitative figure of merit for the operation of the XUV comb, and indicates that extension to even shorter wavelengths should be feasible. The helium metrology investigation results in transition frequencies of 5740806993(10) MHz and 5814248672(6) MHz for excitation of the $1s4p$ and $1s5p$ $^1\mathrm{P}_1$ states, respectively. This constitutes the first absolute frequency measurement in the XUV, attaining unprecedented accuracy in this windowless part of the electromagnetic spectrum. From the measured transition frequencies an eight-fold improved ^{4}He ionization energy of 5945204212(6) MHz is derived. Also a new value for the ^{4}He ground state Lamb shift is found of 41247(6) MHz. This experimental value is in agreement with recent theoretical calculations up to order $m\alpha^6$ and $m^2/M\alpha^5$, but with a six times higher precision, therewith providing a stringent test of quantum electrodynamics in bound two-electron systems.

Introduction

Atomic spectroscopy has been paramount for the discovery of the laws of physics. The ordering of spectral lines in the hydrogen atom has led to the Rydberg formula and the concept of quantization in the old Bohr model led eventually to the formulation of quantum mechanics. In 1947 further advance was made with the observation by Lamb and Retherford that the $2^2S_{1/2}$ and $2^2P_{1/2}$ states in hydrogen are not degenerate, but differ by 1 GHz [35, 1]. This result lead to the development of quantum electrodynamics (QED) [2, 3, 4], which is the most precisely tested physics theory to date. Since the first measurement by Lamb and Retherford, QED contributions to energy levels in atoms are referred to as “Lamb shifts”. The theory has been elaborately tested and confirmed by experiments in various bound systems, ranging from atomic hydrogen [111, 112], via one-electron heavy-ion systems [113], exotic atomic systems such as positronium [114] and muonium [115] to one-electron molecular ions [116, 117], while recently a test of the QED has also been reported in a neutral molecule [118]. Tests have also been performed on the anomalous magnetic dipole moment of the electron (“g-2"), so that in fact QED can now be used to derive a new value for the fine structure constant from such a measurement [119].

The two main QED contributions to the energy of an atomic system are virtual photon interactions ("self energy") and screening of the nuclear charge due to the creation (and annihilation) of electron-positron pairs ("vacuum polarization"). The magnitude of these effects depends on the considered system and its energy eigenstate, and is studied by means of precision spectroscopy. In atoms such as hydrogen and helium, the strongest QED effects are observed in the electronic ground states. For this reason spectroscopy involving the ground state is preferred. In the case of hydrogen this is achieved by inducing a two-photon transition at 2×243 nm from the 1S ground state to the 2S excited state, which has reached a level of precision that allows a detailed comparison between theory and experiment [6]. This comparison is currently limited by the uncertainty in the measured proton charge radius [120, 6, 121], which in itself is not a QED phenomenon. Assuming that the QED calculations are correct, one can also use the $1S - 2S$ experiment in hydrogen to determine the effective proton charge radius. In this respect it is in-

teresting to note that a recent experiment with muonic hydrogen (where the electron in hydrogen is replaced by a muon), has resulted in a proton size that differs 5σ [121] with the CODATA value that is based mainly on hydrogen spectroscopy. The origin of this difference is still under debate [122, 123, 124, 125].

In principle a more stringent test of QED could be performed by experiments using atoms with a higher nuclear charge Z, as the non-trivial QED effects scale with Z^4 and higher. For this reason experiments have been performed on many different high-Z ionic species such as U^{91+} [113]. However, the required (very) short wavelengths for excitation, such as hard-X-rays, make it very difficult to perform absolute frequency measurements (see e.g. [126] and references therein).

Even for $Z = 2$ in the He^+ ion or the neutral helium atom, where QED effects are at least 16 times larger than in hydrogen, it remains difficult to perform high resolution spectroscopy. In the case of He^+ a two-photon excitation from the ground state requires 60 nm, while for neutral helium 120 nm is required to drive the $1s^2\ ^1S_0 - 1s2s\ ^1S_0$ two-photon transition. One-photon transitions require even shorter wavelengths, in the extreme ultraviolet (XUV), e.g. 58 nm to excite the $1s^2\ ^1S_0 - 1s2p\ ^1P_1$ first resonance line in neutral helium.

A major obstacle to precision spectroscopy in the XUV is the lack of continuous wave (CW) narrow bandwidth laser radiation. Instead pulsed-laser techniques have been used. The first laser-based measurement of the $1s^2\ ^1S_0 - 1s2p\ ^1P_1$ resonance line at 58.4 nm was achieved via upconversion of the output of a grating-based pulsed dye laser [127]. Subsequently, pulsed amplification of CW lasers and harmonic generation in crystals and gases led to the production of narrower bandwidth XUV radiation. In this fashion spectroscopy on neutral helium has been performed from the ground state using ns-timescale *single* pulses of 58.4 nm [40, 128]. In an alternative scheme two-photon laser excitation of neutral helium at 120 nm was achieved [41, 129]. In both experiments transient effects resulted in "frequency chirping" of the generated XUV pulses, which limited the accuracy of the spectroscopy to about 50 MHz.

Here we overcome this problem by exciting transitions using a *pair* of phase coherent XUV pulses, produced by amplification and high-harmonic generation (HHG) of pulses from a frequency comb laser. In such a scheme most of the nonlinear phase shifts and those due to short-

lived transients cancel as only differential pulse distortions enter the spectroscopic signal. In effect, a frequency comb in the XUV is generated. The employed method of spectroscopy with this XUV comb laser is a form of Ramsey spectroscopy [67]. Early experiments using phase-coherent pulse excitation in the visible part of the spectrum used a delay line [130], a resonator [131] or modelocked lasers [64] to create two or more phase-coherent pulses. More recently, amplified ultrafast pulses have been split using a Michelson interferometer or other optical means to create two coherent XUV pulses after HHG [132, 133, 134]. Coherent excitation of argon in the XUV with a delay of up to ≈100 ps [135] has been demonstrated in this manner. However, with these methods no absolute calibration in the XUV has been demonstrated up to now as it is very difficult to calibrate the time delay and phase difference between the pulses with sufficient accuracy. In the present experiment we use a frequency comb laser (FCL) [60, 10] to obtain phase-coherent pulses in the XUV which allows for a much higher resolution and immediate absolute calibration.

Single femtosecond laser pulses can be made sufficiently intense for convenient upconversion to XUV or even soft x-ray frequencies using HHG [136]. However, as a consequence of the Fourier principle, the spectral bandwidth of such pulses is so large that it inhibits high spectral resolution. Frequency combs combine high resolution with high peak power by generating a continuous *train* of femtosecond pulses. In this case the spectrum of the pulse train exhibits narrow spectral components (modes) within the spectral envelope determined by the spectrum of a single pulse. The modes are equally spaced in frequency at positions given by:

$$f_n = n f_{rep} + f_{CEO} \tag{6.1}$$

were n denotes the integer mode number, f_{rep} is the repetition frequency of the pulses, and f_{CEO} is the carrier-envelope offset frequency. The latter relates to the pulse-to-pulse phase shift $\Delta\phi_{CE}$ between the carrier wave and the pulse envelope (carrier-envelope phase or CEP) by

$$\Delta\phi_{CE} = 2\pi f_{CEO}/f_{rep}. \tag{6.2}$$

Each of the comb modes can be used as a high-resolution probe almost as if it originated from a continuous single-frequency laser [137, 138, 139].

If the entire pulse train can be phase coherently upconverted, the generated harmonics of the central laser frequency should exhibit a similar spectrum with comb frequencies $mf_{rep} + qf_{CEO}$, where m denotes again an integer mode number, and q is the integer harmonic order under consideration. By amplification of a few pulses from the train, and producing low harmonics in crystals and gases, an upconverted comb structure has been demonstrated down to 125 nm [19, 20]. However, to reach wavelengths below 120 nm, HHG has to be employed requiring nonlinear interaction at higher intensities in the non-perturbative regime [79]. It is well established that HHG can be phase coherent to some degree [132, 133, 108, 79, 140, 135], and attempts have been made to generate frequency combs based on upconversion of all pulses at full repetition rate [16, 17, 141, 18]. However, due to the low XUV-pulse energies the comb structure could so far not be verified in the XUV-domain for those sources. That limitation can be overcome by combining parametric amplification of two frequency comb pulses in combination with harmonic upconversion. This was recently demonstrated with direct frequency comb excitation at 51 nm in helium [21], and in this paper a full and detailed description of that experiment is given.

The article is organized as follows: in section II the measurement principle is explained, followed in section III with a description of the different parts of the experimental setup. The general measurement procedure and results are presented in section IV. In section V, part A, a discussion of all systematic effects that need to be taken into account to determine the ground state ionization potential from the measured transitions frequencies is given. This is followed in part B with a discussion of the timing jitter in the XUV, which can be derived from the measured Ramsey signal. In the final section VI the conclusions and an outlook are presented.

6.1 Overview and principle of XUV comb generation and excitation

A frequency comb is normally based on a modelocked laser producing an infinite train of pulses with fixed repetition rate and CEP-slip between consecutive pulses. The corresponding spectrum of such a pulse train

consists of a comb of narrow optical modes associated with frequencies given by Eq. 6.1. To convert the frequency comb to the XUV, we select only two pulses from the FCL. In this case the spectrum changes to a cosine-modulated continuum, but with the peaks of the modulation exactly at the positions of the original FCL spectrum. This “broad frequency comb" is converted in a phase-coherent manner to the XUV by amplification of the pulse pair to the millijoule level, and subsequent HHG. Once the FCL pulses (separated by the time $T = 1/f_{rep}$) are upconverted, they can be used to directly probe transitions in atoms or molecules. This form of excitation with two pulses resembles an optical (XUV) version of the Ramsey method of spatially (and temporally) separated oscillatory fields [67, 19]. In the present case, the interacting fields are not separated in space, but only in time. Excitation with two (nearly) identical pulses produces a signal which is cosine-modulated according to:

$$S(T) \propto cos(2\pi(f_{tr}T) - \Delta\phi(f_{tr})) \tag{6.3}$$

when varying T through adjustment of f_{rep} of the comb laser. In this expression f_{tr} is the transition frequency and $\Delta\phi(f_{tr})$ is the spectral phase difference at the transition frequency between the two pulses. Relation (6.3) is valid only for weak interaction, which is the case in the current experiment given an excitation probability of $\ll 1$ per atom.

Without HHG and in the absence of additional pulse distortions the phase shift $\Delta\phi := \Delta\phi(f_{tr})$ is equal to $\Delta\phi_{CE}$. The excitation signal will exhibit maxima corresponding to those frequencies where the modes of the original comb laser come into resonance with the transition.

The spectral phase difference of the generated XUV pulse pair cannot be determined directly. Therefore we need to propagate the spectral phase difference from the frequency comb through the parametric amplifier and the HHG process into the interaction region. The phase shift $\Delta\psi(f)$ imprinted on the pulses by the non-collinear optical parametric double-pulse amplifier (NOPCPA) is measured direcly using an interferometric technique described previously [142]. To model the HHG process we employ a slowly varying envelope approximation described in section 6.4, which yields a differential XUV phase shift of the form

$$\Delta\phi_q = q(\Delta\phi_{CE} + \overline{\Delta\psi}) + \Delta\psi_q, \tag{6.4}$$

where $\overline{\Delta\psi}$ denotes the carrier envelope phase accumulated in the NOPCPA (compare Sec. 6.3), q is the harmonic order of the resonant radiation and $\Delta\psi_q$ is an additional phase shift due to nonlinear and transient response in the HHG process [80, 87] and transient effects such as ionization. Note that only differences in phase distortion between the two subsequent pulses from the FCL affect $\Delta\phi_q$ and therefore the Ramsey signal. Shared distortions, such as frequency chirping due to uncompensated time-independent dispersion, have no influence on the outcome of this experiment.

The frequency accuracy of the method scales with the period of the modulation (f_{rep}, here equal to $100-185$ MHz) rather than the spectral width of the individual pulses (about 7 THz in the XUV at the 15^{th} harmonic). An error δ in the value of $\Delta\phi_q$ leads to a frequency error in the spectroscopy result of $\Delta f = \delta/(2\pi T)$. Of the two components contributing to this error, $\Delta\psi(f)$ can be expected to be independent of T, while the transients contained in $\Delta\psi_q$ decay with increasing T. Therefore Δf decreases at least with $1/T$, leading to a higher accuracy for a longer time separation between the pulses. In practice there is still a minimum requirement on the stability and measurement accuracy of phase shift of rms 1/200th of a cycle (at the fundamental frequency of the FCL in the near infrared). This ensures that the contribution $\overline{\delta\psi}$ to the frequency uncertainty of the measured transition frequency is small enough so that the 'mode number' ambiguity in the transition frequency, due to the periodicity of the signal, can be resolved with confidence.

A sketch of the XUV comb principle in the frequency domain is shown in Fig. 6.1. A FCL serves as a source of phase-coherent pulses. A pair of such pulses is amplified in a NOPCPA to the mJ level, yielding a cosine modulated spectrum when viewed in the frequency domain. The amplified pulses are filtered spatially with two pinholes, one placed between the second and third amplification stage, and one after compression respectively. As a result the pulse pairs show less spatial intensity and phase variation compared to the unfiltered beam.

Before the IR beam is focused in a krypton jet for HHG, the center of it is blocked by a 1.9 mm diameter copper disk, while the outside is clipped with an iris. The donut-mode shape is used to facilitate the separation of the driving IR field from the generated XUV emitted on axis (see also section 6.2).

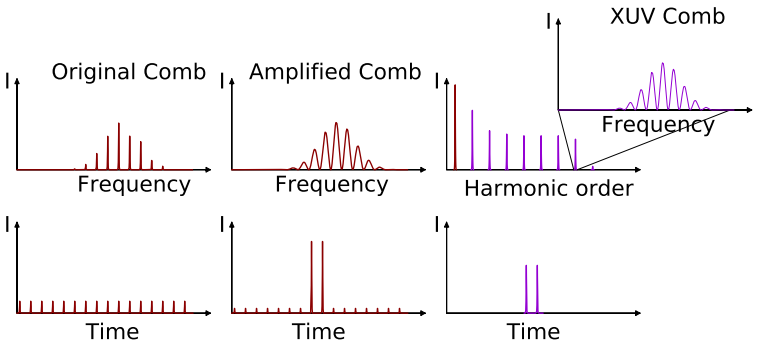

Figure 6.1: Principle of frequency comb generation and spectroscopy in the XUV. (a) Schematic of the spectral and temporal structure of the generated light at the different stages in the experiment (left to right): sharp equidistant frequencies from the infrared FC laser, followed by double-pulse amplification resulting in a cosine modulated spectrum, and finally HHG resulting in odd harmonics of the central frequency, where each of the harmonics consist of a XUV comb in the form of a cosine-modulated spectrum with period f_{rep}.

Phase shifts in the NOPCPA, which are not common for both pulses, and therefore change the position of the comb modes, are measured by means of spectral interference. A Mach-Zehnder-like configuration is used to interfere the original comb pulses with those that are amplified by the NOPCPA, as described in [142] and section 6.2.

The amplified pulses are focused a few mm in front of a krypton jet, in which two phase-locked pulses of high-order harmonics are generated to create a cosine-modulated comb spectrum in the XUV. In order to avoid direct ionization of helium with higher-order harmonics, the IR intensity in the interaction region and the harmonic medium are chosen such that the desired 15^{th} harmonic appears at the cutoff of the HHG process. The XUV beam crosses a low-divergence beam of helium atoms perpendicularly, and excites them from the ground state to the $1snp\ ^1\mathrm{P}_1$ state ($n \in \{4, 5\}$). A pulse of 1064 nm radiation ionizes the excited atoms, which are subsequently detected in a time-of-flight mass spectrometer. Tuning of the XUV comb is accomplished by changing f_{rep} of the FCL. The changing mode separation effectively causes the modes in the XUV to scan over the transition. An example for a scan of the repetition time corresponding to approximately 500 attoseconds (as) is shown in Fig. 6.2. The number m of the mode that excites the measured transition in this

experiment is in the order of 50 million. This means that the repetition rate of the fundamental FCL needs to be changed only by a few Hz in order to bring an adjacent XUV-mode $f_{m\pm1}$ into resonance with a helium transition (f_m is assumed to be at the transition initially). As a consequence the ionization signal will be cosine modulated. In order to resolve the resulting ambiguity in the mode-number assignment, the measurement is repeated with different repetition rates, corresponding to pulse delays between 5.4 ns and 10 ns.

Besides the frequency-domain perspective, this experiment can be viewed also in the time domain. In this case it can be seen as a pump-probe experiment, which tracks the dynamics of the electronic wave function that results from mixing the ground state of helium with the excited p-level. The first XUV pulse brings the atom into a superposition of the ground and the excited state. This superposition results in a dipole, which oscillates at the transition frequency with an amplitude that decays according to the lifetime of the excited state. The second pulse probes this oscillation. Two extreme cases can be distinguished. If the second pulse is in phase with the dipole oscillation, the amplitude of the excited state increases, and thus its detection probability. If the phase of the second pulse is shifted by π with respect to the dipole oscillation of the helium atom, its oscillatory movement is suppressed and the probability to find an atom in the excited state is decreased.

6.2 Experimental setup

The measurement setup consists of four major elements: a frequency comb laser, a non-collinear parametric amplifier, a phase-measurement system, and a vacuum apparatus for HHG and excitation of helium in an atomic beam. A schematic overview of the setup is given in Fig. 6.3.

Frequency-comb oscillator and pulse stretcher

Phase-coherent pulses are obtained from a home-built Kerr-lens mode-locked Ti:Sapphire frequency comb laser. The FCL has an adjustable repetition rate between 100 MHz and 185 MHz. Dispersion compensation in the cavity is obtained with a set of chirped mirrors, supporting a spectral bandwidth of 60 nm centered around 780 nm. The FCL is sta-

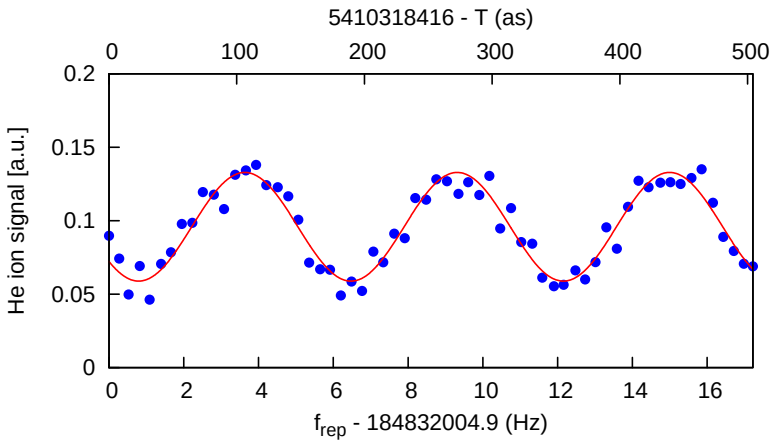

Figure 6.2: The excitation probability of helium at 51.5 nm on the $1s^2\ {}^1\mathrm{S}_0 - 1s5p\ {}^1\mathrm{P}_1$ transition, as a function of the repetition of the frequency comb laser (lower x-axis), and the delay between the pulses (upper x-axis in attoseconds). In this example f_{CEO} is locked 46.21 MHz, and a 1:5 He:Ne mixture is used for the atomic beam.

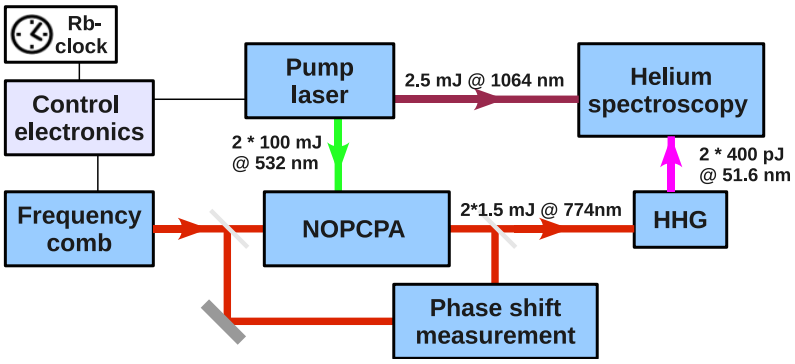

Figure 6.3: Scheme of the experimental setup, including: femtosecond frequency comb laser with control electronics, non-collinear optical parametric chirped-pulse amplifier (NOPCPA), a phase measurement in a Mach-Zehnder interferometer, high harmonic generation (HHG) and a spectroscopy apparatus. Part of the pump laser output at 1064 nm is used as ionization beam.

bilized and calibrated against the signal of a rubidium clock (Stanford research PRS10), which itself is referenced to a GPS receiver so that an accuracy on the order of 10^{-11} is reached after a few seconds of averaging. Before sending the FCL pulses to the amplifier, the wavelength and bandwidth of the comb pulses is adjusted with a movable slit in the Fourier plane of a grating-based $4-f$ stretcher (1200 l/mm, $f = 10$ cm). The bandwidth is set to 6 nm in this device, ensuring that after upconversion to the XUV only one state in helium is excited at a time. The spectral clipping and losses from the gratings in the stretcher reduce the pulse energy from about 5 nJ to 60 pJ. At the same time the added dispersion and reduced bandwidth lengthens the pulse to about 2 ps.

Non-collinear optical parametric amplifier

A pair of subsequent pulses obtained from the stretcher is amplified in a non-collinear optical parametric chirped-pulse amplifier based on two 5 mm long BBO (beta-barium borate) crystals. Here we present a concise description of the system, while further details can be found in [142, 89]. The amplifier operates at a repetition rate of 28 Hz, and amplifies two subsequent FC pulses to a level of typically 5 mJ each. The bandwidth of the pulses remains essentially unchanged compared to that selected by the slit of the preceding stretcher, although saturation effects in the NOPCPA result in a 'cathedral'-like spectrum (see Fig. 6.4). The pump light for the NOPCPA (two pulses at 532 nm, 50 ps, $80 - 100$ mJ per pulse) is obtained by frequency doubling 1064 nm light from a Nd:YAG-based pump laser. A relay-imaged delay line in the pump laser is used to produce these pulse pairs with a time separation between 5.5 ns and 10 ns. This time separation is adjusted carefully for each value of f_{rep} to match the time delay between consecutive pulses from the FC laser at a few-ps level.

Electronic synchronization is employed (timing jitter less than 1 ps) so that the pump and comb laser pulses arrive at the BBO crystals at the same time. The amplification happens in three stages, the first two located in the first BBO crystal and the last (power amplifier) stage uses the second. Between the first and second crystal spatial filtering is used to reduce phase-front errors. After amplification in the NOPCPA, and subsequent compression, a final spatial filter is employed (based on a 1:1

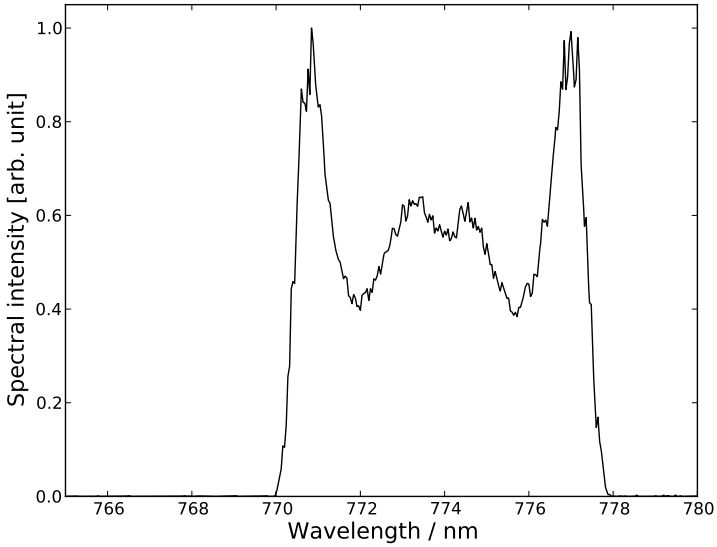

Figure 6.4: A typical spectrum of the pulse-pair after NOPCPA, acquired with a resolution of 0.1 nm measured by an Ando AQ-6315A optical spectrum analyzer.

telescope with $f = 50$ cm lenses and an 80 micron pinhole in between, mounted in vacuum). This reduces wave-front errors and results in a Gaussian beam with a diameter of 6 mm. The pulses of 300 fs duration are essentially diffraction and Fourier-limited with an energy of $1-2$ mJ per pulse.

By choosing parametric amplification, a high gain (10^8) is achieved while avoiding some of the transient effects that conventional laser amplifiers suffer from, such as thermal lensing and inversion depletion. The reason for this is that in NOPCPA negligible power is dissipated in the amplifier medium (a nonlinear crystal), and that the amplified ('signal') wave is not distorted provided the process is perfectly phase matched (see e.g. [91]). Imperfections of the wave front of the pump-beam pulses can lead to a spatially-dependent phase mismatch in the NOPCPA, which in turn influences the phase of the amplified signal beam. Therefore special attention is paid to match the properties (wave front, pulse length, energy, diameter) of the two pump pulses so that induced phase effects in the two amplified signal pulses are as equal as possible. A Shack-

Hartmann sensor was used to align their direction within several μrad and their propagation axis within 10 μm. The remaining spatial differential signal distortions are reduced by the spatial filters and finally measured interferometrically as described in the next section.

Phase-shift measurements in the IR

Knowledge of the carrier-envelope phase change between consecutive pulses of a repetition-frequency stabilized mode-locked laser is a prerequisite for frequency-comb metrology. Because parametric amplification influences the phase of the amplified light [72, 73], a method is needed to detect a differential phase shift between the pulses. This shift is recorded for each laser shot, using spectral interferometry with the original comb pulses as a reference in a Mach-Zehnder configuration (Fig. 6.3).

The phase-measurement setup is an advanced version of the one published earlier [142]. In order to deal with the demand for higher spectral resolution of the phase-measurement setup and the spatial dependence of the phase shift between the pulses, several improvements were made. The most important is a motorized iris (diameter: 2 mm), which enables spatial mapping of the differential phase within 30 seconds, by scanning it along the donut mode (see also section 6.2). Such a wave-front scan is made before every recording of the helium signal as it cannot be done for every individual laser shot while measuring the helium signal. However, during a recording of the helium signal the iris is opened and an average value for the shift of $\Delta\phi_q$ is monitored for each laser shot. This average is compared with the wave-front scan made just before a recording of the helium signal from which a correction for the average phase shift is calculated. In this way the effective phase difference change can be continuously monitored. The differential phase distortion along the donut-mode profile has a typical magnitude of 100 mrad, and a spatial variation of $20 - 30$ mrad.

Perfect spatial overlap between the amplified and reference pulses is ensured by sending both beams through a 2 meter long large-mode volume (field diameter 20 μm) single-mode photonic fiber. Before doing so, the pulses are stretched approximately 40 times in a grating stretcher. The combination ensures that both amplified and reference beam are perfectly overlapped, while the stretching and the large mode volume of

the fiber enables to increase the pulse energy for good signal-to-noise ratio without inducing self-phase modulation (SPM) in the fiber. This last aspect is particularly important because otherwise intensity differences between the pulses could induce SPM and corrupt the result of the phase shift determination.

High harmonic generation

The central part of the amplified and spatially filtered beam is blocked by a 1.9 mm diameter copper disk to facilitate separation of the fundamental IR light and generated XUV further downstream. High harmonics are produced by focusing this donut-shaped beam ($f = 500$ mm) a few mm in front of a pulsed krypton gas jet. The intensity at the focus is estimated to be less than 5×10^{13} W/cm^2, while the local gas density is estimated at a few mbar. After the focus the beam encounters an iris of 0.8 mm diameter at 40 cm distance from the jet, which is placed in the image plane of the copper disk. The iris blocks the infrared radiation with an extinction of better than $1 : 27$, while the XUV light emitted on axis can freely propagate. Thereafter the XUV beam passes the interaction chamber (described below), and enters a normal-incidence focusing grating monochromator equipped with an electron multiplier to analyze the harmonic spectrum. We estimate that about 1×10^8 photons at the 15^{th} harmonic at 51.5 nm are generated per laser shot. The driving intensity is chosen on purpose at such a level that the 15^{th} harmonic is positioned exactly at the cut-off of the HHG process. As a result the next harmonic (the 17^{th}, causing background counts due to direct ionization of helium atoms in the spectroscopy experiment downstream) is about 10 times weaker.

Spectroscopy chamber

In the interaction chamber the XUV double pulse intersects a low-divergence beam of helium atoms at perpendicular angle to avoid a Doppler shift. The atomic beam is generated using a pulsed valve (General Valve, backing pressure 3 bar) producing a supersonic expansion with either pure helium or a mixture with a noble gas (ratio 1 He : 5 NG). By seeding in Kr, Ar and Ne the helium velocity can be varied over a factor of 4 to investigate Doppler effects. The divergence of the

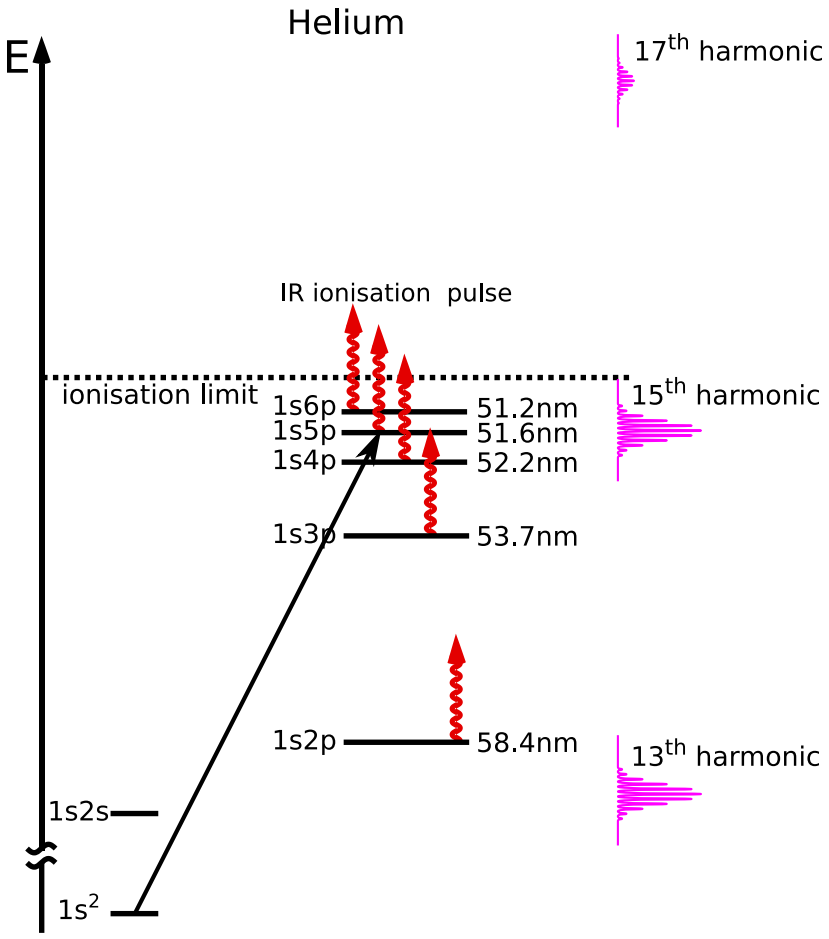

Figure 6.5: The XUV comb drives transitions from the $1s^2\ ^1\mathrm{S}_0$ to the $1snp\ ^1\mathrm{P}_1$ states with the 15^{th} harmonic, and excites the continuum with the 17^{th} and higher harmonics. The excited state population of the $1s4p$ state and above is selectively ionized using 1064 nm radiation. Compared to this schematic, the harmonics are in reality narrower, and contain many more modes (about 50000).

atomic beam is limited to approximately $3-4$ mrad by two skimmers: one circular skimmer of 0.3 mm diameter and one adjustable slit skimmer of 0.25 mm width to set the XUV-He beam angle. This divergence is similar to the divergence of the XUV beam (<2 mrad). Directly after interaction with the XUV-pulse pair the excited state population is detected by state-selective ionization (see Fig. 6.5) with a 50 ps pulse at

1064 nm. The resulting helium ions are detected in a time-of-flight mass spectrometer.

6.3 Frequency metrology on $1s^2 - 1s4p$ and $1s^2 - 1s5p$ transitions in helium

The generated XUV comb has been used to measure the $1s^2 - 1s4p$ and $1s^2 - 1s5p$ transition frequencies, from which an improved value for the helium ground state binding energy is derived. Because this involves tests of many systematic effects, a hierarchy of measurements can be identified (see table 6.1). The first level is that of a single recording of the helium signal as a function of the repetition rate of the frequency comb laser in the IR. To record the helium signal, the infrared FC-laser repetition frequency is scanned in steps of less than 20 mHz, resulting in changes in the time separation between the two pulses of around 1 attosecond. Each scan requires recording of $20000 - 30000$ laser pulses, which takes about 15 minutes. For each laser shot, we record the ion signal, together with a series of other parameters, which are the frequency comb repetition frequency f_{rep} and offset frequency f_{CEO}, the individual IR-pulse energies, energy E_{XUV} of both XUV pulses and the average amplifier phase shift. The records are then binned into typically 20 groups over a Ramsey period, based on a scaled coordinate u defined as

$$u := [q(f_{CEO} + \frac{\overline{\Delta\psi}}{2\pi} f_{rep}) - f_{th}]/f_{rep} \tag{6.5}$$

where q is the harmonic order ($q = 15$), f_{th} is the theoretically predicted transition frequency, and $\overline{\Delta\psi}$ is the phase shift at the peak of the envelope, which is calculated from the phase measurement and additional corrections (see section 6.4). We calculate the excitation probabilities $p(u)$ per laser shot, and averages of the other measured parameters within each bin, denoted by bars over the respective symbol from here on. The measured transition frequency $f_{tf} = f_{th} + f_{ex}$, average background p_0, and Ramsey-fringe amplitude A are then fitting parameters in the following model:

$$p(u) = \Big(p_0 + A\cos 2\pi[u + f_{ex}/\overline{f_{rep}}(u)]\Big)/\overline{E_{XUV}(u)} \tag{6.6}$$

This results in a transition frequency f_{ex} for a single scan, relative to the theoretical transition frequency f_{th}. The statistical error in this fit is determined via a bootstrap method [105], which requires no model of the noise sources.

The theoretical transition frequencies f_{th}, used in the fitting procedure as a reference to which the experimental value is determined, are obtained by combining recent values of the theoretical ground state energy from the literature [28] with those of the excited states [143]. Predicted theoretical frequencies are 5740806963(36) MHz for the $1s^2\ ^1\mathrm{S}_0 - 1s4p\ ^1\mathrm{P}_1$ and 5814248632(36) MHz for the $1s^2\ ^1\mathrm{S}_0 - 1s5p\ ^1\mathrm{P}_1$ transitions.

In Fig. 6.2 a typical recording of the excitation of helium by scanning the XUV comb over the $1s^2\ ^1\mathrm{S}_0 - 1s5p\ ^1\mathrm{P}_1$ transition is shown. The contrast of the modulation (in this example 40%) is smaller than unity due to various effects, like Doppler broadening, frequency noise and a finite constant background of about 15% due to direct ionization with the 17^{th} and higher harmonics. Fitting of a single recording typically shows a statistical error of 1/50th of a modulation period. Depending on the repetition rate it amounts to an uncertainty of $2 - 3$ MHz, which is unprecedented in the XUV spectral region.

Several scans are then performed while changing one parameter in the setup (e.g. helium velocity) to determine the magnitude of systematic effects. Such a measurement sequence is referred to as a "series" in the following. The two most frequently performed tests (series) determine the Doppler shift (by changing the helium velocity using gas mixtures) and ionization-induced frequency shift (by varying the density in the krypton jet). Less frequently the IR-pulse ratio was also varied to test its influence on the measured transition frequency. The analysis of these tests, as well as additional experiments that have been performed to determine other systematic errors, are described in more detail in section 6.4. Each of the series typically requires $4 - 6$ scans. From this data we extract (inter/extrapolate) the measured transition frequency in absence of the investigated effects and a coefficient for correcting the shifted values. For example, the extrapolation to zero velocity in a Doppler-shift measurement yields a Doppler-free frequency plus the slope, i.e. the angle between XUV and atomic beam. The angle can be used to correct the Doppler shift of scans at a finite known helium velocity. A 'session' then consist of a number $(2 - 15)$ of these series containing in total up to

60 scans. Within each session, groups of series are selected so that each group contains at least one Doppler measurement and one ionization-effect measurement. If possible, also a pulse-ratio-variation measurement is included, otherwise a default dependence is used based on previous measurements.

Figure 6.6 gives an example for a data set acquired in a measurement session. The different series are displayed therein as red circles for Doppler-shift measurements, green triangles for ionization-shift determinations and blue squares for the measurement of the shift related to the pulse-intensity ratio. Note, that some measurements are used to derive both the Doppler and the ionization-related contribution. These separate determinations are used to mutually correct each other for the different tested aspects (so e.g. an ionization-series value is corrected for the Doppler shift measured just before or after, and vice versa). The error bar on each series depends on the statistical error of its single recordings, and the fit of the systematic effect. After grouping, a sequence of transitions frequencies results with an appropriate error bar. Additional corrections (such as Stark shift, recoil shift) are then applied, and the theoretical value for the energy of the excited state is taken into account. The weighted average over these values then leads to a session-level value for the ground state binding energy and an error estimate for it.

Each session is performed for a combination of one upper state in helium (either $4p$ or $5p$), with one repetition rate of the frequency comb laser. Most recordings were made of the $1s^2\ {}^1\mathrm{S}_0 - 1s5p\ {}^1\mathrm{P}_1$ transition. As an additional check also one series was measured on the $1s^2\ {}^1\mathrm{S}_0 - 1s4p\ {}^1\mathrm{P}_1$ transition. A weighted average over all sessions then leads to a new value for the measured transition energies.

6.4 Discussion

The experiments discussed in this article yield a two-fold result. The phase coherence of the XUV-pulse pair allows to measure the frequency of an electronic transition in helium. In addition, the contrast of the Ramsey fringes, obtained for different repetition frequencies and helium velocities is used to investigate the coherence of the generated XUV radiation. Accordingly the following discussion is divided in two major

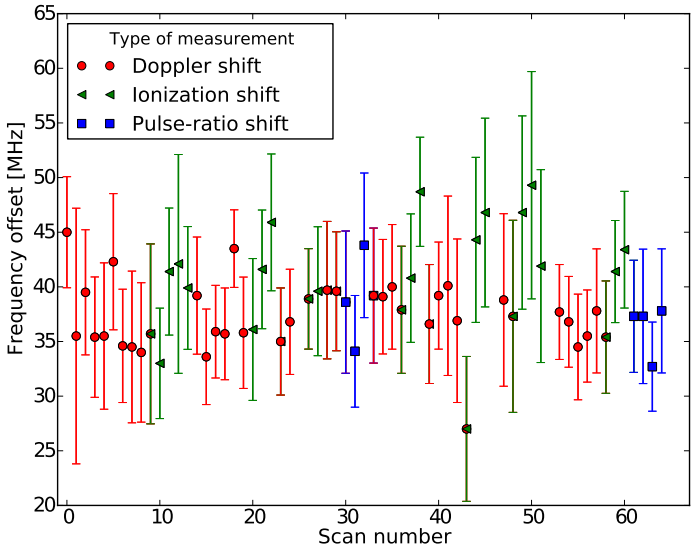

Figure 6.6: A measurement session performed on the $1s^2\ {}^1\mathrm{S}_0 - 1s5p\ {}^1\mathrm{P}_1$ transition in helium at $f_{rep} = 121$ MHz. The uncorrected frequency offset from theory f_{th} is displayed on the y-axis. The different shapes of the points indicate measurement series of systematic effects. Doppler-measurement series are shown as red circles, ionization shift measurement series with green triangles while the blue squares denote the measurement of pulse-intensity related effects.

parts: an evaluation of the measured transition frequencies and a contrast analysis of the observed interference signals.

Determination of the ground-state energy of helium with an XUV-frequency comb

For an absolute measurement many systematic effects have to be considered in addition to the already mentioned effects of Doppler shifts, phase shifts in the NOPCPA and in the HHG. These include recoil shifts, refractive index changes (Kerr effect) in the focusing lens for HHG and the entrance window to the vacuum setup, and the influence of the plasma generated in the HHG medium. Also AC and DC Stark effects and Zeeman shifts are considered. A new ionization energy for helium is derived from these measurements by taking the excited states ionization energy of the $4p$ and $5p$ into account. The binding energies of these states are

known to an accuracy better than 20 kHz from calculations [28, 143]. From the systematic studues an improved experimental value is then obtained; an error budget for this value is listed in Table 6.1

To remove the ambiguity due to the periodic comb spectrum, the energy of the ground state of helium is determined by measuring the frequency of $1s^2\ ^1\mathrm{S}_0 - 1s5p\ ^1\mathrm{P}_1$ transition at different repetition rates f_{rep} of the FCL between 100 and 185 MHz. Additionally, the frequency of the $1s^2\ ^1\mathrm{S}_0 - 1s4p\ ^1\mathrm{P}_1$ transition is measured at $f_{rep} = 148.5$ MHz as a crosscheck. The correct "mode number" is found by plotting the possible energies of the helium ground state against f_{rep} as shown in figure 6.11, (similarly as implemented in [19]).

Systematic phase and frequency shifts, which occur at different stages in the experiment (like phase shifts in the NOPCPA or HHG), are measured, investigated and corrected at different stages of data analysis. In this section the magnitude and treatment of individual systematic contributions to the measured frequency is discussed.

Many error sources lead to a frequency uncertainty that is a function of the delay between the pulses in a Ramsey pulse-pair. This can be a direct influence (by phase shifts), but also indirect (e.g. Doppler shift) because the fit accuracy depends on the contrast of the Ramsey interference pattern, which in turn depends e.g. on the repetition rate, helium velocity and decay rate vs. repetition time. We take these variations into account, providing not only an error, but also an error range estimate for several contributions (see Table 6.1).

Some of the considered error sources relate to differential phase shifts in the IR or XUV light field (e.g. a IR wavefront error or ionization shift), while other errors shift the measured frequency (e.g Doppler shift). For this reason the corrections and errors are given either in terms of a phase shift at the 15^{th} harmonic, or as a frequency shift. Phase shifts convert into different frequency shifts depending on the repetition rate of the frequency comb laser, while the frequency shifts are independent of f_{rep}.

In the following sections, we will discuss the effect of differential phase shifts in the amplifier, in the focusing lens and the entrance window into the HHG-chamber, and in the krypton jet in which the XUV is generated. Furthermore Doppler effects, AC and DC Stark shifts, Zeeman shift, recoil shift and the contribution to the signal from the adjacent $6p$-level

will be evaluated. The discussion is subdivided according to the different stages of error analysis following Table 6.1.

Single recording level errors

Unequal conditions experienced by the two laser pulses can shift their relative phase $\Delta\phi_{CE}$, and therefore the offset frequency f_{CEO} of the corresponding frequency comb. Because every imprecision in the carrier-envelope phase shift $\Delta\phi_{CE}$ between the IR pulses is multiplied by the harmonic order of the harmonic upconversion process, special care must be taken to determine the resulting phase shifts. The harmonic order of 15 employed in this experiment sets a high demand for the detection of differential phase shifts between the IR pulses. The setup used to measure the relative spatial-phase profile of the IR-pulse pair was described in section 6.2. Typical measured phase shifts are on the order of 100 mrad (both positive and negative, depending on the alignment of the pump laser and NOPCPA system). Therefore in the 15^{th} harmonic phase shifts on the order of 1.5 rad in the XUV at 51 nm are considered. The phase-shift variation across the spatial profile of the beam is typically $20-30$ mrad in the IR, which dominates the uncertainty in the propagation of the phase shift error to the XUV.

In a previous experiment [19] the effective influence of the measured differential spectral phase shift $\Delta\psi(f)$ was calculated by taking a simple equal weight average of all spectral components in the pulse. However, this is an oversimplified procedure. In order to propagate IR pulse distortions to the XUV we model the HHG process using a slowly-varying-envelope approximation, neglecting depletion of the HHG medium (consistent with our operating conditions). We can then write the (complex) generated electric field at the q^{th} harmonic

$$E_H(t) = f_H(A(t))e^{iq(\omega_0 t+\phi(t))} + c.c., \tag{6.7}$$

where $A(t)$ is the slowly varying (real) envelope, $\phi(t)$ the (chirp) phase of the pulse and f_H the (complex) single frequency response of the HHG medium. We take ω_0 to be the q^{th} subharmonic of the transition frequency ω_{tr}.

The phase shift between the driving laser field and generated XUV radiation depends on the IR intensity. On a single-atom level and in

the strong-field limit it can be described analytically [80]. This model contains several contributions to the harmonic yield. The most common of these are referred to as the 'long' and 'short' quantum trajectories which exhibit a different intensity-dependent linear phase. By selecting only the central part of the HHG emission we ensure that only those terms that show the smallest phase coefficient (the 'short' trajectory) contribute. The yield of the on-axis emission from the 'short' trajectory is optimized by placing the HHG medium slightly behind the focus of the IR fundamental beam. If we consider now the peak of the pulse, assume that only a single quantum trajectory contributes to the HHG field (as should be the case by design of the experiment) so that there is no net interference and therefore f_H has no oscillatory behaviour, and neglect phase matching (which should be fair in a sufficiently small region around the peak amplitude), we can model the response function by:

$$f_H(A) = \alpha A^n e^{i\beta A^2} \tag{6.8}$$

where α and β are amplitude and phase coefficients and n is an exponent characterizing the HHG conversion efficiency. The harmonic field of the second pulse with a (possibly) slightly distorted envelope $A^*(t) = A(t) + \delta A(t), \quad \phi^*(t) = \phi(t) + \delta\phi(t)$ is then given by

$$E_H^*(t) \approx \left(1 + \delta A \frac{f_H'(A)}{f_H(A)} + iq\delta\phi\right) f_H(A(t)) e^{iq(\omega_0 t + \phi(t))} + c.c. \tag{6.9}$$

so that the Fourier transform of the distorted pulse at the transition frequency (neglecting the rapidly oscillating counter-rotating component) reads

$$\widehat{E_H^*}(\omega_{tr}) \approx \int \mathrm{d}t \left[1 + n\frac{\delta A(t)}{A(t)} + i(2\beta A(t)\delta A(t) + q\delta\phi(t))\right] f_H(A(t)) e^{iq\phi(t)}. \tag{6.10}$$

By adjusting the intensity difference between the two pulses we attempt to make the δA terms vanish. Then the phase difference at the transition frequency between the pulses is given by the expression

$$\overline{\Delta\psi} = \arg\left(\frac{\widehat{E_H^*}(\omega_{tr})}{\widehat{E_H}(\omega_{tr})}\right) \approx \frac{\int \mathrm{d}t q\delta\phi(t) f_H(A(t)) e^{iq\phi(t)}}{\int \mathrm{d}t f_H(A(t)) e^{iq\phi(t)}}. \tag{6.11}$$

For Fourier-limited pulses ($\phi(t) = 0$) and real f_H (no intensity-induced phase effect in the HHG process) this would just be a weighted average

of $\delta\phi$ with $|f_H|$ as a weight function. However, since the IR pulse is near bandwidth limited and tuned close to the transition frequency, $\phi(t)$ can only vary a small fraction of unity during the pulse. Likewise, because we use a harmonic at the cutoff (the 15^{th}), the XUV yield has a single maximum of limited duration around the maximum of the IR pulse. During this time we can assume the nonlinear phase $exp(i\beta A^2)$ to be constant to first order (in t). Therefore the phase correction required at the transition frequency in the XUV is approximately equal to:

$$\overline{\Delta\psi} \approx \frac{\int \mathrm{d}t q\delta\phi(t)|f_H(A(t))|}{\int \mathrm{d}t|f_H(A(t))|}. \tag{6.12}$$

Due to the localization of the XUV emission, the weighting function $f_H(A(t)))$ could be replaced with any function that peaks, where the pulse does. This means that the effective phase shift in the XUV at the transition frequency can be approximated using phase information in the time domain as the XUV radiation is only generated when the IR pulse is close to its maximum intensity. We estimate $A(t)$ by assuming Fourier-limited IR pulses with the spectrum found by spectral interferometry. This should be a good approximation of the actual pulse shape in the experiment, as it leads to the highest XUV yield, and the pulse compressor was set to achieve this maximum XUV yield during the measurements. $\delta\phi(t)$ is calculated using the same assumption by just calculating the inverse Fourier transform of the two spectral-interferometry images. In a separate experiment we determined that the amount of XUV radiation at the 15^{th} harmonic depends on the IR intensity to the 9^{th} power, which has actually been used as the peaking weighting function for $\delta\phi(t)$. The temporally-averaged phase shift using the reconstructed XUV intensity and temporal phase shift results in a value of $\overline{\Delta\psi}$ for each laser shot. This is then used in the helium signal fitting procedure.

We analyzed our data using equal weight spectral averaging over the measured spectral phase as well. The resulting transition frequency coincides with our more accurate model to within 1 MHz. However, for the simple spectral average of the measured phase shift, the spread in the values for the series with different repetition rates of the comb laser is significantly larger, which confirms that weighted temporal averaging models the phase shift better.

To minimize the intensity-related frequency shifts from HHG in the spectroscopy, we take care that the energy in the driving pulses is on av-

erage equal within 5%. Together with the filtered beam profile and equal temporal profile, this ensures that the intensity in the focus is equal on the few percent level. To compensate for possible intensity differences we determined the observed transition frequency as a function of IR-pulse energy difference and interpolate linearly to zero difference. First the energies of the pulses are measured with a photo-diode. The integral of the photo-diode signal is recorded with an oscilloscope for each pulse and divided by the mean value. A value for the peak intensity of a pulse is obtained from the measured energy, using again the spectral data available in the interferograms recorded for the phase measurement. We typically find a frequency shift that, linearly extrapolated, corresponds to an IR phase shift smaller than 0.2 rad for 100% relative intensity variation, which is less than 3 rad at the 15^{th} harmonic. This interpolation also includes (and therefore minimizes) nonlinear phase shifts in the beam splitter, focusing lens and vacuum window, which are not included in the phase measurement using the Mach-Zehnder interferometer. Our relative intensity determination is accurate to within about 2% for small pulse energy differences, so that the error due to this determination can be estimated to be 60 mrad, corresponding to a frequency error of 1.5 MHz at 150 MHz repetition frequency in the XUV.

The "Amplifier phase" error in Table 6.1 combines the uncertainty of the phase measurement and wavefront deviation in the fundamental IR beam. The latter is calculated based on an average over the wavefront scan over the donut mode of the IR pulses. However, in principle there can be a systematic error for this effect at the level of a single helium signal recording, especially if the intensity profile is not perfectly homogeneous. In that case the average of the phase measured over the beam is not representative for the phase shift at the 15^{th} harmonic. To minimize this effect, we employ tight spatial filtering just before the phase-measurement setup to reduce wave-front errors and to smoothen the intensity profile to the lowest order Gaussian. During a session the pinhole we use for spatial filtering typically starts to wear out after a few hours of operation, leading to slightly asymmetric intensity distributions over time that vary randomly for each measurement session. The pinhole was also regularly replaced and realigned, as was the NOPCPA, so that the intensity and phase variations average down significantly over the near 200 scans that were analyzed. Therefore the error due to the

phase deviations and measurement accuracy is listed as a statistical error, conservatively based on the rms amplitude of the phase deviations as measured for each helium signal scan.

Measurement series level errors

Some of the systematic effects are related to the condition of the setup during the measurement. In particular transient and alignment-related effects are investigated alternately during a measurement session, forming series of measurements, which can be used to derive and mutually correct systematic shifts.

Transient phase shifts occur when the first pulse changes the propagation conditions for the second one. In this case the condition of equal pulses is not sufficient to avoid an additional phase shift. Transient shifts that occur within the Mach-Zehnder interferometer are readily detected and corrected for. This includes shifts that are caused in the optics after the NOPCPA.

The largest transient effect is due to ionization of the HHG medium. What matters is only the ionization between the two points in time where the 15^{th} harmonic is generated. Ionization leads to a lowering of the refractive index especially for the IR fundamental pulse, to the effect that the phase velocity of the second pulse becomes faster than that of the first pulse. Ionization is intimately linked to the HHG efficiency and therefore cannot be avoided completely. As we vary the IR intensity (by adjusting an iris size in the IR beam path) we find that at too high intensity, the second XUV pulse can be strongly suppressed due to ionization of the medium and resulting phase-mismatching effects induced by the first pulse. In order to keep the latter to a minimum, we operate at an intensity at which a reasonable XUV yield is obtained, while simultaneously keeping the XUV pulse-energy imbalance to within less than 20% (see Fig. 6.7). In order to determine the remaining effect due to ionization, we change the pressure in the HHG medium (by adjusting the valve driver), thereby varying the plasma density, and record the measured transition frequency effectively for different ion densities in the HHG medium.

The simultaneously measured XUV energy is used as a relative gauge for the density of ions in the HHG interaction zone, as no direct measure-

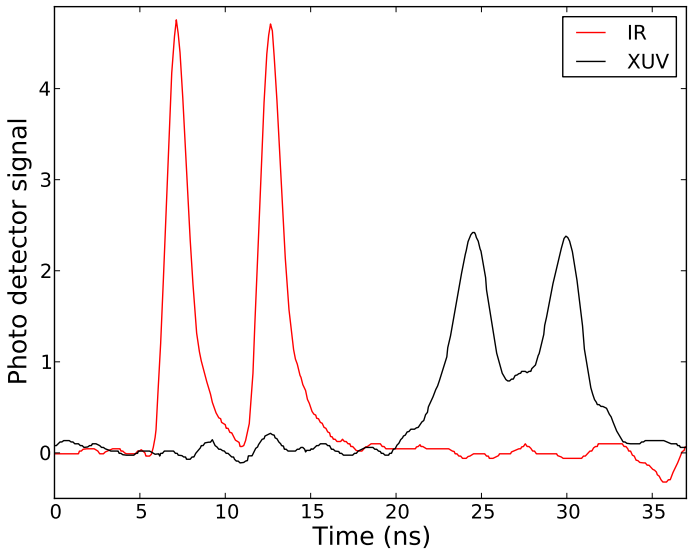

Figure 6.7: A typical example of the measured IR-pulse photo-detector signals (red) together with the corresponding XUV-yield at the 15^{th} harmonic (black).

ment of the level of ionization of the HHG medium was available for the helium measurements. If the phase matching conditions are not severely altered due to ionization, a quadratic dependence of the XUV output on krypton density is expected, while the plasma density, and therefore the phase shift, should be proportional to the density of krypton atoms. We assume that the induced plasma density is proportional to the krypton density, and that no recombination takes place on a timescale of 10 ns.

The relation between XUV yield and ion density was verified in a separate experiment by determining the amount of ionization in the HHG process using a collector grid just below the krypton jet. The voltage applied to this grid was on the order of a few volts to avoid secondary emission. For the conditions in the experiment the relation between XUV energy and recorded number of ions is equal to a power law with an exponent of 2.1(6), in good agreement with the expected 2.0.

To obtain the 'ionization free' frequency we extrapolate the frequency offset *vs.* XUV energy (when varying Kr density) to zero XUV energy using this experimentally determined exponent (see Fig. 6.8). From the extrapolations we typically find shifts between 0 and 2 rad at the 15^{th}

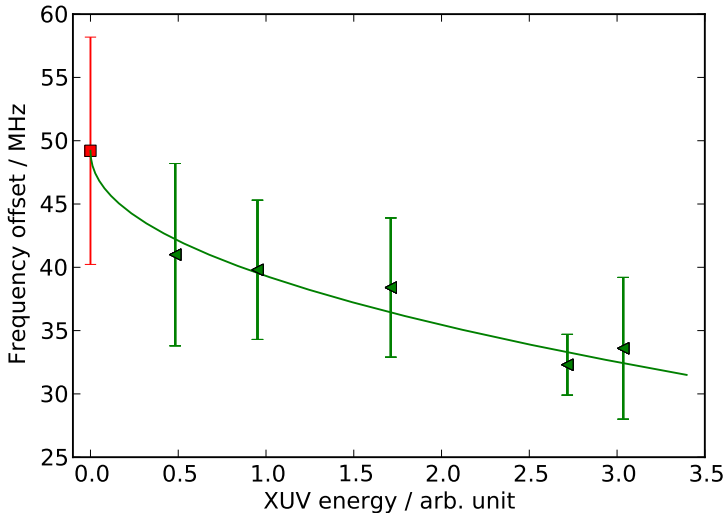

Figure 6.8: A typical measurement of the frequency offset f_{ex} (the experimental transition frequency relative to the theoretical reference value) as a function of the XUV energy. The XUV energy was varied by changing the gas density in the HHG jet. The green curve is the fitted dependence, while the red square indicates f_{ex} for zero gas density in HHG.

harmonic for standard conditions, with uncertainties in the range between 0.5 and 2.0 rad. The average correction is on the order of 0.1 XUV cycles. Figure 6.8 shows the fitting of a typical ionization measurement series, from which a value is derived for f_{ex} at zero gas density in the HHG jet and therefore at zero XUV intensity.

We also have considered krypton atoms in the HHG medium possibly left in an excited state after the first pulse. These excited state atoms would have a different nonlinear susceptibility and therefore produce a different nonlinear phase shift. Such a shift would not be detected by reducing the gas density. However, the HHG cutoff energy for such excited state atoms would lie far below the cutoff energy of the ground state atoms, as the first excited state is about 10 eV above the ground state. Because the cutoff is already set to the 15^{th} harmonic for ground state krypton, this radiation can not be produced by the excited Kr atoms.

The Doppler effect is monitored by varying the helium-beam velocity using mixtures with noble gases. The velocity of helium in the atomic

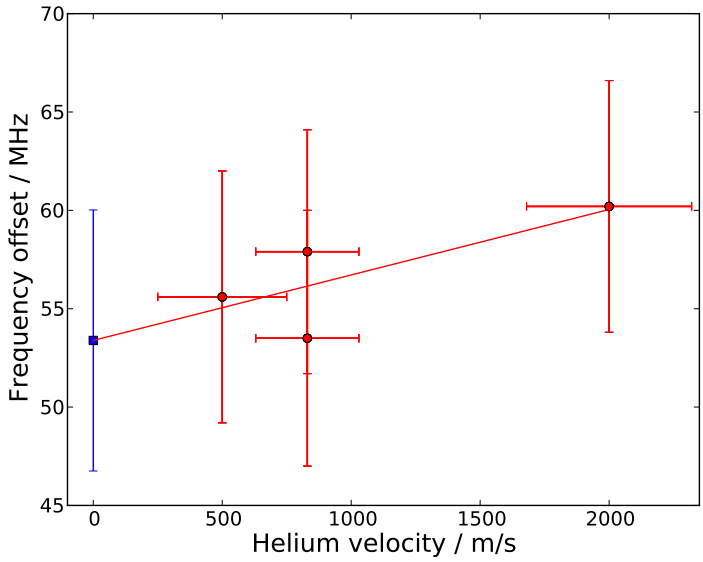

Figure 6.9: A typical measurement of the frequency offset f_{ex} with respect to the velocity of the helium atoms in the beam. The red line is the fitted dependence, the blue square is the extrapolated Doppler-shift free frequency for zero helium velocity.

beam is measured (in a separate experiment) by monitoring the frequency shift in the helium signal for different angles between atomic and XUV beam. Helium atoms in the pulsed atomic beam have a speed of 2000(320) m/s for a pure-helium expansion, helium in neon (pressure ratio 1:5) results in a speed of 830(200) m/s, and helium in argon (pressure ratio 1:5) is slowed down to 500(250) m/s. The XUV and atomic beam can be aligned perpendicularly using the different gas mixtures within approximately 10^{-4} rad, resulting in a typical statistical error of 13 MHz for a single Doppler shift determination. Figure 6.9 shows a typical series, measured with pure helium and the two noble-gas mixtures. A systematic error in the Doppler shift is introduced by the uncertainty in the atomic beam velocity for the different gas mixtures. Because errors in the He velocity lead to a systematic error in the Doppler correction that is proportional to $\cos\phi$ (ϕ being the XUV-atomic beam angle) and the angle is kept small with changing signs by readjusting it, the systematic

Doppler shift in the ground state energy is smaller than 0.5 MHz, which is included in the error budget.

Measurement session level errors

The biggest correction at the measurement session level comes from the recoil shift on the considered transitions and can be calculated with high precision. It amounts to 18.28 and 18.75 MHz for the $1s\ ^1\mathrm{S}_1 - np\ ^1\mathrm{P}_1 (n \in 4, 5)$ transitions respectively.

As discussed in section 6.2, the IR beam is separated from the XUV beam an iris placed after the HHG interaction zone. However, some diffracted IR light can still reach the spectroscopy zone. Compared to the original IR beam, the diffracted light is found to be at least 27 times lower in intensity. this light can still produce an AC-Stark shift but only during the time of the excitation pulses (and not in between), Therefore it shows up in our measurement as a phase shift, which results in a different frequency shift for different f_{rep}.

The required correction is determined from a measurement with the beam block removed (i.e. with full IR intensity present in the interaction region). In this case we find a shift of 17.5(6.0) MHz on the $1s^2\ ^1\mathrm{S}_0 - 1s5p\ ^1\mathrm{P}_1$ at 148 MHz repetition frequency. With the beam block inserted for the regular helium measurements, a shift of less then 0.65 MHz is expected. Converting this to an equivalent phase shift of 14(14) mrad in the XUV allows to correct the other measurements performed at different repetition rates.

We have also estimated the theoretically expected frequency shift at $f_{rep} = 148$ MHz for the same case. The estimated average peak intensity with the beam stop removed is about 25 GW/cm^2, over a pulse duration of 300 fs. Between the two pulses the intensity is zero. The AC-Stark shift can be calculated by taking the time-averaged intensity [137] (for pulses 6.7 ns apart) of 1 MW/cm^2. It leads to a theoretical AC-Stark shift of 20 MHz, in good agreement with the experimental value, measured with the full IR beam passing the interaction zone.

Finally, we need to consider that the pulses for the phase measurement are split off via a 1 mm thick beam splitter (with fused silica as substrate material). After this point the pulses travel through the focusing lens (few mm BK7 glass) and enter the vacuum setup for HHG

via a Brewster window (another few mm BK7). Any difference in intensity between the two subsequent pulses that are used for the XUV comb generation, or any transient effect in these glass pieces, can cause an additional phase shift which is not taken into account by the generic phase-measurement procedure during recordings of the helium transition. To be able to still correct for this phase shift, a separate experiment was performed removing the IR/XUV separation iris in the vacuum setup. In this way the IR pulses could travel through the interaction zone to the monochromator, where they were coupled out through a window. Two beam splitters inside the monochromator vacuum chamber reduced the pulse energy to less than 0.1% of the original energy, thus avoiding spurious phase effects in the output window and other optics. A phase measurement was then performed on these pulses, while varying the pulse-energy ratio (which can be adjusted via the pump laser). This measurement resulted in an additional correction and uncertainty due to the optics placed between the phase-measurement setup and HHG (beam splitter, lens and Brewster window) of 8.5(15) mrad in the IR. This contribution (multiplied by 15 to take the harmonic order into account) is called "NL-phase shift" in the error budget in Table 6.1, where NL stands for the nonlinear origin of these differential phase shifts.

From Table 6.1 it is clear that the error contributions differ between the sessions due to different sizes of the corresponding data sets. Also a higher accuracy is achieved for the lower repetition rates in part because phase errors there result in smaller frequency errors. The highest uncertainty of 25 MHz at $f_{rep} = 185$ MHz is based on a very short measurement session, consisting of only one set of Doppler and 'ionization' series.

Evaluation of the He ground state energy

In the evaluation of the error in the ground state energy, the combined statistical and systematic error based on all sessions (3.7 MHz) is combined with several systematic errors represented as frequencies.

The biggest contribution to the uncertainty comes from the ionization shift model. This error contribution listed under "Ionization shift model" in Table 6.1 refers to the error introduced by the uncertainty in the power law of 2.1(6) between the XUV intensity and the amount of ion-

ization (and therefore phase shift) in the harmonic generation region. As this power law is used to correct for the ionization-induced shifts for all measurements at the measurement series level, it results in a systematic error. This is determined by re-analyzing the helium ionization potential for a power law of 1.5 and 2.7, resulting in a variation of 4.9 MHz. As an additional test of (mostly) ionization-induced errors, we also determined the ground state energy using only data points selected within a limited range of XUV-pulse energy, relative to the average XUV energy for each scan. Tests were performed for symmetric and anti-symmetric XUV energy distributions with 5% and 15% deviation from the average XUV energy. A maximum deviation of 5 MHz (from the value based on all points) was obtained in case of an asymmetric selection of data points with an XUV energy higher than 1.15 times the average energy. This is comparable with the estimated accuracy of the ionization model as it is based on a typical XUV yield and full distribution of XUV energies.

During the excitation time interval, the extraction fields for the time-of-flight spectrometer are switched off. The estimated residual field of less than 0.5 V/cm results in a calculated DC-Stark shift on the $5p$, $m = 0$ state of less than 20 kHz. There can be an additional field due to ions in the interaction zone left from the first excitation pulse. However, even for 1000 ions these fields are too small to cause a significant shift.

The influence of the Zeeman effect is estimated based on the magnetic field measured in the interaction region of 5×10^{-5} T. Because the excitation radiation originates from HHG, which has essentially zero yield for circular polarization, we can assume the circular component to be less than 1%. Since the ground state has no angular momentum, optical pumping cannot occur. Therefore only a weak (1%) $\Delta m = \pm 1$ component has to be taken into account, leading to a Zeeman shift of less than 7 kHz.

It is vital for Ramsey excitation, that only one transition is excited at a time. Excitation of other states would contribute also with a cosine of almost the same period, but a different phase (which changes quickly with the repetition rate of the FCL). A contribution from the $1s^2 - 1s2p$ transition, which is in the vicinity of the 13^{th}-harmonic can be excluded, as it can not be ionized with a single 1064 nm photon. But for the excitation of the $5p$ also the $6p$ level could possibly be excited.

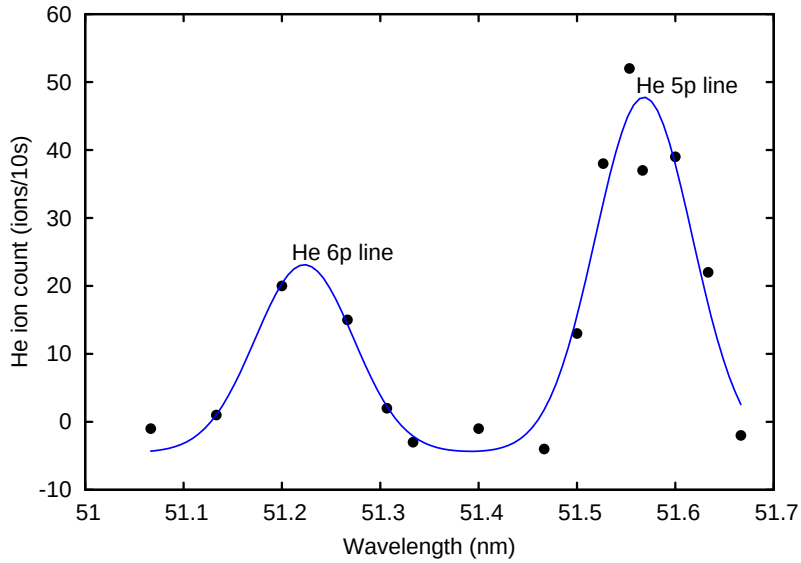

Figure 6.10: Excitation spectrum (single pulse) from the ground state to the $1s5p\ ^1\mathrm{P}_1$ and $1s6p\ ^1\mathrm{P}_1$ levels in helium, obtained by course scanning of the central wavelength of the fundamental and therefore its 15^{th} harmonic over the transitions.

To investigate this, the bandwidth of the XUV pulses was determined by coarse tuning of the IR central wavelength by moving the slit in the Fourier plane of the pulse stretcher, located before the parametric amplifier. As a result, the XUV comb spectrum is tuned as well, and scanned over the transitions. From the signal we subtracted a constant background signal from direct ionization due the 17^{th} and higher harmonics. This background has been found by blocking the ionization beam. A typical scan (corrected for the background) is depicted in Fig. 6.10. The solid line is a Gaussian fit of both the $5p$ and the $6p$ resonance, yielding a 1/e half width of the XUV spectrum of 0.07 nm at the 15^{th} harmonic.

From this width and the Gaussian profile we conservatively estimate a contribution to the $5p$ signal from the $6p$ resonance of less than 1%. This can cause a shift of the Ramsey pattern of at most 10 mrad (in the XUV). However, in practice the influence of this shift on the final transition frequency averages down for different repetition frequencies, so that the maximum error due to excitation of the $6p$ is less than 30 kHz for all measurements combined.

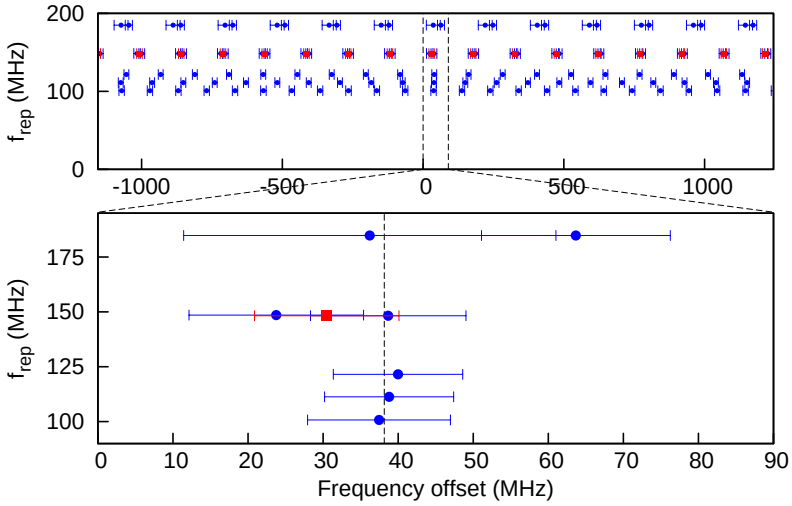

Figure 6.11: Measured ^{4}He ground state binding energy ($\pm n f_{rep}$) relative to the theoretical value of 5945204174 MHz [28], plotted against the repetition frequency f_{rep} of the comb laser. A clear coincidence is seen at +37(6) MHz relative to theory. The values indicated with a blue solid circle symbol are based on the $1s^2\ ^1\mathrm{S}_0 - 1s5p\ ^1\mathrm{P}_1$ transition. As a cross check, also a value based on the recorded $1s^2\ ^1\mathrm{S}_0 - 1s4p\ ^1\mathrm{P}_1$ transition is included (red square symbol at $f_{rep} = 148$ MHz), resulting in a consistent ground state energy.

After incorporating all the systematic corrections, a clear coincidence can be seen between the results for different repetition rates. A new ground state energy for ^{4}He of 5945204212(6) MHz is found by taking a weighted average over all measured frequencies at the coincidence location. The two most recent theoretical predictions of 5945204174(36) MHz from [28] and 5945204175(36) MHz from [30] are in agreement with this value within the combined uncertainty of theory and experiment. (The uncertainty of 36 MHz in both theoretical values is based on estimated but yet uncalculated higher-order QED contributions.) Remarkably, very good agreement is found with the prediction of Korobov [23], who calculates 5945204223(42) MHz, employing non-relativistic quantum electrodynamics theory, in which the problematic divergences of QED are canceled at the operator level. However, the uncertainties in the present calculations are too large to decide, which of the theoretical approaches is better suited to calculate the energy structure of few electron atoms.

Compared with the best previous determinations using single nanosecond laser pulses [40, 41], our new value is almost an order of

magnitude more accurate. Good agreement is found with the value of 5945204215(45) MHz from [40] (based on the measured transition energy in that paper, but corrected for a 14.6 MHz recoil shift that was previously not taken into account, and using the most recent $2p$ state ionization energy from [28]). However, there is a difference of nearly 3σ with the value of 5945204356(50) MHz from [41].

Signal contrast and phase stability of HHG

In the previous section phase information of the obtained cosine-shaped signals was used to determine the ground state ionization energy of helium. In the following we use the observed contrast of the same helium signals to investigate the phase stability of the generated XUV frequency comb. The signal visibility (ion signal modulation amplitude divided by the average signal) depends on a combination of effects.

The biggest contributions come from the line width of the observed transition, phase stability of the 15^{th} harmonic, Doppler broadening, and the width of the IR-FCL modes. In one extreme case ($f_{rep} = 185$ MHz, helium seeded in argon) we find a fringe contrast of 55%, while for $f_{rep} =$ 100 MHz and pure helium the contrast is below 5%. In Figure 6.12 the signal contrast is shown for several experimental conditions.

From an analysis of the observed visibility of the interference pattern as a function of the helium-beam velocity and comb repetition frequency, an estimate for the XUV comb phase jitter and of the effective width of the angular distribution of the atomic beam can be derived. We model the Ramsey pattern assuming Gaussian phase noise, while the Doppler effect is taken into account with various distributions, including Gaussian and rectangular. Both Doppler and phase-noise distribution widths are fitted in the procedure to the observed visibilities, and scans are included that were used in the frequency determination, plus additional scans that were performed on the $6p$ and $7p$ transitions. In all cases we assume a common background count rate of 15%. The resulting Doppler width and phase jitter depends on the function used for the Doppler distribution. For a Gaussian profile, we find a FWHM angular beam divergence of 2.4 mrad and 0.42 cycles XUV jitter. A rectangular distribution leads to a divergence angle of 4.3 mrad and 0.35 cycles XUV phase jitter. In both cases the model seems to have deficiencies. While in the former case

Effect	**Correction**	**Systematic uncertainty**	**Statistical uncertainty**
Single recording level			
Statistical fit error	—	—	typ. 50–150 mrad
Amplifier phase	$0 - 2.25$ rad	—	$75 - 375$ mrad
Combined error single recording		—	typ. $160 - 360$ mrad
Series level			
Doppler shift	$0 - 10$ MHz	see text	$8 - 18$ MHz
Ionization shift	$0 - 2$ rad	see 'ionization shift model'	$0.5 - 2.0$ rad
Session level			
AC-Stark shift	14 mrad	14 mrad - see text	—
NL - phase shift	128 mrad	225 mrad	—
Recoil shift 4p	18.28 MHz	$\ll 1$ MHz	—
Recoil shift 5p	18.75 MHz	$\ll 1$ MHz	—
Combined error single session		$9 - 25$ MHz	
Ground state evaluation			
Weighted mean of sessions	—	3.7 MHz	
Ionization shift model	—	4.9 MHz	—
Doppler shift	—	500 kHz	—
DC-Stark shift	—	< 1 kHz	—
Adjacent 6p-level	—	< 30 kHz	—
Zeeman shift	—	< 7 kHz	—
Total error in ground state energy		6 MHz	

Table 6.1: The error budget for the measurement of the ground-state binding energy of helium. The corrections and uncertainties are given either in radians or in MHz at the 15^{th} harmonic, depending on the type of effect (see text). The NL-phase shift denotes the differential phase shift (multiplied by 15 to account for its effect at the 15^{th} harmonic) induced in the optics after the phase measurement but before the HHG jet (see 6.4).

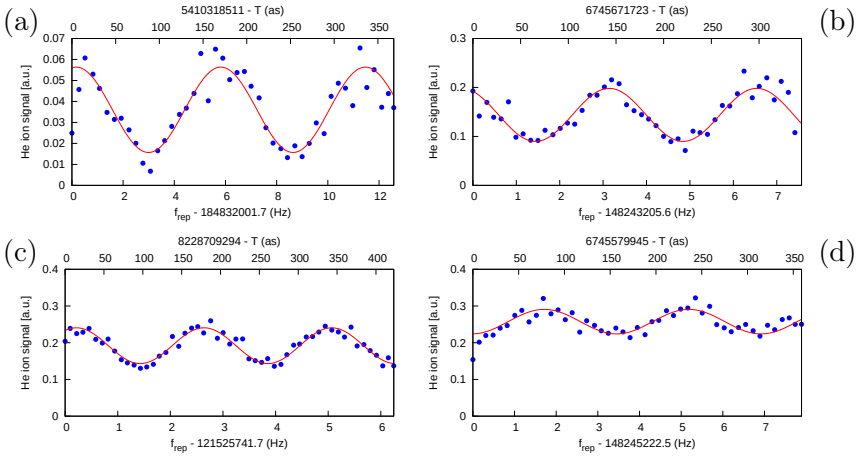

Figure 6.12: Ramsey signal of helium, acquired with different experimental conditions. (a) $f_{rep} = 185$ MHz, $1s^2\ {}^1\mathrm{S}_0 - 1s5p\ {}^1\mathrm{P}_1$ transition, helium seeded in argon, contrast: 56%, (b) $f_{rep} = 148$ MHz, $1s^2\ {}^1\mathrm{S}_0 - 1s5p\ {}^1\mathrm{P}_1$ transition, helium seeded in neon, contrast: 38%, (c) $f_{rep} = 121$ MHz, $1s^2\ {}^1\mathrm{S}_0 - 1s5p\ {}^1\mathrm{P}_1$ transition, helium seeded in neon, contrast: 25%, (d) $f_{rep} = 148$ MHz, $1s^2\ {}^1\mathrm{S}_0 - 1s4p\ {}^1\mathrm{P}_1$ transition, pure helium beam, contrast: 13%.

the visibility seems to be systematically underestimated for slow beams, in the latter case this underestimation is less pronounced and the fit becomes worse for the fast He beams where the angular distribution is important. We therefore estimate an intermediate value of 0.38(6) cycles for the XUV phase jitter.

If we consider the contributions to the XUV comb jitter then the biggest contribution arises from the bandwidth of the modes of the FC in the IR. The bandwidth of the FC was measured in a separate experiment by beating the FC modes with a frequency doubled narrow bandwidth Er-fiber laser (NP Photonics, with a short-term line width of 5 kHz) to yield a value of 1.6 MHz FWHM, corresponding to a jitter of 1/6 of an XUV cycle.

A second contribution comes from the phase uncertainty of 47 mrad FWHM in the amplified pulses after correction for the measured phase shift (evaluated near the peak intensity of the pulse), leading to a jitter of 1/9 cycle in the XUV. For HHG we take into account that the phase of the generated harmonics is proportional to the intensity of the fundamental beam [79], with an estimated factor of $\approx 10^{-13}$ rad cm^2/ W, using the results presented in [144]. Combined with an NOPCPA pulse-

ratio distribution FWHM of 2.5%, this gives a small expected jitter of 0.02 XUV cycles. Fluctuations of 6% in the IR pulse intensity lead to variations in the level of ionization in the HHG jet of more than 35% (as ionization scales with at least the 7^{th} power of the IR intensity for the conditions in the experiment). If we adopt a typical average ionization correction of 0.1 XUV cycles, then this induces a phase jitter of 0.04 XUV cycles. Krypton density fluctuations ($< 20\%$) induce less than half this value.

Statistically independent combination of these noise sources leads to a total expected phase jitter in the XUV of 0.21 cycles. This is lower, but comparable to the jitter extracted from the contrast measurements. The difference might be due to uncertainties in the exact experimental conditions, in particular the Doppler broadening and the bandwidth of the frequency comb laser modes during the experiments.

The (estimated) contributions to the jitter suggest that the contrast should hardly be influenced by intensity-induced phase noise from the HHG process. This was investigated experimentally by taking only a subset of the data points to determine the contrast, using a selection criterion based on the measured XUV intensity. With this procedure we find that the visibility of the interference does not change (within a few percent) if we restrict the XUV intensity variation to symmetric bands of 5%, and 40% around the mean XUV energy. We therefore conclude that intensity dependent effects do not play a significant role as a source of phase noise in the XUV comb in the present experiment.

6.5 Conclusions and outlook

The metrology presented in this article represents a significant advance in the history of precision extreme ultraviolet spectroscopy. As is illustrated in the historical overview of the spectroscopy of the helium atom, depicted in Fig. 6.13, the theoretical and experimental accuracy of the value of the binding energy of helium improved by many orders of magnitude over the last hundred years. Experimentally the biggest progress has always been initiated by new methods, which in turn also lead to advances in the theoretical understanding. The pioneering measurement by Herzberg [145] in 1958 based on a helium lamp and grating spectrom-

eter was not significantly improved upon until the first laser excitation in 1993 [127].

In this paper we have described the first absolute frequency measurement in the XUV spectral region, based on parametric amplification and harmonic upconversion of two pulses from an IR frequency comb laser. Direct frequency comb excitation in the XUV of helium from the ground state is demonstrated, leading to an almost 10-fold improved ground state ionization energy, and in good agreement with theory.

For the employed method it is vitally important to control and detect phase shifts in the amplification and harmonic upconversion process. An important aspect of direct excitation with an upconverted frequency comb is the possibility to detect systematic errors due to phase shifts between the pulses from the NOPCPA, HHG and ionization, but also from the AC-Stark effect. Uncorrected errors of this kind show up as a frequency shift that is proportional to f_{rep}, and can therefore be detected easily. In the current experiment no dependence on the repetition rate is observed in the measurements (see Fig. 6.11), indicating that the systematic effects have been taken into account properly. The accuracy of the presented method scales with f_{rep}, which also means that it can be improved by orders of magnitude by choosing frequency comb pulses further apart. If the pulse delay would be extended to > 150 ns, then the ionization shift introduced in the HHG process would in fact vanish altogether, as the time between the pulses would be sufficiently long to replace the gas in the focal region with a new sample before the second pulse arrives. This would reduce the error in the spectroscopy significantly because the biggest source of uncertainty is currently due to ionization effects in the HHG process. To fully exploit the enhanced accuracy with larger pulse delays, the sample has to be trapped and cooled to reduce Doppler and time-of-flight broadening which would otherwise wash out the ever denser signal modulation. In view of this, measurements on He^+ are particularly interesting. This ion has a hydrogen-like electronic configuration which can be excited from the ground state using a two-photon transition at 60 nm. Such an experiment has the potential to perform QED tests beyond what has been possible so far in atomic hydrogen [6, 153].

In the present work a frequency comb laser in the XUV range is demonstrated, for the first time at wavelengths as short as 51 nm. The

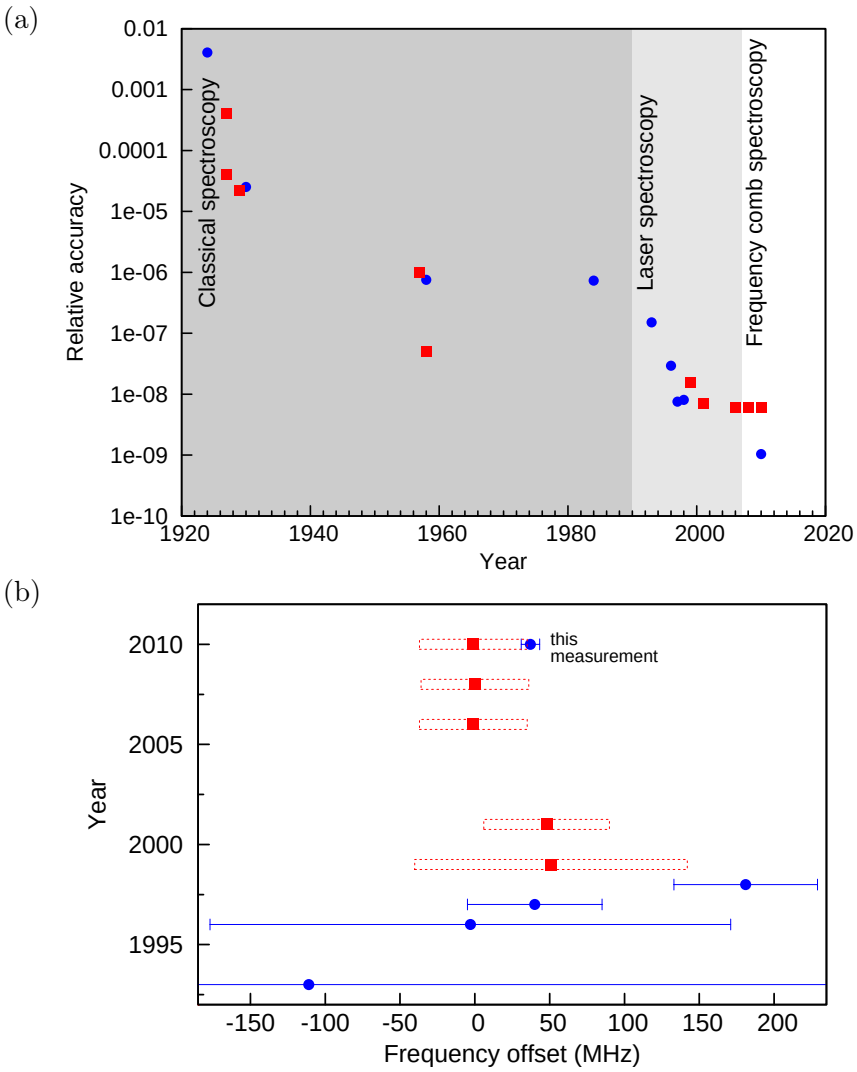

Figure 6.13: (a) Advance in theoretical and spectroscopic accuracy of the ground state energy of helium over the last 100 years. The shaded areas emphasize new spectroscopic tools that allowed to overcome limits of previous technologies. Red squares represent the precision of calculations. The precision obtained in experiments is indicated with blue circles. (b) Comparison of helium ground state ionization energy values obtained experimentally and theoretically in the last two decades. The values are plotted with respect to the most recent theoretical result [41, 40, 145, 22, 146, 147, 148, 149, 28, 150, 24, 30, 127, 128, 23, 151, 31, 152].

phase jitter of the XUV frequency comb modes is found to be 0.38(6) cycles. From the results we conclude that the observed comb jitter in the XUV is not dominated by the HHG upconversion process, but most likely by the stability of the original comb in the infrared. This form of technical noise can be considerably reduced by locking the comb laser to a stable optical reference cavity. It seems therefore feasible to extend comb generation and spectroscopy to even shorter wavelengths into the soft-X-ray region, provided that the carrier-phase noise of the fundamental and upconverted pulses is kept low enough. Further possibilities would arise if not subsequent pulses from the FC, but any two-pulse sequence could be selected for upconversion. This would increase the accuracy significantly below 1 MHz as the pulses could have a much increased time delay, thus making it possible to resolve multiple transitions with discrete Fourier transform spectroscopy techniques. In view of these possibilities, we envision applications such as QED test of He^+ and highly charged ions, precision spectroscopy of simple molecules such as H_2, coherent XUV or X-ray imaging, and possibly even the emergence of X-ray nuclear clocks.

Chapter 7

Outlook

In this thesis an account is given of the development of the first XUV-frequency comb and the spectroscopic experiment at ≈ 51.5 nm performed with it on the helium atom. The developed instrument is therefore a prototype, which naturally leaves some room for improvement. At the same time, already in its present state many spectroscopic experiments with frequency comb excitation are feasible in the XUV wavelength range.

It has been shown that the developed instrument can produce a frequency comb at every wavelength between 200 nm and 50 nm [154]. Demonstration of a frequency comb spectrum at wavelengths below 50 nm would need considerable additional instrumental effort, because such high transition frequencies don't exist in neutral atoms, but only in ionized species such as e.g. singly ionized helium.

In the following two sections an example will be given of a measurement that can be carried out using the source of strong phase-coherent pulses that has been described in chapter 3 of this thesis. To conclude an example of a possible technical development is presented that would extend the range of possible applications of this source.

7.1 Two-photon excitation of the $1s^2\ {}^1\mathrm{S}_0 - 1s2s\ {}^1\mathrm{S}_0$ transition in helium

A limiting factor to the applied method of direct frequency comb spectroscopy is the lifetime of the excited states involved. A long lifetime is particularly interesting in view of the Ramsey excitation approach presented in this thesis. The main sources of uncertainty in the measurement presented in chapter 6 are directly related to the uncertainties in the phase coherence of the used IR- and XUV-pulses. These uncer-

tainties appear in the measured frequency as a function of the inverse repetition time of the pulses, and can therefore be reduced considerably by increasing the delay between the amplified IR-frequency comb pulses.

From this perspective the metastable $1s2s\ ^3\mathrm{S}_1$ state of helium, which exhibits a lifetime of 8000 s seems very interesting. However, optical excitation to this state is strongly forbidden from the $1s^2\ ^1\mathrm{S}_0$ ground state as this would require a spin flip of one of the electrons. Recently [155] it was shown that high resolution spectroscopy is in fact possible between the $1s2s\ ^3\mathrm{S}_1$ and $1s2s\ ^1\mathrm{S}_0$ using a strong (on the order of a few hundred mW) and narrow bandwidth laser at 1557 nm. An optical dipole trap for the $1s2s\ ^3\mathrm{S}_1$ was used to keep helium in the interaction zone, so that interaction times on the order of a second could be achieved in order to compensate for the extremely low excitation probability. To do the same from the ground state is not feasible because of a lack of laser power in the XUV. However, the $1s2s\ ^1\mathrm{S}_0$ still has a comparatively long lifetime of 20 ms, and can be excited from the ground state using a spin-allowed two-photon transition. Excitation with two equal photons of 120.2 nm has been demonstrated with single nanosecond duration pulses with a precision of 48 MHz [41].

For direct frequency comb excitation a Raman scheme might be more appropriate than the above-mentioned two-photon excitation scheme. A suitable Raman scheme coul consist of one photon at the 13^{th} harmonic and one at the fundamental IR wavelength as depicted in figure 7.1. If both beams come from the same side (as is already the case in the presented experiments), then both the XUV and IR combs will have the same Doppler shift and mode spacing, so that many comb modes can contribute pair-wise to the signal. Effectively the transition is made with the 12^{th} harmonic of 721.5 nm. Another advantage of this configuration is the enhancement from the $1s3p$ state, leading to a much higher signal than for equal energy photon without any intermediate nearby resonance. The only downside is that Doppler effects are not canceled in this configuration, so that the Doppler shift still has to be calibrated.

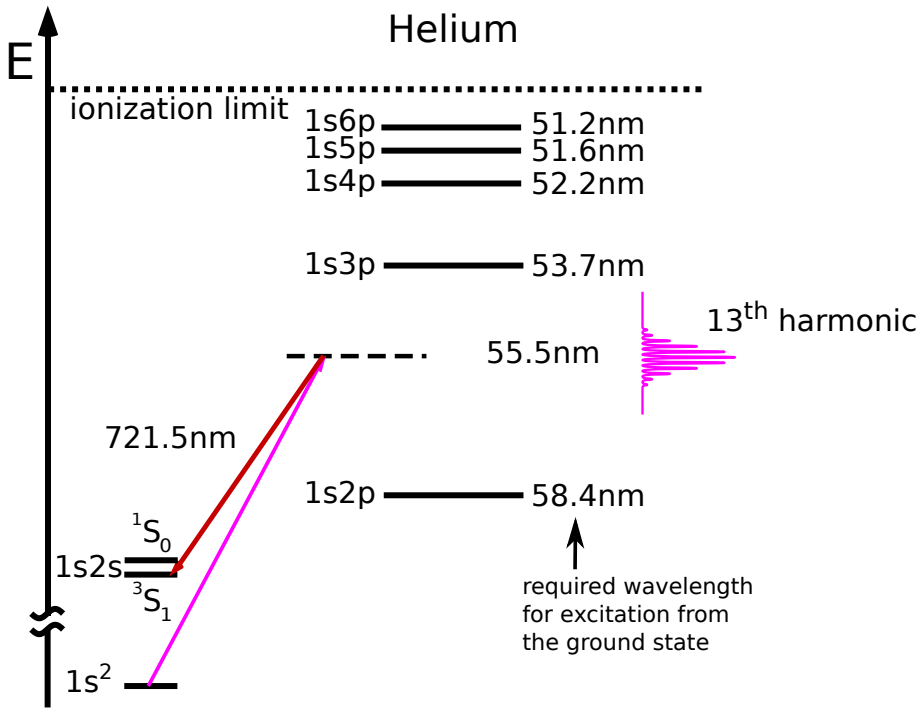

Figure 7.1: Excitation of the $1s2s$ ^{1}S level using the 13$^{\text{th}}$ minus the 1$^{\text{st}}$ harmonic of 721.5 nm.

7.2 Programmable pulse delay for Fourier-transform spectroscopy of moderately complicated spectra

Direct excitation with a frequency comb has an inherent ambiguity because the signal repeats for every comb mode. This problem of the the indistinguishability of the XUV-frequency comb modes can be resolved with a series of measurements performed at different repetition-rates (see Fig. 6.11).

The change of the repetition rate for the helium experiment involved a cumbersome procedure in which the cavity-length of the fundamental FCL was changed, as well as the relay-imaged delay line (Fig. 3.4) in the pump laser of the NOPCPA. Every such reconstruction took many hours and spread the frequency measurement over several weeks. The prospect to spend several weeks to measure one frequency is not encouraging. However, it is feasible to reduce the duration of such measurement to

one day by employing a pump-laser system with a programmable pulse delay. It is preferably done in combination with the same repetition rate of the two fundamental oscillators: the seed oscillator of the pump laser and the IR-FCL respectively.

This can be done by an inclusion of a preamplifier pair in the pump-laser system, which is capable to independently amplify different pulses from the seed laser before injecting them into the power-amplifier modules. This would allow the amplification of any pulse sequence from the fundamental FCL that is temporally separated by n times the repetition time of the FCL, where n is a integer number.

Such XUV-FC with a programmable spectral structure could reduce the time needed for a frequency measurement in the XUV to one day. Moreover, a programmable pulse delay would open the route to the powerful method of Fourier transform spectroscopy (FTS), that is commonly used for molecular spectroscopy in the infrared and was employed for the first time by Rubens in 1910 [156] in the far infrared spectral region at 40 μm. On the other end of the spectrum, recently FTS at wavelengths as short as 40 nm was demonstrated with a relative accuracy of 10^{-7} using a split-wavefront technique and a synchrotron as a light source [157]. By using a frequency comb to create phase coherent pulses in the XUV (or even soft X-rays) with a programmable pulse delay, FTS could be extended to shorter wavelengths and with a many orders of magnitude higher accuracy. The method could also be used to investigate more complicated spectra (such as from molecules) than a single transition, with several resonances within the spectrum of the XUV-FC. The accessible pulse delays at which the interference signal can be recorded are multiples of the repetition rate of the fundamental FCL. However, sampling the quantum-interference signal at many pulse delays and same experimental conditions would provide the information necessary to identify the frequency of each resonance. The applicability of this approach, however, hinges on the longevity of the investigated resonances, and all spectral lines are mapped onto the same interval equal to the pulse repetition rate. To fully exploit the possibilities, cold samples need to be used, otherwise Doppler broadening (in the case of one-photon transitions) would wash out the fringes of the signal. One possible way to achieve this is confinement of ions in a Paul trap, combined with (sympathetic) laser cooling.

Very interesting candidates for such spectroscopy are H_2^+ [117, 116] and He^+ [153].

Bibliography

[1] W. E. Lamb and R. C. Retherford, *Fine structure of the hydrogen atom. Part I*, Physical Review **79**, 549 (1950).

[2] R. P. Feynman, *Space-time approach to quantum electrodynamics*, Physical Review **76**, 769 (1949).

[3] J. Schwinger, *Quantum electrodynamics. I. A covariant formulation*, Physical Review **74**, 1439 (1948).

[4] S. Tomonaga, *On a relativistically invariant formulation of the quantum theory of wave fields*, Progress of Theoretical Physics **1**, 27 (1946).

[5] P. J. Mohr, B. N. Taylor, and D. B. Newell, *CODATA recommended values of the fundamental physical constants: 2006*, Reviews of Modern Physics **80**, 633 (2008).

[6] M. Fischer et al., *New limits on the drift of fundamental constants from laboratory measurements*, Physical Review Letters **92**, 230802 (2004).

[7] H. Schnatz, B. Lipphardt, J. Helmcke, F. Riehle, and G. Zinner, *First phase-coherent frequency measurement of visible radiation*, Physical Review Letters **76**, 18 (1996).

[8] T. Udem, A. Huber, B. Gross, J. Reichert, M. Prevedelli, M. Weitz, and T. W. Hänsch, *Phase-coherent measurement of the hydrogen $1S - 2S$ transition frequency with an optical frequency interval divider chain*, Physical Review Letters **79**, 2646 (1997).

[9] D. J. Jones, S. A. Diddams, J. K. Ranka, A. Stentz, R. S. Windeler, J. L. Hall, and S. T. Cundiff, *Carrier-envelope phase control of fem-*

tosecond mode-locked lasers and direct optical frequency synthesis, Science **288**, 635 (2000).

[10] R. Holzwarth, Th. Udem, T. W. Hänsch, J. C. Knight, W. J. Wadsworth, and P. St. J. Russel, *Optical frequency synthesizer for precision spectroscopy*, Physical Review Letters **85**, 2264 (2000).

[11] C. W. Chou, D. B. Hume, J. C. J. Koelemeij, D. J. Wineland, and T. Rosenband, *Frequency comparison of two high-accuracy Al^+ optical clocks*, Physical Review Letters **104**, 070802 (2010).

[12] T. H. Yoon, J. Ye, J. L. Hall, and J. M. Chartier, *Absolute frequency measurement of the iodine-stabilized laser at 633 nm*, Applied Physics B: Lasers and Optics **72**, 221 (2001).

[13] H. Telle, G. Steinmeyer, A. Dunlop, J. Stenger, D. Sutter, and U. Keller, *Carrier-envelope offset phase control: A novel concept for absolute optical frequency measurement and ultrashort pulse generation*, Applied Physics B: Lasers and Optics **69**, 327 (1999).

[14] H. Telle, B. Lipphardt, and J. Stenger, *Kerr-lens, mode-locked lasers as transfer oscillators for optical frequency measurements*, Applied Physics B: Lasers and Optics **74**, 1 (2002).

[15] P. B. Corkum and F. Krausz, *Attosecond science*, Nature Physics **3**, 381 (2007).

[16] Ch. Gohle et al., *A frequency comb in the extreme ultraviolet*, Nature **436**, 234 (2005).

[17] R. J. Jones, K. D. Moll, M. J. Thorpe, and J. Ye, *Phase-coherent frequency combs in the vacuum ultraviolet via high-harmonic generation inside a femtosecond enhancement cavity*, Physical Review Letters **94**, 193201 (2005).

[18] D. C. Yost, T. R. Schibli, J. Ye, J. L. Tate, J. Hostetter, M. B. Gaarde, and K. J. Schafer, *Vacuum-ultraviolet frequency combs from below-threshold harmonics*, Nature Physics **5**, 815 (2009).

[19] S. Witte, R. Th. Zinkstok, W. Ubachs, W. Hogervorst, and K. S. E. Eikema, *Deep-ultraviolet quantum interference metrology with ultrashort laser pulses*, Science **307**, 400 (2005).

[20] R. Th. Zinkstok, S. Witte, W. Ubachs, W. Hogervorst, and K. S. E. Eikema, *Frequency comb laser spectroscopy in the vacuum-ultraviolet region*, Physical Review A: Atomic, Molecular, and Optical Physics **73**, 061801 (2006).

[21] D. Z. Kandula, C. Gohle, T. J. Pinkert, W. Ubachs, and K. S. E. Eikema, *Extreme ultraviolet frequency comb metrology*, Physical Review Letters **105**, 063001 (2010).

[22] E. A. Hylleraas, *Neue Berechnung der Energie des Heliums im Grundzustande, sowie des tiefsten Terms von Ortho-Helium*, Zeitschrift für Physik **54**, 347 (1929).

[23] V. Korobov and A. Yelkhovsky, *Ionization potential of the helium atom*, Physical Review Letters **87**, 193003 (2001).

[24] G. W. F. Drake, *High precision theory of atomic helium*, Physica Scripta **1999**, 83 (1999).

[25] G. W. F. Drake, *Long-range casimir forces: theory and recent experiments on atomic systems*, chap. 3 High-Precision Calculations for the Rydberg States of Helium, pp. 107–217 (Plenum Press, 1993).

[26] H. A. Bethe and E. E. Salpeter, *Quantum mechanics of one- and two-electron atoms* (Dover Publications, 2008).

[27] A. K. Bhatia and R. J. Drachman, *The mass polarization effect in He-like ions: first and second order*, Journal of Physics B: Atomic, Molecular and Optical Physics **36**, 1957 (2003).

[28] V. A. Yerokhin and K. Pachucki, *Theoretical energies of low-lying states of light helium-like ions*, Physical Review A: Atomic, Molecular, and Optical Physics **81**, 022507 (2010).

[29] G. Breit, *The effect of retardation on the interaction of two electrons*, Physical Review **34**, 553 (1929).

[30] G. W. F. Drake and Z. C. Yan, *High-precision spectroscopy as a test of quantum electrodynamics in light atomic systems*, Canadian Journal of Physics **86**, 45 (2008).

[31] K. Pachucki, *$\alpha^4 Ry$ corrections to singlet states of helium*, Physical Review A: Atomic, Molecular, and Optical Physics **74**, 022512 (2006).

[32] K. Pachucki, *Helium energy levels including $m\alpha^6$ corrections*, Physical Review A: Atomic, Molecular, and Optical Physics **74**, 062510 (2006).

[33] P. A. M. Dirac, *Über die Quantunmechanik der Stoßvorgänge*, Zeitschrift für Physik **44**, 585 (1927).

[34] E. Fermi, *Quantum theory of radiation*, Reviews of Modern Physics **4**, 87 (1932).

[35] W. E. Lamb and R. C. Retherford, *Fine structure of the hydrogen atom by a microwave method*, Physical Review **72**, 241 (1947).

[36] H. A. Bethe, *The electromagnetic shift of energy levels*, Physical Review **72**, 339 (1947).

[37] A. Gumberidze et al., *Precision tests of QED in strong fields: experiments on hydrogen- and helium-like uranium*, Journal of Physics: Conference Series **58**, 87 (2007).

[38] K. Pachucki, *Complete two-loop binding correction to the Lamb shift*, Physical Review Letters **72**, 3154 (1994).

[39] W. E. Caswell and G. P. Lepage, *Effective lagrangians for bound state problems in QED, QCD, and other field theories*, Physics Letters B **167**, 437 (1986).

[40] K. S. E. Eikema, W. Ubachs, W. Vassen, and W. Hogervorst, *Lamb shift measurement in the 1^1S ground state of helium*, Physical Review A: Atomic, Molecular, and Optical Physics **55**, 1866 (1997).

[41] S. D. Bergeson et al., *Measurement of the He ground state Lamb shift via the two-photon $1^1\mathrm{S} - 2^1\mathrm{S}$ transition*, Physical Review Letters **80**, 3475 (1998).

[42] A. Akhamov, Sergei, V. A. Vysloukh, and A. S. Chirkin, *Optics of femtosecond laser pulses* (American Institute of Physics, 1992).

[43] R. W. Boyd, *Nonlinear optics* (Elsevier Academic Press, 2008).

[44] Y. Shen, *The principles of nonlinear optics* (John Wiley & Sons, Inc., 2003).

[45] M. Perry, *Crossing the petawatt threshold*, Science & Technology Review **2**, 4 (1996).

[46] A. E. Siegman, *Lasers* (University Science Books, 1986).

[47] M. Nisoli et al., *Compression of high-energy laser pulses below 5 fs*, Optics Letters **22**, 522 (1997).

[48] P. A. Franken, A. E. Hill, C. W. Peters, and G. Weinreich, *Generation of optical harmonics*, Physical Review Letters **7**, 118 (1961).

[49] M. Niering et al., *Measurement of the hydrogen 1S-2S transition by phase coherent comparison with a microwave cesium fountain clock*, Physical Review Letters **84**, 5496 (2000).

[50] J. Helmcke, G. Wilpers, T. Binnewies, C. Degenhardt, U. Sterr, H. Schnatz, and F. Riehle, *Optical frequency standard based on cold Ca atoms*, IEEE Transactions on Instrumentation and Measurement **52**, 250 (2003).

[51] F. Keilmann, Ch. Gohle, and R. Holzwarth, *Time-domain mid-infrared frequency-comb spectrometer*, Optics Letters **29**, 1542 (2004).

[52] T. Yasui, Y. Kabetani, E. Saneyoshi, S. Yokohama, and T. Araki, *Terahertz frequency comb by multifrequency-heterodyning photoconductive detection for high-accuracy, high-resolution terahertz spectroscopy*, Applied Physics Letters **88**, 241104 (2006).

[53] E. Peters, S. A. Diddams, P. Fendel, S. Reinhard, T. W. Hänsch, and Th. Udem, *A deep-UV optical frequency comb at 205 nm*, Optics Express **17**, 9183 (2009).

[54] I. Coddington, W. C. Swann, L. Nenadovic, and N. R. Newbury, *Rapid and precise absolute distance measurements at long range*, Nature Photonics **3**, 351 (2009).

[55] S. Witte, R. Th. Zinkstok, W. Hogervorst, and K. Eikema, *Control and precise measurement of carrier-envelope phase dynamics*, Applied Physics B: Lasers and Optics **78**, 5 (2004).

[56] K.-K.. Ni et al., *A high phase-space-density gas of polar molecules*, Science **322**, 231 (2008).

[57] P. Del'Haye, O. Arcizet, A. Schliesser, R. Holzwarth, and T. J. Kippenberg, *Full stabilization of a microresonator-based optical frequency comb*, Physical Review Letters **101**, 053903 (2008).

[58] S. T. Cundiff, J. Ye, and J. L. Hall, *Optical frequency synthesis based on mode-locked lasers*, Review of Scientific Instruments **72**, 3749 (2001).

[59] J. K. Ranka, R. S. Windeler, and A. J. Stentz, *Optical properties of high-delta air silica microstructure optical fibers*, Optics Letters **25**, 796 (2000).

[60] S. A. Diddams et al., *Direct link between microwave and optical frequencies with a 300 THz femtosecond laser comb*, Physical Review Letters **84**, 5102 (2000).

[61] P. M. Goorjian and S. T. Cundiff, *Nonlinear effects on the carrier-envelope phase*, Optics Letters **29**, 1363 (2004).

[62] K. Holman, R. Jones, A. Marian, and S. J. Y. Cundiff, *Detailed studies and control of intensity-related dynamics of femtosecond frequency combs from mode-locked Ti:sapphire lasers*, IEEE Journal of Selected Topics in Quantum Electronics **9**, 1018 (2003).

[63] S. Koke, C. Grebing, H. Frei, A. Anderson, A. Assion, and G. Steinmeyer, *Direct frequency comb synthesis with arbitrary offset and shot-noise-limited phase noise*, Nature Photonics **4**, 462 (2010).

[64] J. Eckstein, A. I. Ferguson, and T. W. Hänsch, *High-resolution two-photon spectroscopy with picosecond light pulses*, Physical Review Letters **40**, 847 (1978).

[65] A. L. Wolf, S. A. van den Berg, C. Gohle, E. J. Salumbides, W. Ubachs, and K. S. E. Eikema, *Frequency metrology on the*

$4s\ ^2\mathrm{S}_{1/2} - 4p\ ^2\mathrm{P}_{1/2}$ *transition in* $^{40}Ca^+$ *for a comparison with quasar data*, Physical Review A: Atomic, Molecular, and Optical Physics **78**, 032511 (2008).

[66] I. V. Hertel and C.-P. Schulz, *Atome, Moleküle und optische Physik 2 Moleküle und Photonen - Spektroskopie und Streuphysik* (Springer Berlin Heidelberg, 2010).

[67] N. F. Ramsey, *A new molecular beam resonance method*, Physical Review **76**, 996 (1949).

[68] D. J. Armstrong, W. J. Alford, T. D. Raymond, A. V. Smith, and M. S. Bowers, *Parametric amplification and oscillation with walkoff-compensating crystals*, Journal of the Optical Society of America B: Optical Physics **14**, 460 (1997).

[69] G. Cerullo and S. D. Silvestri, *Ultrafast optical parametric amplifiers*, Review of Scientific Instruments **74**, 1 (2003).

[70] S. Witte, *Terawatt-intensity few-cycle laser pulses Optical parametric chirped pulse amplification and frequency comb spectroscopy*, Ph.D. thesis, Vrije Universiteit Amsterdam (2007).

[71] S. Witte and K. S. E. Eikema, *Ultrafast optical chirped-pulse amplification*, IEEE Journal of Selected Topics in Quantum Electronics **99**, 1 (2010).

[72] I. N. Ross, P. Matousek, G. H. C. New, and K. Osvay, *Analysis and optimization of optical parametric chirped pulse amplification*, Journal of the Optical Society of America B: Optical Physics **19**, 2945 (2002).

[73] S. Witte, R. Th. Zinkstok, W. Hogervorst, and K. S. E. Eikema, *Numerical simulations for performance optimization of a few-cycle terawatt NOPCPA system*, Applied Physics B **87**, 677 (2007).

[74] A. McPherson et al., *Studies of multiphoton production of vacuum-ultraviolet radiation in the rare gases*, Journal of the Optical Society of America B: Optical Physics **4**, 595 (1987).

[75] M. Ferray, A. L'Huillier, X. F. Li, L. A. Lompre, G. Mainfray, and C. Manus, *Multiple-harmonic conversion of 1064 nm radiation in rare gases*, Journal of Physics B: Atomic, Molecular and Optical Physics **21**, L31 (1988).

[76] P. B. Corkum, *Plasma perspective on strong field multiphoton ionization*, Physical Review Letters **71**, 1994 (1993).

[77] B. Piraux (Ed.), *Super intense laser atom physics*, vol. III of *SILAP* (Plenum Press, 1993).

[78] A. L'Huillier, M. Lewenstein, P. Salières, Ph. Balcou, M. Y. Ivanov, J. Larsson, and C. G. Wahlström, *High-order harmonic-generation cutoff*, Physical Review A: Atomic, Molecular, and Optical Physics **48**, R3433 (1993).

[79] M. Lewenstein, Ph. Balcou, M. Yu. Ivanov, A. L'Huillier, and P. B. Corkum, *Theory of high-harmonic generation by low-frequency laser fields*, Physical Review A: Atomic, Molecular, and Optical Physics **49**, 2117 (1994).

[80] M. Lewenstein, P. Salières, and A. L'Huillier, *Phase of the atomic polarization in high-order harmonic-generation*, Physical Review A: Atomic, Molecular, and Optical Physics **52**, 4747 (1995).

[81] L. V. Keldysh, *Ionization in the field of a strong electromagnetic wave*, Journal of Experimental and Theotetical Physics (U.S.S.R.) **20**, 1307 (1965).

[82] A. L'Huillier, P. Balcou, S. Candel, K. J. Schafer, and K. C. Kulander, *Calculations of high-order harmonic-generation processes in xenon at 1064 nm*, Physical Review A: Atomic, Molecular, and Optical Physics **46**, 2778 (1992).

[83] P. Antoine, A. L'Huillier, M. Lewenstein, P. Salières, and B. Carré, *Theory of high-order harmonic generation by an elliptically polarized laser field*, Physical Review A: Atomic, Molecular, and Optical Physics **53**, 1725 (1996).

[84] P. Salières, A. L'Huillier, and M. Lewenstein, *Coherence control of high-order harmonics*, Physical Review Letters **74**, 3776 (1995).

[85] I. J. Kim et al., *Highly efficient high-harmonic generation in an orthogonally polarized two-color laser field*, Physical Review Letters **94**, 243901 (2005).

[86] L. G. Gouy, *Sur une propriete nouvelle des ondes lumineuses*, Comptes rendus de l'Académie de sciences **110**, 1251 (1890).

[87] A. Pirri, C. Corsi, E. Sali, A. Tortora, and M. Bellini, *Interferometric measurement of the atomic dipole phase for the two electronic quantum paths generating high-order harmonics*, Laser Physics **17**, 138 (2007).

[88] J. Seres et al., *Laser-driven amplification of soft X-rays by parametric stimulated emission in neutral gases*, Nature Physics **6**, 455 (2010).

[89] S. Witte, R. Th. Zinkstok, A. L. Wolf, W. Hogervorst, W. Ubachs, and K. S. E. Eikema, *A source of 2 terawatt, 2.7 cycle laser pulses based on noncollinear optical parametric chirped pulse amplification*, Optics Express **14**, 8168 (2006).

[90] M. Y. Sander, E. P. Ippen, and F. X. Kärtner, *Carrier-envelope phase dynamics of octave-spanning dispersion-managed Ti: sapphire lasers*, Optics Express **18**, 4948 (2010).

[91] A. Renault, D. Z. Kandula, S. Witte, A. L. Wolf, R. Th. Zinkstok, W. Hogervorst, and K. S. E. Eikema, *Phase stability of terawatt-class ultrabroadband parametric amplification*, Optics Letters **32**, 2363 (2007).

[92] M. Bellini, C. Lyngå, A. Tozzi, M. B. Gaarde, T. W. Hänsch, A. L'Huillier, and C.-G. Wahlström, *Temporal coherence of ultrashort high-order harmonic pulses*, Physical Review Letters **81**, 297 (1998).

[93] A. Baltuška et al., *Attosecond control of electronic processes by intense light fields*, Nature **421**, 189 (2003).

[94] M. F. Kling et al., *Control of electron localization in molecular dissociation*, Science **312**, 246 (2006).

[95] A. J. Verhoef, J. Seres, K. Schmid, Y. Nomura, G. Tempea, L. Veisz, and F. Krausz, *Compression of the pulses of a Ti:sapphire laser system to 5 femtoseconds at 0.2 terawatt level*, Applied Physics B: Lasers and Optics **82**, 513 (2006).

[96] C. P. Hauri et al., *Generation of intense, carrier-envelope phase-locked few-cycle laser pulses through filamentation*, Applied Physics B: Lasers and Optics **79**, 673 (2004).

[97] A. Baltuška, T. Fuji, and T. Kobayashi, *Controlling the carrier-envelope phase of ultrashort light pulses with optical parametric amplifiers*, Physical Review Letters **88**, 133901 (2002).

[98] C. Vozzi et al., *High-energy, few-optical-cycle pulses at* $1.5\mu m$ *with passive carrier-envelope phase stabilization*, Optics Express **14**, 10109 (2006).

[99] R. Th. Zinkstok, S. Witte, W. Hogervorst, and K. S. E. Eikema, *High-power parametric amplification of 11.8-fs laser pulses with carrier-envelope phase control*, Optics Letters **30**, 78 (2005).

[100] C. P. Hauri, P. Schlup, G. Arisholm, J. Biegert, and U. Keller, *Phase-preserving chirped-pulse optical parametric amplification to 17.3 fs directly from a Ti:sapphire oscillator*, Optics Letters **29**, 1369 (2004).

[101] M. Kakehata, H. Takada, Y. Kobayashi, K. Torizuka, Y. Fujihira, T. Homma, and H. Takahashi, *Single-shot measurement of carrier-envelope phase changes by spectral interferometry*, Optics Letters **26**, 1436 (2001).

[102] L. Lepetit, G. Chériaux, and M. Joffre, *Linear techniques of phase measurement by femtosecond spectral interferometry for applications in spectroscopy*, Journal of the Optical Society of America B: Optical Physics **12**, 2467 (1995).

[103] I. Thomann et al., *Investigation of a grating-based stretcher/compressor for carrier-envelope phase stabilized fs pulses*, Optics Express **12**, 3493 (2004).

[104] M. Takeda, H. Ina, and S. Kobayashi, *Fourier-transform method of fringe-pattern analysis for computer-based topography and interferometry*, Journal of the Optical Society of America **72**, 156 (1982).

[105] W. H. Press, S. A. Teukolsky, W. T. Vetterling, and B. P. Flannery, *Numerical recipes in C: the art of scientific computing* (Cambridge University Press, 1992).

[106] M. Uiberacker et al., *Attosecond real-time observation of electron tunnelling in atoms*, Nature **446**, 627 (2007).

[107] N. F. Ramsey, *A molecular beam resonance method with seperated oscillating fields*, Physical Review **78**, 695 (1950).

[108] S. Cavalieri, R. Eramo, M. Materazzi, C. Corsi, and M. Bellini, *Ramsey-type spectroscopy with high-order harmonics*, Physical Review Letters **89**, 133002 (2002).

[109] R. J. Jones and J. Ye, *High-repetition-rate coherent femtosecond pulse amplification with an external passive optical cavity*, Optics Letters **29**, 2812 (2004).

[110] M. B. Gaarde, F. Salin, E. Constant, Ph. Balcou, K. J. Schafer, K. C. Kulander, and A. L'Huillier, *Spatiotemporal separation of high harmonic radiation into two quantum path components*, Physical Review A: Atomic, Molecular, and Optical Physics **59**, 1367 (1999).

[111] A. Huber, B. Gross, M. Weitz, and T. W. Hänsch, *High-resolution spectroscopy of the* $1S - 2S$ *transition in atomic hydrogen*, Physical Review A: Atomic, Molecular, and Optical Physics **59**, 1844 (1999).

[112] C. G. Parthey et al., *Precision Measurement of the Hydrogen-Deuterium* $1S - 2S$ *Isotope Shift*, Physical Review Letters **104**, 233001 (2010).

[113] A. Gumberidze et al., *Quantum electrodynamics in strong electric fields: The ground-state lamb shift in hydrogenlike uranium*, Physical Review Letters **94**, 223001 (2005).

[114] D. Hagena, R. Ley, D. Weil, G. Werth, W. Arnold, and H. Schneider, *Precise measurement of n=2 positronium fine-structure intervals*, Physical Review Letters **71**, 2887 (1993).

[115] V. Meyer et al., *Measurement of the* $1s - 2s$ *Energy Interval in Muonium*, Physical Review Letters **84**, 1136 (2000).

[116] V. I. Korobov, L. Hilico, and J.-P. Karr, *Relativistic corrections of* $m\alpha^6(m/M)$ *order to the hyperfine structure of the* H_2^+ *molecular ion*, Physical Review A: Atomic, Molecular, and Optical Physics **79**, 012501 (2009).

[117] J. C. J. Koelemeij, B. Roth, A. Wicht, I. Ernsting, and S. Schiller, *Vibrational spectroscopy of HD+ with 2-ppb accuracy*, Physical Review Letters **98**, 173002 (2007).

[118] E. J. Salumbides, G. D. Dickenson, T. I. Ivanov, and W. Ubachs, *QED Effects in Molecules: Test on Rotational Quantum States of* $H2$, Physical Review Letters **107**, 043005 (2011).

[119] D. Hanneke, S. Fogwell, and G. Gabrielse, *New Measurement of the Electron Magnetic Moment and the Fine Structure Constant*, Physical Review Letters **100**, 120801 (2008).

[120] K. Pachucki and U. D. Jentschura, *Two-loop Bethe-logarithm correction in hydrogenlike atoms*, Physical Review Letters **91**, 113005 (2003).

[121] R. Pohl et al., *The size of the proton*, Nature **466**, 213 (2010).

[122] U. D. Jentschura, *Proton radius, Darwin-Foldy term and radiative corrections*, European Physical Journal D **61**, 7 (2011).

[123] A. De Rujula, *QED confronts the radius of the proton*, Physics Letters B **697**, 26 (2011).

[124] I. C. Cloet and G. A. Miller, *Third Zemach moment of the proton*, Physical Review C **83**, 012201 (2011).

[125] V. Barger, C. W. Chiang, W. Y. Keung, and D. Marfatia, *Proton Size Anomaly*, Physical Review Letters **106**, 153001 (2011).

[126] S. W. Epp et al., *X-ray laser spectroscopy of highly charged ions at FLASH*, Journal of Physics B-atomic Molecular and Optical Physics **43**, 194008 (2010).

[127] K. Eikema, W. Ubachs, W. Vassen, and W. Hogervorst, *1st Laser Excitation Of The* ^{4}He1^1S-2^1P *Resonance Line At* 58nm, Physical Review Letters **71**, 1690 (1993).

[128] K. S. E. Eikema, W. Ubachs, W. Vassen, and W. Hogervorst, *Precision Measurements in Helium at 58 nm: Ground State Lamb Shift and the* 1^1S-2^1P *Transition Isotope Shift*, Physical Review Letters **76**, 1216 (1996).

[129] S. D. Bergeson, K. G. H. Baldwin, T. B. Lucatorto, T. J. McIlrath, C. H. Cheng, and E. E. Eyler, *Doppler-free two-photon spectroscopy in the vacuum ultraviolet: helium 1 1S–2 1S transition*, Journal of the Optical Society of America B: Optical Physics **17**, 1599 (2000).

[130] M. M. Salour and C. Cohen-Tannoudji, *Observation of Ramsey's Interference Fringes in the Profile of Doppler-Free Two-Photon Resonances*, Physical Review Letters **38**, 757 (1977).

[131] R. Teets, J. Eckstein, and T. W. Hänsch, *Coherent Two-Photon Excitation by Multiple Light Pulses*, Physical Review Letters **38**, 760 (1977).

[132] P. Salieres et al., *Frequency-domain interferometry in the XUV with high-order harmonics*, Physical Review Letters **83**, 5483 (1999).

[133] M. Bellini, S. Cavalieri, C. Corsi, and M. Materazzi, *Phase-locked, time-delayed harmonic pulses for high spectral resolution in the extreme ultraviolet*, Optics Letters **26**, 1010 (2001).

[134] M. Kovacev et al., *Extreme ultraviolet fourier-transform spectroscopy with high order harmonics*, Physical Review Letters **95**, 223903 (2005).

[135] I. Liontos et al., *Ramsey spectroscopy of bound atomic states with extreme-ultraviolet laser harmonics*, Optics Letters **35**, 832 (2010).

[136] J. Seres et al., *Source of coherent kiloelectronvolt X-rays*, Nature **433**, 596 (2005).

[137] P. Fendel, S. D. Bergeson, Th. Udem, and T. W. Hänsch, *Two-photon frequency comb spectroscopy of the 6s-8s transition in cesium*, Optics Letters **32**, 701 (2007).

[138] A. Marian, M. C. Stowe, D. Felinto, and J. Ye, *Direct frequency comb measurements of absolute optical frequencies and population transfer dynamics*, Physical Review Letters **95**, 023001 (2005).

[139] A. L. Wolf, S. A. van den Berg, W. Ubachs, and K. S. E. Eikema, *Direct Frequency Comb Spectroscopy of Trapped Ions*, Physical Review Letters **102**, 223901 (2009).

[140] R. Zerne et al., *Phase-locked high-order harmonic sources*, Physical Review Letters **79**, 1006 (1997).

[141] A. Ozawa et al., *High harmonic frequency combs for high resolution spectroscopy*, Physical Review Letters **100**, 253901 (2008).

[142] D. Z. Kandula et al., *Ultrafast double-pulse parametric amplification for precision Ramsey metrology*, Optics Express **16**, 7071 (2008).

[143] D. C. Morton, Q. Wu, and G. W. F. Drake, *Energy levels for the stable isotopes of atomic helium ^{4}He I and ^{3}He I*, Canadian Journal of Physics **84**, 83 (2006).

[144] C. Corsi, A. Pirri, E. Sali, A. Tortora, and M. Bellini, *Direct interferometric measurement of the atomic dipole phase in high-order harmonic generation*, Physical Review Letters **97**, 023901 (2006).

[145] G. Herzberg, *Ionization Potentials and Lamb Shifts of the Ground States of ^{4}He and ^{3}He*, Proceedings of the Royal Society (London) A **248**, 309 (1958).

[146] P. K. Kabir and E. E. Salpeter, *Radiative Corrections to the Ground-State Energy of the Helium Atom*, Physical Review **108**, 1256 (1957).

[147] J. J. Hopfield, *New Ultra-Violet Spectrum of Helium*, The Astrophysical Journal **72**, 133 (1930).

[148] G. W. Kellner, *Die Ionisierungsspannung des Heliums nach der Schrödingerschen Theorie*, Zeitschrift für Physik **44**, 91 (1927).

[149] J. C. Slater, *The Structure of the Helium Atom*, Proceedings of the National Academy of Sciences **13**, 423 (1927).

[150] M. A. Baig, J. P. Connerade, C. Mayhew, G. Noeldeke, and M. J. Seaton, *On the principal series helium*, Journal of Physics B: Atomic and Molecular Physics **17**, L383 (1984).

[151] T. Lyman, *The Spectrum of Helium In the Extreme Ultra-Violet*, The Astrophysical Journal **60**, 1 (1924).

[152] J. Sucher, *Energy Levels of the Two-Electron Atom to Order α^3 ry; Ionization Energy of Helium*, Physical Review **109**, 1010 (1958).

[153] M. Herrmann et al., *Feasibility of coherent xuv spectroscopy on the 1S-2S transition in singly ionized helium*, Physical Review A: Atomic, Molecular, and Optical Physics **79**, 052505 (2009).

[154] T. J. Pinkert, D. Z. Kandula, C. Gohle, I. Barmes, J. Morgenweg, and K. S. E. Eikema, *Widely tunable extreme UV frequency comb generation*, Optics Letters **36**, 2026 (2011).

[155] R. van Rooij, J. S. Borbely, J. Simonet, M. D. Hoogerland, K. S. E. Eikema, R. A. Rozendaal, and W. Vassen, *Frequency metrology in quantum degenerate helium: direct measurement of the* $2\,^3\mathrm{S}_1 - 2\,^1\mathrm{S}_0$ *transition*, Science **333**, 196 (2011).

[156] H. Rubens and H. Hollnagel, *Measurements in the extreme infrared spectrum*, Philosophical Magazine **19**, 761 (1910).

[157] N. de Oliveira, M. Roudjane, D. Joyeux, D. Phalippou, J.-C. Rodier, and L. Nahon, *High-resolution broad-bandwidth Fourier-transform absorption spectroscopy in the VUV range down to 40 nm*, Nature Photonics **5**, 149 (2011).

[158] M. E. Michelson Albert Abraham, *On the Relative Motion of the Earth and the Luminiferous Ether*, American Journal of Science **34**, 333 (1887).

*

List of Publications

This thesis is based on the following publications:

Chapter 4:

Phase stability of terawatt-class ultrabroadband parametric amplification
A. Renault, D. Z. Kandula, S. Witte, A. L. Wolf, R.Th. Zinkstok, W. Hogervorst K. S. E. Eikema
Optics Letters **32**, 2363-2365, (2007)

Chapter 5:

Ultrafast double-pulse parametric amplification for precision Ramsey metrology
D. Z. Kandula, A. Renault, Ch. Gohle, A. L. Wolf, S. Witte, W. Hogervorst, W. Ubachs, K. S. E. Eikema
Optics Express **16**, 7071-7082, (2008)

Chapter 6:

Frequency comb metrology in the XUV on the ground state of helium
D. Z. Kandula, Ch. Gohle, T. J. Pinkert, W. Ubachs, K. S. E. Eikema
Submitted to Physical Review A

and

Extreme ultraviolet frequency comb metrology
D. Z. Kandula, Ch. Gohle, T. J. Pinkert, W. Ubachs, K. S. E. Eikema
Physical Review Letters **105**, 063001, (2010)

The author contributed also to the following publication

Widely tunable XUV frequency comb generation
T. J. Pinkert, D. Z. Kandula, Ch. Gohle, I. Barmes, J. Morgenweg, K. S. E. Eikema
Optics Letters **36**, 2026-2028, (2011)

Summary

High precision measurements are intimately linked to major advances in the modern Science. A very famous example of the impact of a precision measurement on our notion of the laws of physics is the Michelson-Morley experiment [158]. It was carried out at the beginning of the 20^{th} century to measure the movement of the aether wind by interferometric means. However, the experiment failed, and instead provided the first strong evidence that the velocity of light is constant, and irrespective of the speed of the observer. The knowledge obtained in this measurement resulted in the theory of special and general relativity.

Half a century later another high-precision experiment, carried out by Lamb and Retherford [35], provided detailed information about the electronic structure of the hydrogen atom. Surprisingly they found that it was in disagreement with predictions of the quantum theory at that time. This kind of discrepancies are now called 'Lamb shifts', and it has subsequently been explained with quantum electrodynamics theory (QED). The extension of the body of the quantum theory with QED did perhaps not revolutionize the scientific paradigm to the same extent as special (or general) relativity did, but it provided major new insights and tools for the description of the interaction between light and matter, and therefore also e.g. of atomic structure.

A central notion in QED is that the vacuum (or space in general) is never really empty, but in fact full of so-called virtual particles. These particles can be thought to appear, and quickly disappear again, within the constraints of Heisenbergs uncertainty principle for energy and time. The shorter the time scale, the bigger the energy uncertainty is, leading to e.g. spontaneous electron-positron pair creation (and annihilation). Heisenbergs uncertainty principle implies that virtual particles can exist only for extremely short time intervals, shorter than e.g. electron dy-

namics in an atom. However, there is a net effect, e.g. on the energy states of atoms and molecules, which is what QED calculates. The idea that empty space is in fact full of constantly appearing and disappearing particles was a big surprise, and still appears strange to many. However, despite its strangeness, QED has been extremely successful and is currently the best tested physics theory.

QED can be tested in several ways, e.g. by performing precision laser spectroscopy on atoms and molecules. Ideally, the spectroscopy is performed in the form of a frequency measurement as it enables the highest accuracy in precision tests. The ultimate limit on accuracy in this case is determined by the frequency reference, typically an atomic clock. The most common one, available in national metrology institutes all over the world, is based on a microwave hyperfine transition in Cesium and can reach a typical fractional accuracy in the range of 10^{-13} - 10^{-16}. The latest atomic clocks based on an optical transition have even reached a precision on the order of 10^{-17} in a relative frequency measurement [11]. However, absolute measurements with this level of accuracy are presently impossible because the standard of time and frequency is still based on Cesium clocks.

To perform *optical* frequency measurements for laser spectroscopy is not trivial. Until about a decade ago, complex "frequency chains" were needed in order to transfer the accuracy of microwave atomic clocks to the optical region at frequencies of several hundred THz. This typically required a big lab, including a lot of lasers and electronics, and several people to run it. The invention of the optical frequency comb [10, 60] has changed all that, and optical frequency determinations have now almost become routine. Frequency combs are generally based on modelocked lasers which are often smaller than 1 m^2 in size, and can be operated by a single person. External feedback is used for precise control over the repetition rate and phase evolution of the optical pulses from such a laser. As a result the spectrum of the pulses is equal to typically hundreds of thousands of equidistant modes. The positions of the modes can be described by just two radio frequencies that can easily be measured electronically. The frequency comb laser can therefore act as a gear wheel transmission between the radio frequencies where most atomic clocks operate, and optical frequencies that are used for laser precision spectroscopy. This principle has caused a revolution in many

scientific fields. Frequency combs are now a vital part of the best optical atomic clocks, and play an important role in the field of attosescond physics, which studies phenomena that take place on a time scale of 10^{-18} seconds. However, up to now there have been no frequency comb devices that would allow measurements in the extreme ultraviolet.

In this thesis a method is demonstrated to test QED on the ground state of helium, by performing the first absolute frequency measurement in the extreme ultraviolet at 6 PHz (51 nm) with a frequency comb in the XUV. This XUV comb (XFC) is based on harmonic upconversion of a near-infrared frequency comb. The ground state ionization energy of helium obtained with the XFC has an unprecedented accuracy of 10^{-9}. From this measurement a Lamb shift of the helium ground state is derived equal to 41247(6) MHz, which agrees with the most recent theoretical predictions of 41284(36) MHz [30], 41285(36) MHz [32, 31] and 41264(42) MHz [23], though challenging their precision. The measured value is precise enough to resolve the discrepancy between the previous measurements of the helium ground state energy. Correcting Eikemas [40] result for the missing recoil shift yields a Lamb shift of 41250(45), which is confirmed by the result presented here. Bergesons [41] value, however, is almost 3σ away.

The first two chapters of this thesis introduce the theoretical background of the energy structure of helium and of the employed experimental techniques. Chapter 3 then gives a systematic overview of the components of the XUV-frequency comb (XFC) source. An important ingredient is parametric amplification of frequency comb pulses. In chapter 4 an investigation is presented about the phase stability of broadband single-pulse parametric amplification. To convert a frequency comb to the XUV actually a minimum of two pulses from a comb laser need to be amplified. Such a system is presented in chapter 5, including a phase characterization of the amplified pulses. The final step to convert the frequency comb to the XUV takes place with high-harmonic generation using the amplified pulses. The generated light has been used to coherently excite helium from the ground state to one of the higher lying P states. In effect the excitation takes place with a frequency comb created at the 15^{th} harmonic of the original infrared pulse pair. The excited helium atoms were ionized by a 1064 nm laser pulse and detected in a time of flight mass spectrometer. Scanning of the XFC over the

transition is realized by changing the repetition rate of the fundamental oscillator. This gives rise to Ramsey fringes in the observed excited state population. Recording of the signal at (several) repetition rates between $100 - 185$ MHz allowed to determine the frequency of the observed transitions, and derive the ionization energy of the ground state. A detailed account of this experiment is given in chapter 6. Finally, in chapter 7, an outlook is given for future experiments with the developed extreme ultraviolet frequency comb.

Samenvatting

De Nederlandse titel van dit proefschrift luidt: "XUV frequentiekammetrologie en de grondtoestand van helium". Bij vele grote vooruitgangen in de moderne wetenschap hebben precisiemetingen een belangrijke rol gespeeld. Een van de beroemdste voorbeelden hiervan is het experiment van Michelson en Morley [158] aan het begin van de 20^e eeuw. De aanleiding van het experiment was een bepaling van de invloed van de 'aether wind' op de snelheid van het licht via interferometrie, maar in plaats daarvan werd een sterke aanwijzing gevonden dat de lichtsnelheid in vacuum altijd constant is, ongeacht de beweging van de waarnemer. Deze uitkomst leidde tot de ontwikkeling van de speciale relativiteitstheorie, en iets later tot de algemene relativiteitstheorie.

Een halve eeuw later gaf een ander precisie-experiment, dat werd uitgevoerd door Lamb and Retherford [35], gedetailleerde informatie over the energiestructuur van het waterstofatoom. Het was een verrassing dat die niet in overeenstemming bleek te zijn met de voorspellingen van de quantumtheorie van die dagen. Het verschil wordt nu de 'Lamb-verschuiving' genoemd, en kon verklaard worden na de ontwikkeling van quantum-electrodynamica (QED). De uitbreiding van standaard-quantummechanica met QED zorgde weliswaar niet voor een zelfde paradigmaverschuiving als speciale relativiteitstheorie, maar het was wel een grote stap voorwaarts voor ons begrip van de wisselwerking van licht en materie, en daarmee ook bijvoorbeeld voor het begrijpen van de structuur van atomen.

Een belangrijk ingrediënt van QED is dat een vacuüm (zelfs ruimte in zijn algemeenheid) nooit echt leeg is, maar vol zit met 'virtuele deeltjes'. Deze virtuele deeltjes verschijnen vanuit het niets, en verdwijnen ook weer in het niets op zo'n korte tijdschaal dat energiebehoud niet geschonden wordt binnen de grenzen van de onzekerheidsrelatie voor

tijd en energie van Heisenberg. De tijdschaal waarop de virtuele deeltjes verschijnen en verdwijnen is sneller dan de dynamica van bijvoorbeeld electronen in een atoom. Niettemin is er een netto effect op de energietoestanden van atomen en moleculen, en dat kan met QED worden uitgerekend. Het idee dat een lege ruimte feitelijk niet bestaat, maar altijd gevuld is met deeltjes die voortdurend verschijnen en verdwijnen zorgt nog steeds voor verwondering bij velen. Ondanks de vreemde implicaties van de theorie is QED toch buitengewoon succesvol gebleken in zijn voorspellingen, zodat het op dit moment de best geteste theorie in de fysica is.

QED kan op verschillende manieren getest worden, bijvoorbeeld door precisie-spectroscopie aan atomen en molekulen. In het ideale geval wordt de spectroscopie uitgevoerd in de vorm van een frequentiemeting, omdat daarmee de hoogste nauwkeurigheid mogelijk is. De uiteindelijke grens aan de nauwkeurigheid wordt in dit geval bepaald door de frequentiereferentie die gebruikt wordt, wat doorgaans een atoomklok is. De meest gebruikelijke atoomklok is gebaseerd op cesium, warmee een fractionele nauwkeurigheid gehaald kan worden die gewoonlijk tussen 10^{-13} en 10^{-16} in zit. De meest moderne atoomklokken zijn gebaseerd op een optische overgang, en daarmee is een precisie van ongeveer 10^{-17} gedemonstreerd in een relative frequentiemeting [11]. Het is echter nog niet mogelijk om absolute metingen met deze nauwkeurigheden te doen omdat de standaard voor tijd en frequentie nog steeds gebaseerd is op cesium atoomklokken.

Om een frequentiemeting te doen bij *optische* frequenties voor laserspectroscopie is niet eenvoudig. Tot ruim tien jaar geleden waren complexe "frequentieketens" nodig om de nauwkeurigheid van atoomklokken die bij microgolffrequenties werken (zoals de cesium atoomklok bij 9.2 GHz) naar optische frequenties over te brengen bij honderden THz. Dit nam een heel lab in beslag, bestond uit veel lasers en elektronica, en had ook veel personeel nodig om te functioneren. Door de uitvinding van de frequentiekamlaser [10, 60] is dat is dat enorm vereenvoudigd, en kunnen optische frequentiemetingen vrijwel routinematig plaatsvinden. Een frequentiekam is gebaseerd op een 'modengekoppelde' laser die doorgaans kleiner is dan 1m^2, en die makkelijk door een persoon bediend kan worden. Door externe terugkoppeling wordt de herhalingsfrequentie en fase-evolutie van de pulsen uit zo'n laser heel precies gecontroleerd. Het

spectrum van de pulsen is daarom equivalent met een spectrum in de vorm van (honderdduizenden) equidistante optische modes. De posities van die modes worden gekarakteriseerd met maar twee radiofrequenties die eenvoudig elektronisch te meten zijn. De kamlaser werkt als een soort overbrenging tussen elektronische frequenties waar de meeste atoomklokken functioneren, en de optische frequenties van de lasers voor spectroscopie. Dit principe heeft een ware revolutie teweeggebracht in vele wetenschappelijke disciplines. Zo zijn frequentiekammen tegenwoordig een centraal onderdeel in de eerder genoemde optische atoomklokken. Maar bijvoorbeeld ook voor attosecondenfysica, waarbij verschijnselen worden bestudeerd die zich afspelen op een tijdschaal van 10^{-18} seconde, spelen frequentiekammen een belangrijke rol. Tot nu toe waren er echter geen frequentiekammen die metingen in het extreem ultraviolet mogelijk maakten.

In dit proefschrift wordt een methode gedemonstreerd om QED te testen in helium door de eerste absolute frequentiebepaling te doen in het extreem ultraviolet by 6 PHz (51 nm) met een frequentiekam in het extreem-ultraviolet. Deze XUV kam (XFC) is gebasserd op harmonische opconversie van een nabije-infrarood frequentiekam. De energiepositie van de grondtoestand van helium is door middel van de XFC met een ongekende fractionele nauwkeurigheid van 10^{-9} bepaald. Uit deze meting is een Lamb-verschuiving afgeleid voor de grondtoestand van 41247(6) MHz, wat overeenkomt met de meest recente theoretische berekeningen van 41284(36) MHz [30], 41285(36) MHz [32, 31] en 41264(42) MHz [23]. De experimentele waarde is echter wel duidelijk nauwkeuriger dan de theorie. Dit maakt ook een interessante vergelijking mogelijk met eerdere metingen van de grondtoestandsenergie van helium die onderling niet met elkaar overeen komen. Als de meting van Eikema et al. [40] wordt gecorrigeerd voor een "recoil shift" die indertijd niet is meegenomen, dan resulteert een Lamb-shift van 41250(45), wat goed overeenkomt met de waarde die nu met de XFC bepaald is. De waarde bepaald door Bergeson et al. [41] wijkt echter bijna 3σ af.

In de eerste twee hoofdstukken van dit proefschrift wordt een overzicht gegeven van de theorie die de energiestructuur van helium beschrijft, en worden de gebruikte experimentele technieken geïntroduceerd. Hoofdstuk 3 geeft vervolgens een systematisch overzicht van de verschillende componenten waaruit de XUV frequentiekam is opge-

bouwd. Een belangrijke component is parametrische versterking van frequentiekam-pulsen. In hoofdstuk 4 wordt een experiment beschreven waarin de fase-stabiliteit is onderzocht voor parametrische versterking van individuele kamlaserpulsen. Om een frequentiekam te maken zijn minimaal twee versterkte pulsen nodig. Een systeem wat daartoe in staat is wordt beschreven in hoofdstuk 5, inclusief het resultaat van de fase-karakterisatie. Als laatste stap voor de realisatie van een frequentiekam in het XUV is hoge-harmonische generatie toegepast met de versterkte laserpulsen. Het licht wat hierbij ontstaat kan gebruikt worden om direct helium te exciteren vanuit de grondtoestand naar een hoger gelegen P toestand. In feite wordt helium zo geëxciteerd met een soort frequentiekam die gegenereerd is op de 15^e harmonisch van de oorspronkelijke infrarode laserpulsen. Voor detectie zijn de helium atomen met behulp van een 1064 nm laser geïoniseerd, en vervolgens gedetecteerd met een vluchttijd-massaspectrometer. De frequentie van de XFC modes kunnen worden verschoven door de repetitiefrequentie van de oorspronkelijke frequentiekamlaser aan te passen. Als gevolg hiervan wordt de excitatiewaarschijnlijkheid gemoduleerd in de vorm van zgn. Ramsey oscillaties. Door deze oscillaties te meten voor verschillende repetitiefrequenties van de kamlaser over een bereik van $100 - 185$ MHz is het mogelijk geworden de absolute frequentie van de gemeten overgangen te bepalen, en daaruit de grondtoestandsenergie (ionisatie-energie) te bepalen. Een gedetailleerde beschrijving van dit experiment wordt gegeven in hoofdstuck 6. Tenslotte wordt in hoofdstuk 7 een vooruitblik gegeven voor toekomstige experimenten met de ontwikkelde extreem-ultraviolet frequentiekam.

Acknowledgements

This thesis reports on a very complex experiment, which I would never have been able to do carry out without the support of many people.

In the first place I want to thank my doctoral advisors Wim Ubachs and Kjeld Eikema for giving me the opportunity to build the XUV-frequency comb and carry out a spectroscopic experiment with it.

Kjeld, I would have to write here that it was the biggest luck of my life to have you as my thesis supervisor, if I have not met Nele before. Your expertise is truly impressive and I have the feeling to have learned more from you in the 43 month that I spent in Amsterdam than during my whole preceding education. Besides your professional qualities, there is also an other side of your personality that made my PhD time in the VU even more enjoyable. Your dark humor and the predilection for nonsense that we share helped me particularly in the beginning, when the sad feeling to live separated from my family was counterbalanced by the pleasant anticipation of working in your team.

Wim, from the beginning of my PhD we agreed, that Kjeld would become my immediate supervisor, while you would follow my progress from the background. This has never meant that you did not care, but that you would conduce to our success at these particular moments, when we needed your help most. I was always very impressed to see how much better our articles (and the thesis) became, after your review of our manuscripts. As the leader of the group, a major part of the credit for the great atmosphere in our group belongs to you. In your group high professional standard combines with a cheerful informal atmosphere. I will also never forget the magnificent view on Holland from the frozen Amstel river: an experience that I made - thanks to you.

During the most difficult part of my PhD research I have got a lot of support from my predecessors: Stefan Witte and Roel Zinkstok. It was

not easy for me to follow in their footsteps, but they made it somehow possible in a kind and patient way. I was lucky with Stefan, who stayed in the VU and supported me with the problems in lab during my entire stay in Amsterdam. Roel and Stefan, I want to apologize for the downgrading of your tremendous NOPCPA to this pathetic state.

Amandine Renault joined the group shortly after me to develop and prove phase-stable amplification of pulse pairs. Later Christoph Gohle joined to bring the helium spectroscopy to work. I would have never managed to develop the machine without their help. Amandine, has got the difficult task to introduce a newbie (me) to one of the most advanced laser systems in the world. Christoph, you took care that the spectroscopy became doable and after a long cumbersome preparation we went together through the 24+ hours shifts in the lab to get enough data for the helium ground state. You also ensured that I can do the experiment and its analysis on my own, which was necessary, as the analysis matched the complexity of the experiment itself and you have not had enough time in Amsterdam to finish it together with me.

Many more have helped with the experiments presented in this thesis and to write the thesis itself either with their work or with discussions of our problems end their possible solutions or just by contributing to the nice atmosphere in Wims group. I want to thank Dimitris Charalambidis, Paris Tzallas and Manolis Benis for the hospitality and the fruitful discussions during my stay in FORTH IESL. Jacques Bouma has helped with the best system for optical and for vacuum components in the world. Anne Lisa Wolf has build the black comb, Tjeerd Pinkert the wheel of fortune. Toncho Ivanov, helped us with the mass spectrometer. Fernando Brandi has shown me how to operate the HHG-chamber. Wim Vassen has helped me with the helium QED. Oleg Kornilov helped to cope with the theory chapter. Finally I have to thank Itan, Edcel, Kees, Wim Hogervorst, Ofelia, Rob, Roel, Sandro, Tom, Dmitry, Rick, Jeroen, John, Lineke, Elmar, Cesar, Valdas, Daniel, Jonas, Ali, Gareth, Dongfeng, Adrian, Paul, Jop, Ziyu, Maria, Eric-Jan and more.

Special thanks to Charaf Cherkouk for the painting “Das Messbare und das Beobachtbare” that became the cover of my thesis, to Swami Perikamana for lessons that enabled me to carry out the research and to The Timelords for The Manual. Nele, danke für alles.